Size effects in small-scale structures of body-centered cubic metals

Dissertation

zur Erlangung des Grades

des Doktors der Ingenieurwissenschaften

der Naturwissenschaftlich-Technischen Fakultät III

Chemie, Pharmazie, Bio- und Werkstoffwissenschaften

der Universität des Saarlandes

von

Oscar Torrents Abad

Angefertigt am INM – Leibniz-Institut für Neue Materialien

Programmbereich Funktionelle Mikrostrukturen

Universität des Saarlandes

Saarbrücken

2016

Tag des Kolloquiums:	16. November 2016
Dekan:	Prof. Dr.-Ing. Dirk Bähre
Berichterstatter:	Prof. Dr. Eduard Arzt Prof. Dr. Christian Motz
Vorsitz:	Prof. Dr.-Ing. Dirk Bähre
Akad. Mitarbeiterin:	Dr.-Ing. Dr. Anne Jung

A la meva mare

Abstract

Small-scale metal structures play a crucial role in a broad range of technological applications. However, knowledge of mechanical properties at this size scale is lacking. Size strengthening effects are generally experienced at the microscale. Compression of non-free defect body centered cubic (BCC) metal micropillars has revealed that the size effect of these metals scales with a temperature ratio that signifies how much the yield strength is governed by screw dislocation mobility. So far, no effort has been made to systematically study the effect of screw dislocation mobility and lattice resistance on the size effect in BCC-based metals. Thus, this work investigated this in BCC tungsten (W) and tantalum (Ta), as well as B2 beta-brass (β-CuZn) and nickel aluminide (NiAl). The influence of temperature on the size effect in W and Ta was studied up to 400 °C, whereas the room-temperature size effect in β-CuZn and NiAl was studied as a function crystal orientation and deformation rate. It was found that the size effect scaled with the magnitude of the lattice resistance, which is strongly related to the screw dislocation mobility. Direct evidence of the mobility of screw dislocations was observed for the first time. The results also showed that plastic anisotropy vanishes with decreasing sample size and that ductility is considerably improved, thus highlighting the importance of dislocation-nucleation controlled deformation and screw dislocation mobility at the sub-micron scale.

Zusammenfassung

Metallische Strukturen auf Mikroskala spielen bei einer Vielzahl von technologischen Anwendungen eine wichtige Rolle – jedoch sind die Kenntnisse über mechanische Eigenschaften in dieser Größenordnung begrenzt. Größeneffekte kommen i. d. R. auf Mikroskala zum Tragen. Druckversuche mit krz-Mikropillars konnten zeigen, dass der Größeneffekt auf Mikroskala hauptsächlich vom Temperaturverhältnis abhängt, die Fließspannung also durch die Mobilität der Schraubenversetzungen bestimmt wird. Bisher liegen keine systematischen Untersuchungen des Einflusses der Mobilität von Schraubenversetzungen und des Gitterwiderstandes auf den Größeneffekt von krz-Metallen vor. In der vorliegenden Arbeit wurde diese Fragestellung anhand von W und Ta sowie β-CuZn und NiAl aus der Phase B2 untersucht. Hierbei wurden der Temperatureinfluss auf den Größeneffekt von W und Ta bis 400°C und der Größeneffekt von β-CuZn und NiAl bei Raumtemperatur als Funktion der Kristallorientierung und Deformationsrate betrachtet. Es konnte gezeigt werden, dass der Größeneffekt mit dem Gitterwiderstand skaliert, somit also eng mit der Mobilität der Schraubenversetzungen in Zusammenhang steht. Die Ergebnisse von NiAl haben offengelegt, dass die plastische Anisotropie mit kleiner werdenden Proben bis in den Submikrometerbereich verschwindet und sich die Duktilität beträchtlich verbessert. Die Untersuchungen zeigen die Bedeutung von Deformation und Mobilität der Schraubenversetzungen bedingt durch Versetzungsnukleation.

Acknowledgments

Over the last four years, I have had the pleasure to interact with many people who, in one way or another, have helped me complete this thesis. First of all, I would like to thank my scientific advisor, Prof. Eduard Arzt, for his advice and support. He has listened to and guided me when needed and, at the same time, given me the freedom to work and explore as I wished, something I think is very enriching for a PhD student. Everything written in this thesis is the result of discussions with him. I am thankful to him in many ways.

This thesis could not have been possible without Dr. Andreas S. Schneider. My sincere thanks go to him. He opened me the doors to the INM-Leibniz Institute for New Materials and welcomed me to his research group, the Metallic microstructures group, first as a research intern and afterwards as a PhD student. He quickly transmitted his passion to science, and constantly encouraged me with new ideas and ways to approach problems. Thank you.

I greatly thank Dr. Jeffrey M. Wheeler and Dr. Johann Michler for our successful collaboration on the elevated temperature tests. Without their help, chapter 4 could have not been done. I also wish to thank Dr. Carl P. Frick, Assistant Professor of Mechanical Engineering at the University of Wyoming, USA, for his interest in this thesis as well as critical review and discussion of chapters 5 and 6. Furthermore, Bentejuí Medina Clavijo, former master student at the INM, has been of great help in the labs, where he helped me prepare the specimens and testing setups when needed, and had the time to comment on chapters 5 and 6.

I have found many answers to daily research issues at the chair of Materials Science and Methods at the University of Saarland. Prof. Christian Motz, scientific co-advisor of this work, Dr. Mohammad Zamanzade and Jorge Rafael Velayarce have shown continuous interest in my work, and provided me with interesting discussions on nanomechanics / microplasticity.

I wish to thank Dr. Arnaud Caron, for his interest in the topic and useful discussions on plasticity matters. Thanks to Dr. Markus Koch and Birgit Heiland for transmission electron microscopy training, and Rudolf Karos for carrying out X-ray diffraction measurements. In addition, I would like to specially thank Birgit Heiland for showing me all intricacies of sample preparation and scanning electron microscopy as well as helping me with focused ion beam (FIB) machining issues.

Dr. Elmar Kroner, Dr. Nathalie K. Guimard and Dr. René Hensel, deputy heads of the Functional Microstructures group over the years I have been at the INM, are sincerely acknowledged for unquestionably supporting this work and offering their help when possible.

I would like to thank all my colleagues at the INM, particularly those of the Functional Microstructures group and former Metallic Microstructures group. From senior to young researchers, technicians and administrative personnel, thank you all for your help throughout these years.

Finally, I would like to thank my family and friends for their unconditional support. Regardless of the distance, they are always there to encourage me. Particularly, I would like to thank my mother, Maria Carmen Abad Palos, and my wife, Jinkyung Pyo, for being always next to me and supporting me as much as they do. Thank you so much.

Contents

List of Abbreviations and Symbols

Abbreviations

APB	anti-phase boundary
BCC	body-centered cubic
CRSS	critical resolved shear stress
CVD	chemical vapor deposition
EBID	electron beam induced deposition
EBSD	electron backscatter diffraction
EDX	energy dispersive x-ray spectroscopy
FCC	face-centered cubic
FIB	focused ion beam
IBID	ion beam induced deposition
KAM	kernel average misorientation
MRSS	maximum resolved shear stress
SEM	scanning electron microscopy
SHR	apparent strain hardening rate
TEM	transmission electron microscopy

Symbols

a	lattice constant [m]
A	Zener's parameter [-]
A_0	cross-sectional area [m^2]
Al	aluminum
Ar	argon
Au	gold
b	Burgers vector [m]
C_{ij}	elastic stiffness constant [Pa]
CH_3OH	methanol
CoTi	cobalt titanium
Cu	copper
C_2H_6O	ethanol
$C_6H_{14}O_2$	2-butoxyethanol
d	top diameter [m]
d_b	bottom diameter [m]
E	Young's modulus [Pa]
F	applied force [N]
Fe	iron
FeAl	iron aluminide
Ga	gallium
h	pillar height [m]
$HClO_4$	perchloric acid
H_2O	distilled water
H_2SO_4	sulfuric acid

H_3PO_4	phosphoric acid
k	material constant
K	Boltzmann's constant [$J \cdot K^{-1}$]
l	dislocation line [m]
L_{seg}	average length of dislocation segments in a pillar [m]
m	strain rate sensitivity [-]
Mo	molybdenum
n	power-law exponent (size effect) [-]
N	number of equivalent nucleation sites [-]
NaOH	sodium hydroxide
Nb	niobium
Ni	nickel
NiAl	nickel aluminide
p	number of dislocation sources [-]
Pt	platinum
Q*	nucleation barrier [J]
s	number of primary slip systems [-]
S	Schmid factor [-]
Ta	tantalum
T_c	critical temperature [K, °C]
T_m	melting temperature [K, °C]
T_{test}	test temperature [K, °C]
V	vanadium
W	tungsten
wt%	weight percentage [%]
Zn	zinc
α	constant of the order of unity [-]

β	angle between the primary slip plane and the compression axis [°]
β-CuZn	beta-brass
$\gamma \cdot \omega$	anti-phase boundary energy [J]
Δx	displacement of the pillar top [m]
ε	strain [-]
$\dot{\varepsilon}$	strain rate [s^{-1}]
λ	angle between the slip direction and the force applied [°]
λ_{max}	maximum source length [m]
$\bar{\lambda}_{max}$	statistical avg. length of the weakest single-arm disl. source [m]
μ	shear modulus [Pa]
ν	Poisson's ratio [-]
v_0	nucleation rate [s^{-1}]
V	activation volume [m^3]
ρ_{mob}	mobile dislocation density [m^{-2}]
ρ_{tot}	total dislocation density [m^{-2}]
σ	applied normal stress [Pa]
σ_i	strength of the interface [Pa]
σ_s	dislocation source strength [Pa]
σ_x	strength related to strengthening factors others than Peierls [Pa]
σ_y	yield strength [Pa]
σ_0	bulk strength [Pa]
τ_{CRSS}	critical resolved shear stress [Pa]
τ_P	Peierls stress [Pa]
τ_μ	athermal component of the critical resolved shear stress [Pa]
τ_0	lattice resistance of the material in shear [Pa]
τ^*	thermal component of the critical resolved shear stress [Pa]
χ	Taylor angle [°]

List of Figures

List of Tables

1 Introduction

Size effects play an important role in the strength of metals. Since the 70's, small-scale metal structures have been continuously developed in order to satisfy the strong technological driving force in which smaller and smaller devices have become a clear demand. However, with the purpose of designing materials of multiple length scales and producing micro-components to use their unique functions, an increased need to understand the fundamental mechanical properties at small scales has emerged.

Over the last two decades, a big effort has been made to study the mechanical behavior of small-scale metal structures. The mechanical properties in bulk material are usually subject to microstructural constraints. If the dimensions of the sample are similar to or smaller than microstructural length scales, as is the case for thin films, interfaces and free surfaces become important. It has been shown that the mechanical properties of micron-sized structures differ from those of bulk material. A so-called 'size effect' has been observed in metals [1], where the strength usually increases with decreasing sample size. This has been first observed in thin films, and it was rationalized in terms of plasticity constrains at the interface between the thin film and the substrate (Nix [2] and Freund [3] model). In 2005, an unprecedented size effect was observed for single crystalline micron-scale pillars. Uchic *et al.* [4] compressed constrained-free single crystalline pillars. Hence, strengthening effects related to either grain boundaries or an underlying substrate such as in thin films could be disregarded. They found that sample size restricts plastic processes, causing a variation in strength as a function of sample size. This unequivocally showed that both the internal structure and the external geometry of a material play a crucial role in the strength of plastically deforming materials. It was realized early on that the plastic response reacts to confinement in crystalline materials. Since then, many studies on the plasticity of metal (and other material classes) nano- and micropillars have been carried out, and have revealed new insights into the fundamentals of plastic deformation of materials. The attention of materials scientists and mechanical engineers has focused on understanding the fundamental deformation mechanisms of materials at

the microscale, with the eventual purpose of obtaining models capable of describing the mechanical behavior of materials across the scales. Such models can, in turn, speed up the design process of novel materials and micro devices.

Fundamental research carried out to understand size effects and deformation mechanisms of materials at the (sub-) microscale has been mainly focused on single crystal metals with a face-centered cubic (FCC) and a body-centered cubic (BCC) crystal structure. Compression of FCC metal micropillars has revealed a universal power-law relationship between pillar diameter d and strength σ_y of the form $\sigma_y \propto d^{-0.6}$ [5]. However, all studies related to size dependence of BCC micropillars have exhibited diminished size dependence relative to FCC. It was postulated that the BCC size dependent deformation behavior is heavily influenced by the effect of the Peierls potential on the motion of screw dislocations [6]. This was suggested by a correlation of the critical temperature (T_c) relative to ambient testing conditions for several BCC metals [7]. Furthermore, Mo micropillars compressed at 500 K showed a size dependence very close to that of FCC metals [8], suggesting that the mobility of screw dislocations play an important role on small-scale BCC pillar deformation.

1.1 Aim and outline of this work

Currently, the mechanical behavior of BCC metals at small scales is not well understood; the precise role of thermal activation on small-scale deformation of metals is still an open question. Therefore, the overarching goal of this work is to establish a deeper knowledge of the defect behavior thought to be responsible for the size effect on strength of BCC-based metals. To that end, the effect of temperature on the plasticity of BCC metal micropillars was studied systematically. Focused ion beam (FIB) machined pillars of single crystalline tantalum (Ta) and tungsten (W) with diameters ranging from 5 µm down to 500 nm were compressed at different temperatures, from room temperature to 400 °C. Since most BCC metals possess a strong thermal component to the strength at room temperature, other materials with a similar crystal structure but a much lower thermal component were also employed to further study size effects. In this case, beta-brass (β-CuZn), which possesses a BCC-based crystal structure (B2) and a low thermal component to the strength at room temperature, was studied by compressing micron-sized pillars crystallographically oriented to show single and multiple slip. In addition, the strain rate sensitivity of β-CuZn micropillars was explored, so that insights into the

deformation rate limiting mechanisms could be obtained. Size effects of β-CuZn and mainly B2 alloys have barely been explored [9–11]. Little is known about their deformation behavior at the microscale. Thus, the third main purpose of this work was to extend the knowledge of size effects to another class of B2 alloys, which do not deform in the same fashion as β-CuZn. Although the crystal structure of B2 alloys resembles that of BCC metals, the slip behavior might be different from the commonly observed for BCC metals and β-CuZn, the ⟨111⟩ slip direction. Nickel aluminide (NiAl) is a clear example for this: it also possesses a B2 crystal structure, but its dominant slip direction is ⟨100⟩. Hence, the size and crystallographic orientation dependent strengthening effects of NiAl were examined by compressing micropillars at room temperature. Emphasis was placed on the effect of sample size on the plastic anisotropy of NiAl, which strongly depends on the bulk strength of the material.

In summary, through *in situ* scanning electron microscopy (SEM) microcompression tests, and post-mortem electron backscatter diffraction (EBSD) and transmission electron microscopy (TEM) investigations, this work aims to study not only the deformation behavior of FIB milled BCC metals at elevated temperatures, but also the room-temperature deformation behavior of β-CuZn and NiAl pillars.

This dissertation consists of the following: Chapter 2 reviews the mechanical behavior of BCC metals and B2 alloys as well as the state of the art on size effects and small-scale plasticity with focus on BCC metals. Chapter 3 presents the different materials, sample preparation and microcompression techniques used. It also examines the limitations of the test methodology and emphasizes potential issues that might affect the experimental measurements. Chapter 4 examines the temperature dependence of the size effect on strength of [111]-oriented Ta and [100]-oriented W single crystalline pillars. This chapter has been published by O. Torrents Abad, J. M. Wheeler, J. Michler, A.S. Schneider and E. Arzt in Acta Materialia, 103, 483–494 (2016). The fundamental aspects of room-temperature plastic deformation of sub-micron and micron-sized β-CuZn pillars are presented in Chapter 5, highlighting the influence of sample size, crystallographic orientation and strain rate on their strength. Chapter 6 investigates the role of crystallographic orientation and strain rate on the size effect of NiAl pillars. Attention is paid to the changes in deformation morphology, plastic anisotropy and ductility compared to bulk NiAl. In Chapter 7, the dissertation ends with concluding remarks of the work done in this thesis, as well as with a guideline for future work.

2 Literature review

2.1 Plasticity in metals

The mechanical properties of crystalline materials are unequivocally linked to the underlying material microstructure. In crystalline metals, properties such as the mechanical strength depend strongly on the availability of dislocations and interaction of these with obstacles in the microstructure [12–14]. Dislocations produce permanent plastic deformation and are line defects consisting of atoms moved from their initial location. The motion of a dislocation across a crystal produces a deformation of the crystal structure whereby the atoms on one side of the dislocation plane move forward one atomic spacing from their initial locations. The magnitude and direction of an atomic displacement is given by the Burgers vector. Dislocations can have two distinct characters: edge or screw. Edge dislocations have the Burgers vector b and dislocation line l perpendicular to each other while screw dislocations have b and l parallel to one another. However, dislocations are often of mixed character, i.e., they possess an edge and a screw component, and therefore, the resultant angle between b and l differs from pure edge and screw dislocations. Dislocations generally move in the crystallographic planes and directions that are most tightly packed, called slip planes and slip directions. This occurs because the atoms are more strongly bonded to the neighboring in-plane atoms than to the out-of-plane atoms so that it is easier to move relative to the out-of plane atoms. On the other hand, atoms move along the most densely packed direction since it is the shortest movement needed to recover the original crystal order. A slip plane and a slip direction within this plane form a slip system. For instance, the slip systems generally observed for FCC metals are the $\langle 110 \rangle \{111\}$ while for BCC metals the $\langle 111 \rangle \{110\}$ and $\langle 111 \rangle \{112\}$ [12]. As a result of the movement of dislocations in specific slip systems, steps on the surface of the crystals are formed. Such steps are commonly called slip bands or slip traces and are readily observed on the surfaces of micropillars after compression.

2.1.1 Strength

To plastically deform a crystalline metal, a certain amount of stress σ is required. Particularly, a critical shear stress resolved on a specific slip system has to be reached. Such a critical resolved shear stress τ_{CRSS} depends on microstructural aspects of the material tested. The critical resolved shear stress can be usually determined by means of Schmid's law [15]. When applying a normal stress σ to a sample, the shear component acting on the slip plane and along the slip direction can be defined as:

$$\tau_{CRSS} = \frac{F}{A_0}\cos\beta\cos\lambda = \sigma \cdot S \qquad \text{Equation 2.1}$$

where σ is the applied normal stress, i.e., force F applied on a specimen with a cross-sectional area A_0, and S is the Schmid factor, defined as the product of the $\cos \emptyset$ and $\cos \lambda$. The force acting in the slip direction, $F \cdot \cos \lambda$, is applied on the slip plane, with an area $A_0/\cos \beta$. λ is the angle between the slip direction and F, and β is the angle between F and the normal to the slip plane as illustrated in Figure 2.1.

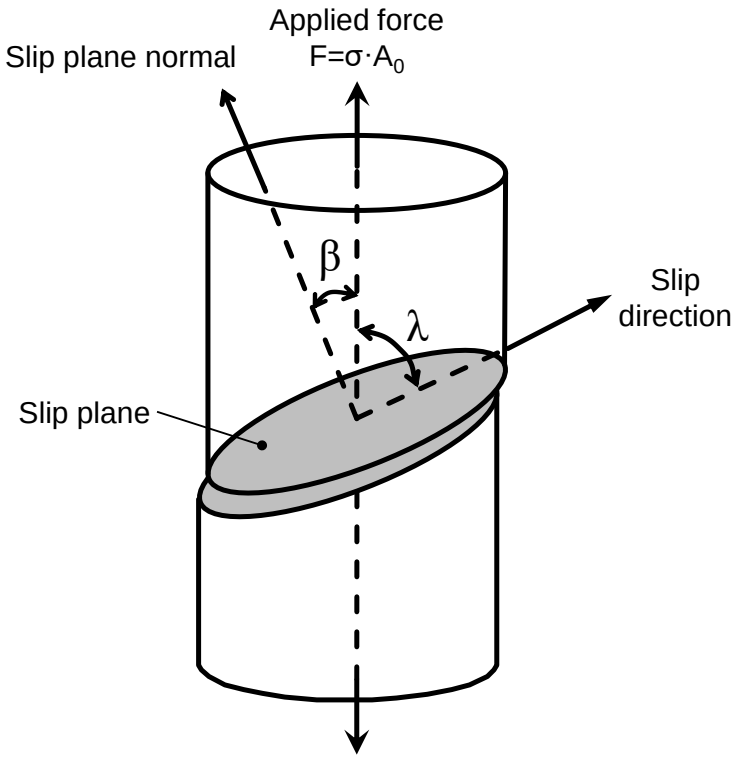

Figure 2.1: Sketch of slip in crystalline materials. The critical resolved shear stress τ_{CRSS} required for slip is commonly defined by the axial stress σ applied to the crystal and the Schmid factor S. Adapted from reference [12].

Schmid's law specifies that a slip system is activated only when the applied resolved shear stress on this system surpasses a certain critical shear stress. This has been commonly shown to apply to FCC metals [12]. However, in BCC metals, Schmid's law is not valid at low temperatures [16]. It has been observed experimentally and computationally that plastic flow follows the planes of maximum resolved shear stress (MRSS) [13,17–19] (see section 2.1.2 for further details).

2.1.1.1 Temperature and strain rate dependence

The stress required to deform a material plastically does not only depend on material features but also on test parameters such as temperature and applied strain rate. The energy required by dislocations to overcome the obstacles found during slip dictates such temperature and strain rate dependence of the flow stress. At temperatures above 0 K, atoms vibrate at a certain amplitude. The increase in thermal energy provided at higher temperatures magnifies the vibration amplitude of the atoms. Thus, the probability of an atom to overcome a so-called short-range obstacle increases. This, in turn, means that the stress needed to move a dislocation decreases with increasing temperature. The effect of strain rate is comparable to the temperature effect, but with an opposite trend. With increasing strain rate, dislocations have shorter time to overcome obstacles, which reduces the effect of thermal energy, and therefore a higher stress is required. In summary, a decrease in temperature and an increase in applied strain rate will increase the flow stress [12].

Generally, the τ_{CRSS} of a material is denoted as the contribution of an athermal τ_μ and a thermal τ^* component as follows:

$$\tau_{CRSS} = \tau_\mu(structure) + \tau^*(T, \dot{\varepsilon}, structure). \qquad \text{Equation 2.2}$$

The athermal term is related to long-range obstacles, which are commonly point defects, precipitates, grain boundaries and other dislocations. It is almost independent of temperature since there is only a slight variation coming from the shear modulus μ with temperature. The thermal term, however, is related to short-range obstacles, which include the intrinsic lattice friction that dislocations experience. This is particularly important for BCC metals and related alloys, whose deformation depend strongly on temperature and strain rate (see section 2.1.2). The thermal stress component becomes smaller with increasing temperature. Hence, above a critical temperature T_c (also known as athermal temperature or knee temperature), short-range obstacles are negligible and τ_{CRSS} is then dominated by the athermal component τ_μ.

2.1.2 Plasticity in BCC metals

The stress-strain behavior of BCC metals is strongly temperature, strain-rate and orientation dependent at temperatures below T_c [20–22]. This has been attributed to a limited mobility of the screw dislocations, caused by the nature of their cores. As the preferred slip direction for BCC metals, $\langle 111 \rangle$, lies at the junction of three $\{110\}$ and three $\{112\}$ crystallographic planes, it was postulated that, in order to account for the high yield strength of BBC metals at low temperatures, screw dislocations should spread in a threefold manner in these planes [23]. It is generally accepted that such non-planar core structure of the screw dislocations is responsible for the high lattice friction stress (Peierls stress) [14,24,25]. These features are present in all BCC metals irrespective of their interatomic bonding [26].

The critical temperature T_c is an indication of the upper limit of the temperature regime where the thermally activated mobility of screw dislocations affects the yield strength (see Figure 2.2). The value of T_c of a BCC metal is not exact since there is a rather smooth transition of the flow stress that relies slightly on strain rate. Nevertheless, the critical temperature of a BCC metal generally falls on about 20% of the melting temperature T_m [24]. Below the critical temperature T_c, the flow stress response of single crystals shows three specific regimes [20,21,24] manifested by knees that can be distinguished on the stress-temperature curves (see Figure 2.2). These are characterized by a stress-assisted, thermally activated formation of kink pairs on the screw dislocations as proposed by Seeger [24,27]. In these temperature regimes, i.e., below T_c, there is not sufficient thermal energy provided, so that screw dislocations can overcome the Peierls barrier only by forming kink pairs that push the dislocations to the adjacent potential valley [27]. In the temperature regimes III and II (see Figure 2.2), it has been found that BCC metals deform primarily by slip on $\{112\}$ planes [56, 57, 63, 66, 67]. The slip traces in these regimes are wavy and ill-defined. Such appearance is related to cross-slip, a process characterized by the shift from planes that intersect the $\langle 111 \rangle$ zone axis [12,28]. This causes the slip traces to follow the MRSS planes [42]. By contrast, in the temperature regime I, slip lines correspond to slip on $\{110\}$ planes, as shown experimentally [30, 42] and computationally [75-78], and Schmid's law applies broadly. The slip traces observed in this regime are straight. The change of slip system, from $\{112\}$ at higher temperatures to $\{110\}$ at lower temperatures, stems from a phase transition in the dislocation core. Details about this phase transition as well as kink pair theory can be found in references [14,27].

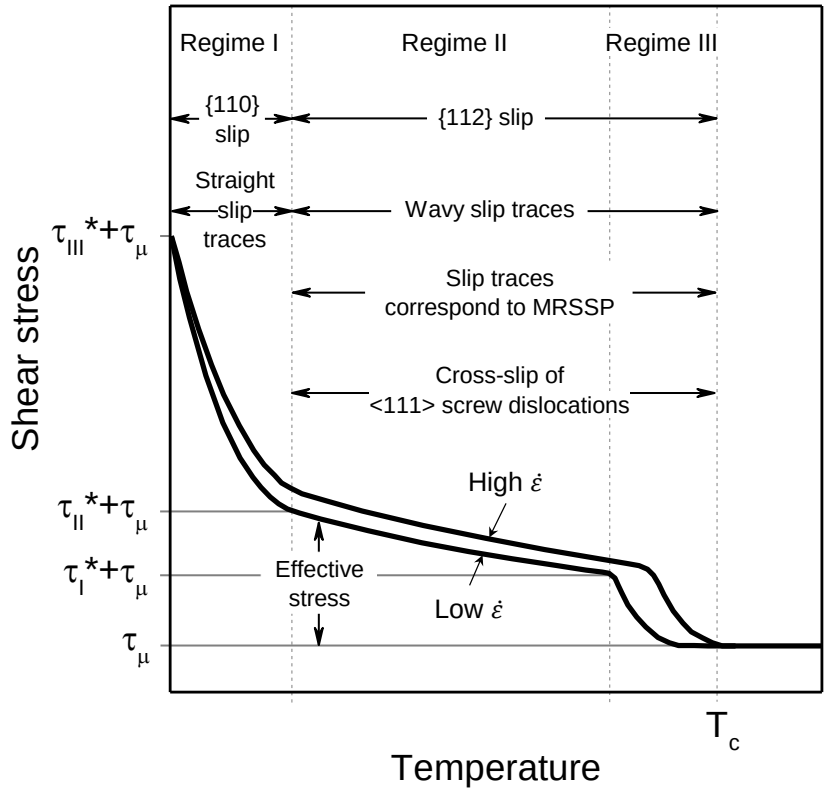

Figure 2.2: Common critical shear stress behavior of BCC metals as a function of temperature. The critical resolved shear stress τ_{CRSS} decreases with temperature and increases slightly with strain rate until a critical temperature T_c is reached. The main deformation aspects shown by BCC metals in three distinct deformation regimes below T_c are also depicted. MRSSP stands for maximum resolved shear stress planes. Adapted from references [24,28].

In the temperature regime where slip takes place on $\{112\}$ planes, the slip lines observed on compressed specimens are wavy because of the cross-slip of the $a/2\langle 111\rangle$ screw dislocations (a is the lattice constant). In this regime, the screw dislocations cross-slip led by the local stresses resolved on the $\langle 111\rangle$ slip direction. Consequently, the apparent direction of slip commonly falls onto a non-crystallographic plane that corresponds or is close to the one with the maximum shear stress resolved along the glide direction; i.e., MRSS plane [28,29]. In principle, the MRSS plane can take any orientation containing the $\langle 111\rangle$ zone axis. Therefore, it is not possible to determine the slip behavior of BCC metals deformed in an intermediate temperature regime by simply observing the slip traces on the specimen surfaces.

Researchers have commonly described the crystal orientation dependence of the yield strength of BCC metals by defining an orientation parameter χ (called Taylor angle), which is the angle between the $\{110\}$ slip plane with the largest Schmid factor and the apparent MRSS plane *M*, as illustrated in Figure 2.3. This figure represents the standard stereographic projection where *A* is the crystal orientation of a specimen tested in tension

or compression. *D* is the slip direction ⟨111⟩, and λ is the angle between the loading axis *A* and the slip direction *D*. All BCC crystals lying within the unit triangle (illustrated by bold lines) can be defined by the Taylor angle χ. It lies between -30 and 30° depending on the crystal orientation of the specimen tested as depicted in Figure 2.3 [24,30–32].

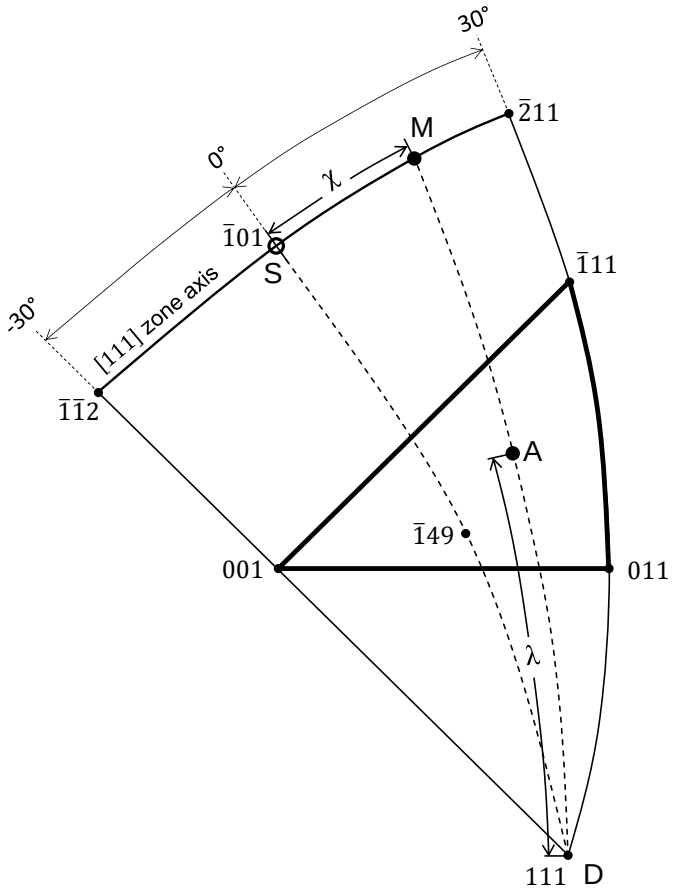

Figure 2.3: Standard (001) stereographic projection. Given a crystal orientation *A* and the slip direction *D* ([111] for BCC metals), the angle between the apparent maximum resolved shear stress plane *M* and the plane with the largest Schmid factor S={110} is defined by χ. χ ranges between -30 and +30° depending on where the crystal orientation lies within the standard triangle. λ corresponds to the angle between the uniaxial stress direction *A* and the slip direction *D*. Adapted from references [24,30].

2.1.3 Plasticity in B2 alloys

B2 alloys are a class of intermetallics that possess the CsCl type-structure and differ from the BCC structure only in that the atoms occupying the body-centered position are of different chemical species from the atoms at the corners of the unit cell. These compounds can also be considered as two interpenetrating simple cubic lattices with different chemical species (see Figure 2.4). Their macroscopic mechanical behavior has been extensively studied, particularly in the case of β-CuZn and NiAl. In fact, β-CuZn was first studied by Taylor in 1928 [30] and was the first BCC-like alloy described as having a

deformation behavior very different from those of FCC metals but similar to BCC (α-)iron. The deformation behavior of β-CuZn is similar to that of elemental BCC metals. Slip takes place along the ⟨111⟩ glide direction in either {110} or {112} planes. Furthermore, the yield strength exhibits somewhat similar temperature and orientation trends as in BCC metals, for instance, the breakdown of Schmid's law. On the contrary, NiAl deforms by cube slip along the ⟨100⟩ direction and {110} or {100} planes [33–36].

In BCC-like crystal structures, the most densely packed planes are the ones belonging to the {110} family while the most densely packed directions are the ⟨111⟩. Therefore, the $a/2\,\langle 111\rangle$ dislocation is the shortest and most energetically favored. However, B2 alloys differ in that an $a/2\,\langle 111\rangle$ dislocation does not fully restore the crystal structure. A second $a/2\,\langle 111\rangle$ dislocation is required (see Figure 2.4). Such dislocations move in pairs and are commonly called superpartial dislocations. The leading and trailing dislocations are separated by a complex stacking fault called anti-phase boundary (APB).

$$a\langle 111\rangle = a\frac{1}{2}\langle 111\rangle + APB + a\frac{1}{2}\langle 111\rangle \qquad \text{Equation 2.3}$$

Since two partial dislocations are then required to restore the crystal structure, it is sometimes more energetically favorable to have the $a\langle 100\rangle$ dislocation with the longer Burgers vector. The precise reasons for the choice of slip direction in a given B2 alloy are still under debate. However, recent computational studies indicate that a combination of elastic anisotropy, slip vectors of metastable faults and their energies dictates the slip direction [37].

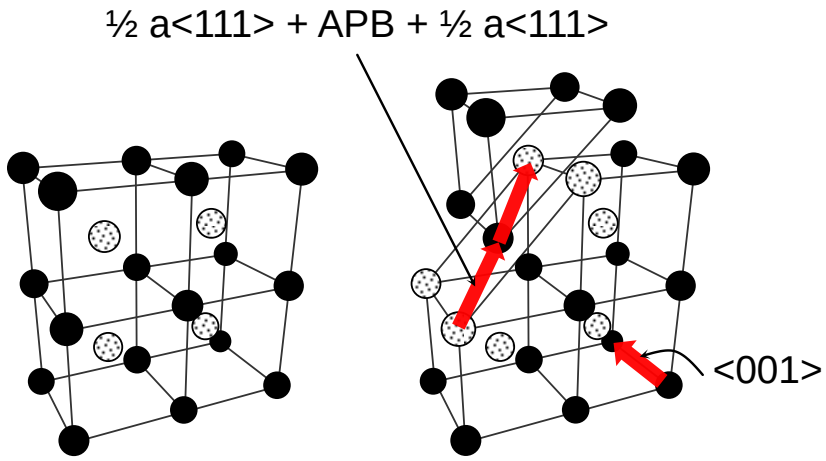

Figure 2.4: Crystal structure of B2 alloys and their main dislocation Burgers vectors ½ <111> and <100>. Adapted from reference [38].

2.1.3.1 The roles of elastic anisotropy, dislocation mobility and anti-phase boundary

In order to understand slip behavior in B2 intermetallics, it is necessary to understand the behavior of partial dislocations. In elastically isotropic crystals, dislocations with the smallest Burgers vector are more easily nucleated since their self-energy is proportional to the square of their Burgers vector [13]. Providing that they can also move easily, they dominate the plastic deformation. However, there are B2 alloys in which the ⟨111⟩ slip dominates despite the square of the Burgers vector of ⟨111⟩ dislocations is three times larger than that of ⟨100⟩ dislocations [37]. One such material is β-CuZn. It has been proposed that the anisotropic nature of B2 alloys plays a role in explaining this. Anisotropy is usually described by Zener's parameter *A*:

$$A = \frac{2 \cdot C_{44}}{C_{11} - C_{12}} \qquad \text{Equation 2.4}$$

where C_{ij} are the elastic stiffness constants. B2 metals are, in general, relatively anisotropic [39], as seen in Figure 2.5. Elastic anisotropy decreases, in most cases, the energy difference between the ⟨111⟩ and the ⟨100⟩ dislocations [37].

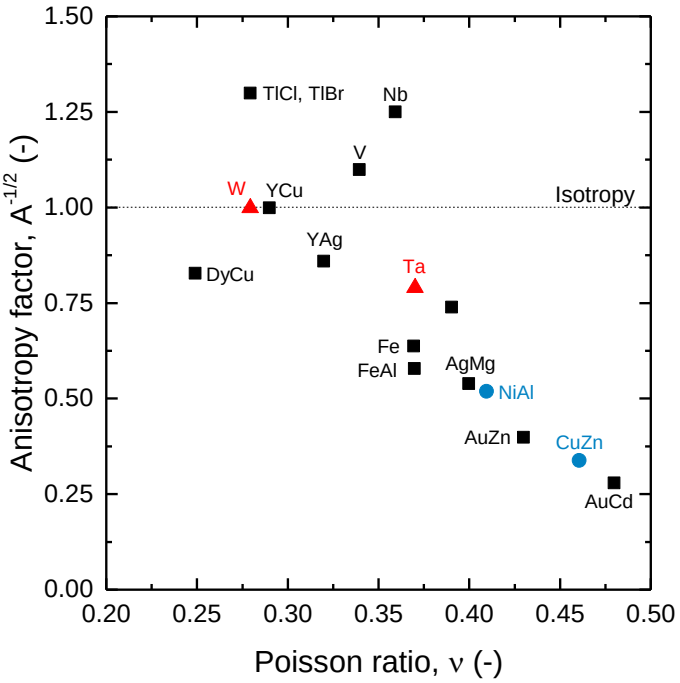

Figure 2.5: Elastic anisotropy vs. Poisson's ratio for B2 alloys and BCC metals. Depicted red triangles and blue dots are the BCC and B2 alloys employed in this work, respectively. Adapted from references [40,41].

Lin *et al.* [37] showed via dislocation energy calculations that only in β-CuZn, which is very anisotropic, does the ⟨111⟩ screw dislocation have a lower energy than the ⟨100⟩

screw dislocation. This indicates that the energy is not the only parameter that dictates slip in B2 alloys.

Dislocation glide is strongly affected by the structure and properties of dislocation cores [26]. For example, the motion of dislocations with non-planar cores can be difficult since these cores must be first transformed from their sessile (immobile) state to a glissile (mobile) state [26]. On the other hand, dislocations with planar cores are usually more mobile since their cores are already in the glissile form. It is commonly argued that in materials with well-defined stacking faults that possess low energies, dislocations can dissociate into well-separated partials, thus rendering planar dislocation cores [26]. Assuming that, in a B2 ordered alloy, the stacking fault energy is related to the order–disorder transition temperature between the ordered B2 and disordered BCC phases, a low stacking fault energy, and hence, a wide dislocation splitting can be expected [37]. An example is β-CuZn. The ⟨111⟩ superdislocations may then dissociate into two $1/2\,\langle 111\rangle$ superpartials. This decreases their energy while the dissociation of the ⟨100⟩ dislocations into partials of the same type may be energetically unfavorable. Thus, the ⟨111⟩ slip direction will be favored and, indeed, this slip direction is the principal direction of slip in β-CuZn [39,40,42–45]. However, this is also the main slip direction in stoichiometric FeAl although the order–disorder transition temperature of this compound is not particularly low [46]. In fact, it is similar to that of other B2 compounds, such as for example CoTi, in which ⟨100⟩ slip dominates [47].

In summary, these considerations suggest that deformation in B2 alloys is governed by the line tension of dislocations and their mobility. While the line tension of dislocations is strongly influenced by elastic anisotropy and possible planar faults, the mobility of the dislocations depends on their core structure [37].

2.1.3.2 β-CuZn single crystals – strength anomaly

The yield strength of β-CuZn exhibits a similar trend to BCC metals below room temperature [48,49]; it increases with decreasing temperature. This has been attributed to the conventional motion of ⟨111⟩ screw dislocations overcoming the Peierls potential [49,50], as is also the case for BCC (and FCC) metals. Post-mortem TEM investigations [42,51–53] have clearly shown that deformation takes place mainly by ⟨111⟩ partial dislocations below room temperature. Two distinct slip systems have been observed via slip trace analyses [43,49,54–56] and TEM observations [42,49]. Below 115 K, slip takes place mostly on the ⟨111⟩{112} slip system and the temperature and strain rate

dependences are very similar to those of BCC metals [49,56]. On the other hand, above this temperature, slip occurs on the $\langle 111 \rangle \{110\}$ slip system [55], a behavior opposite to that of BCC metals. Furthermore, the flow stress is relatively independent of strain rate up to room temperature [49,56]. Hanada *et al.* [56] analyzed the change of slip plane from $\{112\}$ to $\{110\}$ at higher temperatures. The energy required to move $\langle 111 \rangle$ superpartials on either $\{110\}$ or $\{112\}$ planes (E) were calculated at different temperatures by considering the elastic energies of the superpartials (E_1 and E_2) together with the APB energy ($\gamma \cdot \omega$) and interaction energy of the superpartials E_{12}:

$$E = E_1 + E_2 + E_{12} + \gamma \cdot \omega. \qquad \text{Equation 2.5}$$

Hanada *et al.* also considered anisotropy conditions as well as dislocation mobility conditions. Thus, it was determined that, at 77 K and at room temperature, slip in dissociated superpartials on $\{112\}$ planes requires less energy than on $\{110\}$ planes. They could not explain, however, why slip commonly takes place on $\{110\}$ planes at room temperature.

Unlike BCC metals and other B2 alloys, β-CuZn shows an anomalous peak in strength at intermediate temperatures, i.e., at approximately 500 K [44,48]. Between about 273 and 500 K, the yield strength increases with temperature (see Figure 2.6), in a temperature regime well below the order-disorder transition temperature of this alloy (733 K) [57]. The temperature of this anomalous peak has been shown to depend on strain rate and crystal orientation [42,44,58,59]. An increase in strain rate raises the strength anomaly strongly [58] while crystal orientations close to the $[100]$ exhibit higher peak temperatures [42,44]. Several researchers have tried to explain the plasticity mechanisms responsible for this anomalous behavior, but no agreement has yet been reached. Mainly, three different theories have been suggested in view of experimental results: the APB dragging theory [60], the cross-slip pinning theory [44] and the local climb-locking theory [52,61]. First, Beauchamp *et al.* [60] determined the energy and thickness of an APB in $\{110\}$ planes at different temperatures and observed a peak in the energy of the APB at temperatures close to the anomalous-peak temperature. Thus, it was postulated that the actual temperature dependence of the APB energy could be the responsible for such a strength-temperature anomaly. Nevertheless, concerns exist about this theory since the model cannot describe the crystal orientation dependence. Second, Umakoshi *et al.* [44] have investigated the dependence of the yield strength on temperature together with slip observations and suggested that the strength anomaly is related to the thermally activated

locking of ⟨111⟩ screw dislocations by cross-slip from {110} to {112} planes. This, however, does not explain completely how a decrease in strength is observed above the peak temperature. Thus, Saka *et al*. [52,53,61] have pointed out that the strength anomaly might be caused by a change of slip from ⟨111⟩ dislocations below the peak temperature to non-⟨111⟩ dislocations above the peak temperature (i.e, mainly ⟨100⟩ dislocations). Also, Dirras *et al.* [50] found some evidence of such slip transition, although only a limited amount of ⟨100⟩ dislocations were observed at the peak temperature through TEM. Furthermore, the increase in strength between room temperature and anomalous-peak temperature has been explained in terms of the dissociation of ⟨111⟩ dislocations, which seem to take place by climb [62,63]. Saka *et al.* [42] assessed the strength anomaly in terms of the energy of ⟨111⟩ superdislocations in the climb-dissociated and the glide-dissociated configurations. They concluded that climb-dissociation is more likely in all cases except for near-screw orientations. This has been also supported by strain rate dependent tests as a function of temperature [58], revealing that the observed positive strain rate dependence is better described by a climb mechanism. Climb is a deformation process where edge character dislocations can move out of its plane [12]. This mechanism requires diffusional events and occurs only at sufficiently elevated temperatures [12].

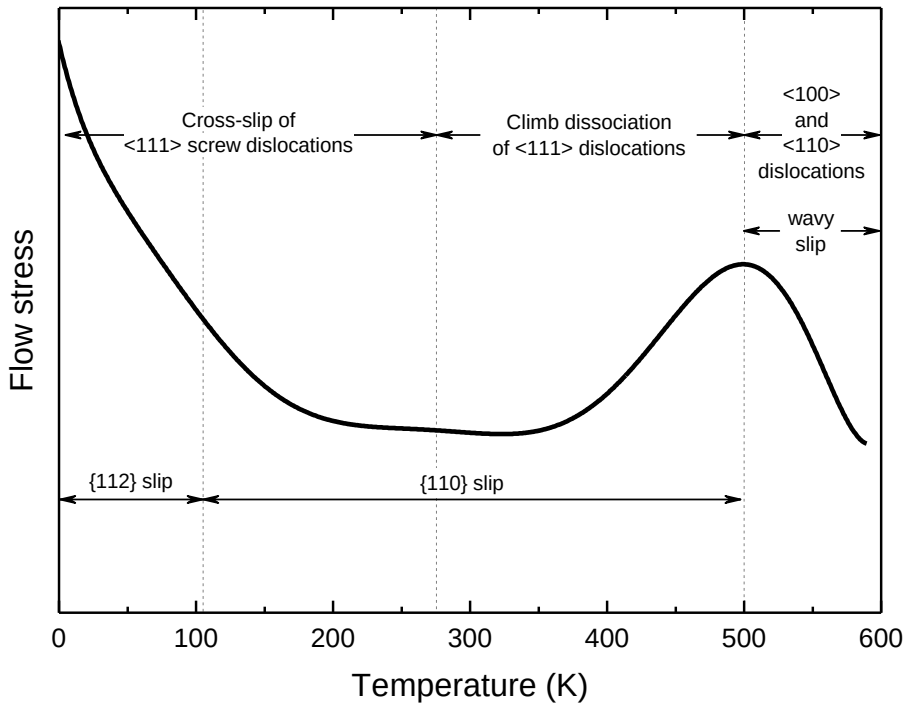

Figure 2.6: Schematic illustration of the temperature dependence of the flow stress of β-CuZn. Included are the main slip features observed experimentally via slip trace analyses and TEM studies.

2.1.3.3 NiAl single crystals

B2 alloys that slip along the ⟨100⟩ direction, such as NiAl, possess only three independent slip systems, insufficient for polycrystalline deformation [39]. Thus, they are commonly brittle. Single-crystal stoichiometric NiAl has been extensively studied, and considerable plastic deformation takes places in compression [34,36,64–66]. The temperature dependence of the yield strength is similar to that of BCC metals, which exhibits decreasing yield strength with increasing temperature. However, the yield strength depends strongly on the crystal orientation of the specimen. In Figure 2.7, the yield strength as a function of deformation temperature is depicted for different crystal orientations [67]. Two different kinds of flow stress and slip behavior are clearly observed in NiAl crystals oriented along non-⟨100⟩ directions and along the ⟨100⟩ direction. Crystals oriented along non-⟨100⟩ directions exhibit much lower yield stresses. Therefore, they are commonly referred to as 'soft' and 'hard' crystals, respectively.

The mechanical response of soft crystals has been studied in compression and in tension for a wide variety of crystal orientations and temperatures (see review by Miracle [33]). The yield strength decreases rapidly from 77 to approximately 400 K. Above this temperature, it remains rather constant or decreases slowly with temperature up to 1250 K [33,34,65] as seen in Figure 2.7. Plastic strain is observed in compression at room temperature [34,65,68,69] although tensile plastic strain is limited (between 0.5 and 2.5%) [70]. All studies on soft crystal orientations performed over a temperature range from 77 to 1273 K show that the preferred slip direction is ⟨100⟩ [33,34,36,64,67,69,70]. The active slip plane has been observed to change depending on crystal orientation. However, most of orientations slip on {110} planes [33,34,64,67,69,70]. Cross-slip on {110} planes has been reported [34,64]. In addition, other active planes have been reported for [110]-oriented crystals at temperatures ranging between room temperature and 1000 K [64,70]. These planes are (100) and (010). However, no clear explanation for it has been given. A study of the strain rate and temperature dependence of the yield stress of single crystals has revealed that, below the ductile-to-brittle temperature, the rate-controlling deformation mechanism is the nucleation of kink pairs [71].

Hard crystals, i.e., [100]-oriented crystals, usually deform by either conventional slip of ⟨111⟩ dislocations or an instability deformation mechanism called kinking [33]. This is because all possible slip systems for the common ⟨100⟩ slip vector shown in other crystal orientations have a Schmid factor of zero. Consequently, other deformation mechanisms

have to be activated to accommodate the deformation. Such crystals, therefore, exhibit significantly higher yield stresses than soft crystals. Kinking is a localized deformation mechanism distinguished by sudden load drops taking place in a jerky manner along the stress-strain curves. This is manifested as the formation of localized deformation bands that take place on planes oriented at approximately 20° from the compression axis. X-ray and TEM studies on compressed crystals suggest that the kinked bands might form by the slip of ⟨100⟩ dislocations on {110} planes although ⟨110⟩ dislocations have also been observed [66,72]. However, ⟨110⟩ dislocations were attributed to interactions between ⟨100⟩ dislocations [72]. Kinking is a phenomenon related to edge dislocations constituting two large equal and opposite tilt boundaries [66,72,73] and has also been observed in other B2 alloys such as CoTi [74]. Pairs of ⟨100⟩ edge dislocations moving in opposite directions on {110} planes form two distinct boundaries. This is caused locally by high bending stresses which produce a geometrical softening and activation of ⟨100⟩{110} slip systems [72].

Between room temperature and 600 K both kinking [33,34,66,68,75,76] and conventional deformation by ⟨111⟩ slip on {110} and {112} planes [33,36,68,76] have been reported. The specific mechanism controlling the deformation of hard crystals seems to be determined by an interplay between deformation temperature and strain rate [66]. The aspect ratio of the tested sample also affects the deformation mechanism [77]. If the aspect ratio of a sample is large, the bending stresses can induce slip on unfavorable slip systems, and kinking seems to occur as an alternative deformation mode. By contrast, if the aspect ratio is small, kinking cannot be induced, and therefore, NiAl deforms by slip of ⟨111⟩ dislocations, which are less favorable than ⟨100⟩ dislocations. Kinking has been reported to be favored for large aspect ratios (>2.4) [33,77] and high strain rates ($>10^{-4}$ s^{-1}) [68].

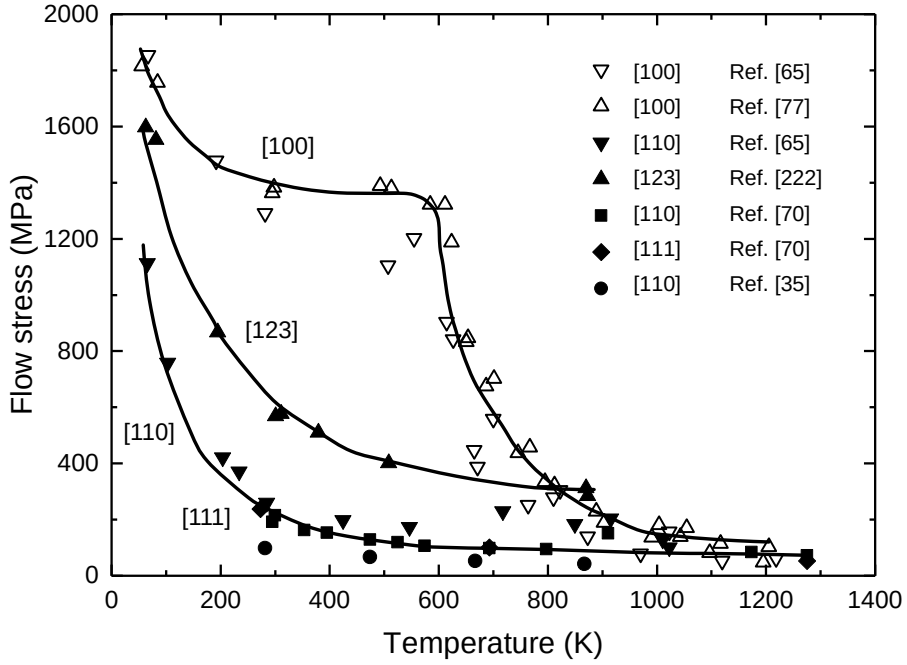

Figure 2.7: Flow stress as a function of temperature for different NiAl single crystals. Adapted from reference [67].

2.2 Size effects in small-scale metal structures

Mechanical properties can change drastically when the specimen size scale is small. The properties of most materials are well known and constitutive models are available at large size scales (above ca. 1 mm). However, the stress-strain curves obtained from classical continuum plasticity models are size independent. Controversy exists at small scales, where there exists the so-called 'size-effect', in which the strength of a material increases when the structure is small or when only a small volume deforms.

Size effects can be split into two groups: intrinsic or extrinsic, as established by Arzt [1] in 1998. Intrinsic size effects are caused by microstructural constraints such as grain size or second phase particles. Such effects are mainly controlled by the processing of materials. On the other hand, extrinsic size effects are regulated by dimensional constraints, i.e., small sample size, where certain mechanisms such as dislocation motion start to be affected by surfaces or interfaces. In many applications, such as thin films, both size effects are present and the interactions between them are very important, but current understanding is limited. In this work, we focus our attention on extrinsic size effects arising in uniaxial deformation of crystals.

Size effects in materials have been commonly studied using the nanoindentation technique due to the ease of varying the deformation length-scale and the high resolution load-displacement data that is obtained. At small length scales, discrete displacement bursts [78–80] have often been observed and associated with dislocation nucleation events in metals. Depth-dependent hardness is observed and is often described as a strain gradient effect [81] at larger size scales. Nevertheless, the inhomogeneous strain field applied during indentation makes such data difficult to interpret. Sample size effects have also been studied in thin film systems [2], where the thickness of the film is the critical length scale. In addition to their technological relevance, the attractiveness of studying thin films is the ease of sample preparation. However, since grain size often scales with the film thickness, separating microstructure effects from sample size effects is complicated. Moreover, for films on substrates, the substrate is inherently involved in the mechanical behavior; where temperature changes are used to load the film, such as for wafer curvature experiments, the thermal and mechanical effects are combined. In the case of freestanding films, problems with limited ductility, transverse buckling and tearing are often encountered.

A decade ago, a new methodology to study the size scale effects in crystalline plasticity was introduced by Uchic *et al.* [4]: micropillar compression. In this technique, FIB machined micropillars are compressed using high resolution loading with a nanoindenter equipped with a flat punch. The simple loading state is used to avoid the strain gradients present in indentation tests while allowing small-volume investigations. This generally simplifies the interpretation of the results compared to nanoindentation. The use of this technique has invariably shown the importance of sample dimensions for the strength of materials, being able to discern intrinsic from extrinsic effects. Micropillar compression studies have mainly focused on simple metals, in particular materials that possess the FCC crystal structure [4,82–93] and BCC crystal structure [6–8,88,89,94–101]. These studies have revealed that the yield strength in metals is size dependent even for unconstrained geometries and the absence of strain gradients, showing an inverse power-law effect in which the yield strength increases with decreasing sample size (see Zhu *et al.* [102], Uchic *et al.* [5], Kraft *et al.* [103] and Greer and De Hosson [104] reviews). However, such a size dependence has been shown to be strongly dependent on the presence of initial defects within the pillar microstructure [105]. A study by Bei *et al.* [105] on Mo revealed that such a size dependence relies on the presence of dislocations prior to compression. Single crystalline Mo micropillars were produced with different

initial dislocation densities. This was achieved by manufacturing directionally solidified Mo pillars and pre-straining them to different extents. With such a method, it was observed that dislocation-free pillars and pillars with a high initial dislocation density showed no size dependence whereas pillars with a moderate initial dislocation density showed a clear size dependence. In addition, dislocation-free pillars exhibited yield stresses close to the theoretical yield stress, while the pillars with the highest initial dislocation density revealed the lowest strength.

Due to the fact that, in these studies, the micropillars were single crystalline, the increase in strength cannot be explained by the existence of obstacles to dislocation motion such as grain boundaries. Thus, the reduction in sample size must affect the deformation mechanisms related to the nucleation, multiplication and pile-up of defects [4].

2.2.1 Theories of size effect in micropillar testing

Different theories have been put forward to explain the compressive behavior of nano- and micropillars. A classical explanation is the so-called 'dislocation multiplication', which is based on Taylor hardening [106]. The increase of dislocation density promotes the interaction of dislocations, thus limiting their movement. Nevertheless, Greer *et al.* [85] have discussed that dislocations can leave the pillar at the surface before multiplying and interacting. They proposed a 'dislocation starvation' mechanism [85,86,107]. The model is based on a condition of dislocation depletion caused by a higher probability of mobile dislocations to annihilate at free surfaces than to interact with other dislocations and multiply. As a result, new dislocations have to be nucleated from dislocation sources, and therefore a higher stress is needed to deform the crystal. Two-dimensional discrete dislocation simulations [108–110] as well as post-mortem TEM investigations [85,93] and *in situ* TEM pillar compressions [82] have supported this theory. Nevertheless, it has only been proven experimentally for pillars smaller than 300 nm in diameter. Shan *et al.* [82] showed via *in situ* TEM experiments that dislocations present in pillars with diameters in the range of 200 to 300 nm leave the pillar during initial compression, thus providing evidence of dislocation starvation (also called mechanical annealing). On the contrary, it was reported that dislocations remained in bigger pillars. Post-mortem TEM experiments support these results, where an increase in the dislocation density for sub-micrometer ⟨111⟩ Ni pillars [84] and for ⟨269⟩ Ni micropillars [111] was observed.

Another proposed model is the 'dislocation nucleation' mechanism [87,102,112], originally proposed for whiskers (free-defect structures). According to this, the high strength in pillars depends on the difficulty to activate dislocation sources. Von Blanckenhagen *et al.* [112] reported that the critical stress to pull out a dislocation segment for a given source size is

$$\tau_{source} = \frac{\mu b}{2\pi} \cdot \frac{1}{d} \cdot \ln\left(\frac{od}{b}\right), \qquad \text{Equation 2.6}$$

where μ is the shear modulus, b the Burgers vector, d the source size and o a numerical constant. The optimum source size, regarding operating the source at low stress levels, is between 1/3 and 1/4 of the limiting dimension, i.e., the pillar diameter. Therefore, this mechanism predicts an inverse power-law of the flow stress with the pillar diameter.

A related interpretation for the size effect was proposed by Parthasarathy *et al.* [113] and further extended by Rao *et al.* [114] through three-dimensional dislocation simulations. They formulated a hardening mechanism based on the availability of dislocation sources and formation of single-arm dislocation sources (source truncation). A Frank Read source operating in the vicinity of a free surface leads to the formation of two single-arm dislocation sources once the dislocation meets a surface. The length of the single-arm source can be small compared to the length of the original Frank Read source. Hence, higher stresses are needed for their activity. The shortest distance between the pinning point and the surface is the limiting configuration for the single-arm sources. On the other hand, the weakest single ended source, i.e., the one with the longest critical arm length, determines the flow stress for double-ended sources. In addition, Rao *et al.* [114] defined the concept of exhaustion hardening, which relates to the sample hardening caused when a dislocation source ceases its operation. A main aspect of this mechanism is that dislocations do not necessarily need to annihilate at the pillar free surfaces [115]. Single ended dislocation source activity has been observed computationally [108,116,117] and experimentally via *in situ* TEM pillar testing [118]. Parthasarathy *et al.* have demonstrated that the model can account for the experimental yield stresses of Ni and Au micropillars [113]. The model can be described as follows:

$$\tau_{CRSS} = \tau_0 + 0.5\mu b\sqrt{\rho_{tot}} + \frac{\alpha\mu b}{\bar{\lambda}_{max}(d,\rho_{tot},\beta)} \cong \tau_{bulk} + \tau_{size\ dependent}, \qquad \text{Equation 2.7}$$

where the critical resolved shear stress of a pillar with a diameter d directly depends on the lattice resistance of the material in shear, τ_0, a Taylor-hardening term comprising the total dislocation density, ρ_{tot}, and a size-dependent term (further discussed in chapter 4).

In this case, size effects stem from the stress needed to operate a single-arm dislocation source, which scales with the pillar diameter. Higher stresses are required to operate the short single-arm dislocation source in smaller micropillars.

The last model which is under discussion is the 'dislocation pile-up' [119] model. Kiener *et al.* [91] discussed that gallium surface layers induced by FIB machining, passivation layers or surface oxides could act as obstacles, creating dislocation pile-ups [120]. This model is based on the concentration of dislocations in few glide systems due to the presence of a limited number of dislocation sources when the specimen is in the sub-micron or micron size scale. Thus, dislocation pile-ups affect the dislocation sources by strong back stresses. According to Friedman and Chrzan [121], the stress necessary to operate a dislocation source is similar to the Hall-Petch formulation:

$$\sigma = \left(\frac{4\mu b\sigma_i}{\pi d} + \sigma_S^2\right)^{1/2} \qquad \text{Equation 2.8}$$

where σ is the applied stress, σ_i the strength of the interface, d the critical length scale and σ_s the source strength. Therefore, an inverse scaling of the flow stress with the square root of the critical length scale results from the back-stress obtained from the dislocation pile-up [121–123].

Although these plasticity phenomena may be valid for specific cases, it is more than likely that they interact with each other as shown by Kiener and Minor through *in situ* TEM observations [124]. For instance, dislocation starvation has been proven to occur for small pillars, while the operation of single-arm dislocation sources and dislocation multiplication may be predominant for relatively large pillars as higher dislocation densities may provide more chances. Dislocation source nucleation/source-truncation and dislocation starvation/exhaustion hardening might be able to co-exist in the same system. Also, the damage produced by FIB milling may affect deformation (discussed in section 3.6). Thus, it is plausible that the microstructure and size of the pillar as well as the testing parameters may dictate which mechanism is dominant [125].

2.2.2 Characteristic stress-strain behavior

A characteristic phenomenon observed during micropillar deformation is an intermittency of plastic flow [5,126,127], different from bulk metal compression, where a continuous and smooth stress-strain response is usually observed. Such intermittency is manifested on the stress-strain curves in different manners depending on the testing system

employed. Nanoindenters commonly used to perform compression tests are either load controlled or displacement controlled, thus dictating the sample response. Discrete bursts of strain are usually obtained in load-controlled micropillar compression, where strain bursts almost without any strain hardening and separated by regimes of nearly elastic loading are observed. This is the result of imposing a constant stress rate. On the other hand, a serrated stress response commonly takes place when micropillars are compressed in displacement control mode. Since a constant displacement rate is imposed in these systems, any strain instability is attenuated by producing a sudden stress drop and shortening of a strain burst [5]. Thus, the fact of using one testing mode or another produces noticeable differences in the stress-strain response of micropillars that must be borne in mind when analyzing size effects.

2.2.3 Size effects in FCC Metals

Typically, researchers have empirically described the size dependence on strength of sub-micron and micropillars by a power-law:

$$\sigma_y = \sigma_0 + kd^n \propto kd^n, \qquad \text{Equation 2.9}$$

where σ_y is the yield strength of the structure, σ_0 the bulk strength of the material, d the characteristic length scale (pillar diameter), k a constant and n the scaling exponent. Matching experimental data to the power-law requires fitting the data to extract the scaling exponent n (see Figure 2.8). This is usually carried out by plotting the experimental data on log-log plots of strength as a function of size, and then drawing the best-fit line. Thus, all the studies on FCC micropillars show a power-law relationship between pillar diameter d and yield strength σ_y, often expressed as in Equation 2.9. Through several studies on FCC metals, it has been demonstrated that the size effect exponent n falls in the range of -0.6 to -1.0 [5,83,84,86,87,91,93,104,128–130]. The bulk yield stress σ_0 is usually negligible as it is significantly smaller than $k \cdot d^n$ [5,131]. When the shear stress values of the different FCC metal studies are normalized with the material specific shear modulus μ and Burgers vector b, the values converge into a band over a size range in which the best fit corresponds to an exponent of approximately -0.6 [5,131] as seen in Figure 2.8.

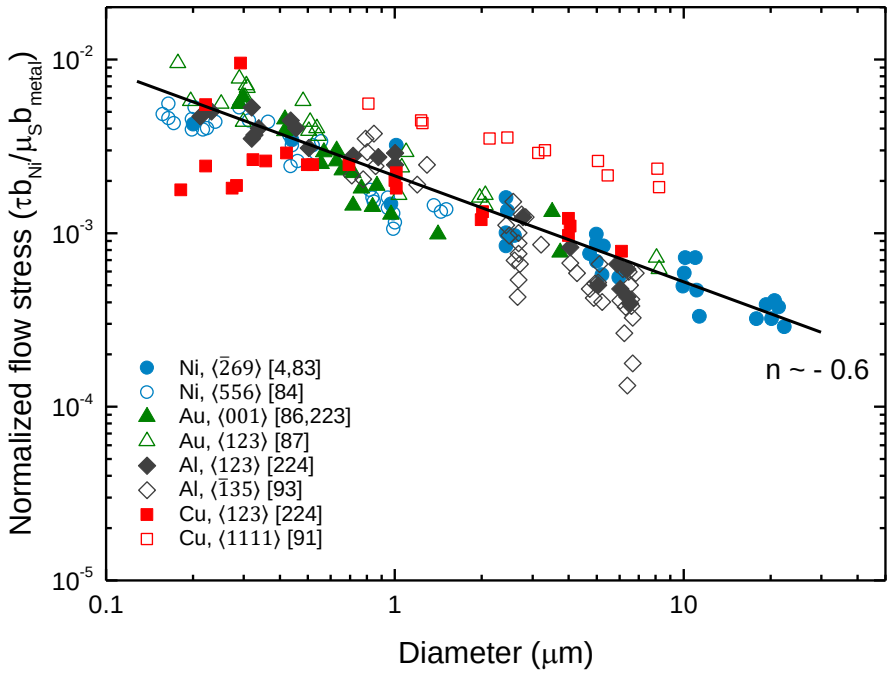

Figure 2.8: Plot of normalized flow stress data against sample diameter for different FCC metals. Adapted from reference [5].

2.2.4 Size effects in BCC metals

Plasticity in BCC metals inherently differs from that in FCC metals; the deformation of BCC metals is rather dependent on temperature, strain rate and crystal orientation [14,21]. This dissimilarity stems from the complex behavior of screw dislocations. Screw dislocations are less mobile than edge dislocations in BCC metals [14], thus controlling the deformation of these metals. The core of the screw dislocations in BCC metals is non-planar. It is particularly characterized by the three-fold symmetry of screw dislocations [20–22], which leads to a relatively high Peierls potential. Therefore, the screw dislocations have to overcome such a potential by a thermally activated process [20–22].

Several experimental studies on BCC metals including W, Mo, Ta, V, Nb and Fe [6–8,88,89,94–101,132–137] have reported lower size dependence relative to FCC metals as well as different degree of size dependency depending on the material, as seen in Table 2.1. However, it must be noted that the size effect in BCC metals has been determined, in most studies, without considering the contribution of bulk stresses, which are often in the order of hundreds of MPa's for BCC metals and should not be neglected [101,138].

Table 2.1: Comparison of power-law exponents for different BCC metals. The values reported can be described by Equation 2.9 when the flow stress at 5% strain is considered for pillars ranging in diameter from 0.2 to 6 μm.

Material	**Power-law exponent *n***
W, [100]	-0.21 (Ref. [7])
Mo, [100]	-0.38 (Ref. [7])
Ta, [100]	-0.42 (Ref. [101]) and -0,41 (Ref. [7])
Ta, [111]	-0.38 (Ref. [101])
Nb, [001]	-0.48 (Ref. [7])
Fe, [001]	-0.59 (Ref. [137]

The room-temperature strength of Mo, Nb, Ta and W has been extensively investigated at the micron and sub-micron scale via compression of FIB machined pillars with diameters ranging from 200 nm to 6 μm [6–8,88,89,94–101,132,134–136]. In particular, Schneider *et al.* [139] carefully compared the experimental results with other studies as well as theories such as starvation and nucleation theory. Through these experiments, it was found that the yield stress, the strain-hardening rate and the frequency of the strain bursts increase with decreasing sample size. The stress-strain curves exhibited strain burst behavior similar to that observed for FCC pillars, which is characteristic for the activation and subsequent exhaustion of dislocation sources [82]. More importantly, a correlation between the so-called critical temperature T_c and the strength of small-scale BCC pillars was determined, suggesting that the mobility of the screw dislocations is an important parameter for the deformation of small-scale BCC micropillars [7].

Figure 2.9 shows the power-law exponent for BCC and FCC pillars as a function of the ratio of T_{test} to T_c, which is used as a measure for the thermal activation of the screw dislocations. A larger ratio means higher thermal activation and therefore higher mobility of the screw dislocations. The extrapolation of the linear fit to lower critical temperatures leads to an exponent of about -0.6 for $T_c = T_{test,}$ which corresponds to the condition where screw and edge dislocations have equal mobility (see Figure 2.9b) and to exponents found for FCC metal pillars [83,87].

Mo, Nb and W micropillars oriented along the [100] and [235] directions were used to study the influence of orientation on the size effect [97]. The studies of Brinckmann *et al.* [96] as well as dislocation and molecular dynamics simulations by Greer *et al.* [89] and Weinberger and Cai [140] have shown that the low mobility of the screw dislocations could enhance dislocation-dislocation interactions in BCC pillars. However, Schneider *et*

al. [97] suggested that dislocation-dislocation interactions are not responsible for the size effect in BCC metals as the same effect was found for single and multiple slip orientations. On the contrary, the influence of T_{test}/T_c suggests that the low mobility of screw dislocations determines the different size dependence of FCC and BCC metals. Furthermore, the fact that the BCC size effect is increased and approaches the values of FCC pillars for a ratio of T_{test}/T_c close to one indicates that, besides the screw dislocation mobility, the size dependence of BCC and FCC pillars is controlled by similar dislocation processes such as dislocation nucleation. As possible explanations for this behavior, the kinetic pile-ups of screw dislocations [6] and kink nucleation at the pillar surface [140] were proposed. Nevertheless, neither of these mechanisms has been confirmed. Schneider *et al.* [139] carried out further experiments to correlate the activation volume and pillar diameter for BCC pillars and estimated which mechanism of both is more favorable to occur. It was found that the activation volumes calculated were in the order of $1b^3$ to $9b^3$. Comparable activation volume values were also reported by Kim *et al.* [98], suggesting that time-dependent deformation is most likely caused by the thermally activated kink-pair formation on screw dislocations. Besides this, it was suggested that kinks may be favorably nucleated at the surface of the pillar with decreasing pillar diameter, and hence less thermal energy is needed for screw dislocation motion.

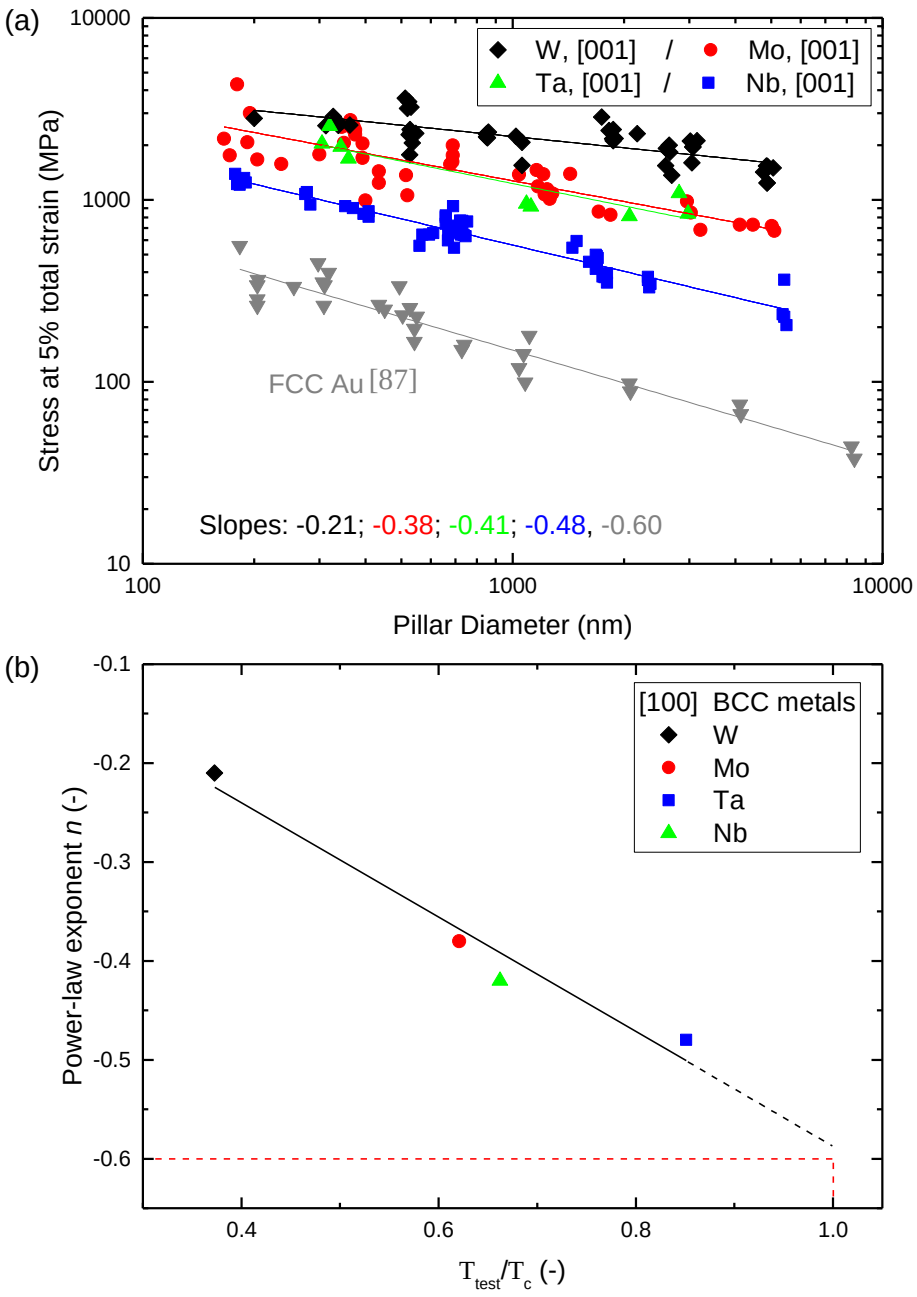

Figure 2.9: (a) Size dependence of the yield stress for BCC metals, and (b) the power-law exponent as a function of the ratio T_{test}/T_c (taken from Ref. [7]).

2.2.4.1 Influence of test temperature on the size effect of small-scale BCC structures

The influence of temperature on the size effect of small-scale BCC pillars has hardly been studied. Very recently Schneider *et al.* [8] have presented results about the influence of test temperature on the size effect of [110]-oriented Mo small-scale compression pillars. The aim of this work was to study the size dependent deformation behavior of BCC Mo at 500 K, a temperature above T_c (480 K [141]).

It was reported that the yield stress measured at 5% strain increased with decreasing diameter regardless of the test temperature. Nevertheless, the test temperature had a

significant effect on the yield stress as seen in Figure 2.10, where size exponents of -0.32 and -0.59 were determined at room temperature – which is similar to those previously published by Schneider *et al.* [7] and Kim *et al.* [98] for [001] and [235] Mo pillars – and at 500 K, respectively. The size dependence of the Mo pillars tested at 500 K resembles the one shown for FCC pillars (-0.6 [5]). Thus, it was concluded that such results support the interpretation of earlier experiments performed at room temperature [7,97], which indicated that the screw dislocation mobility strongly influences the size dependence of the BCC pillars. The better mobility of the screw dislocations above T_c allowed the BCC pillars to deform as observed in FCC pillars. Therefore, it was suggested that the mechanisms which control the size dependence of the BCC pillars may be the same as the ones to control the FCC size effect: source truncation [113] and/or dislocation starvation/ mechanical annealing [82,90].

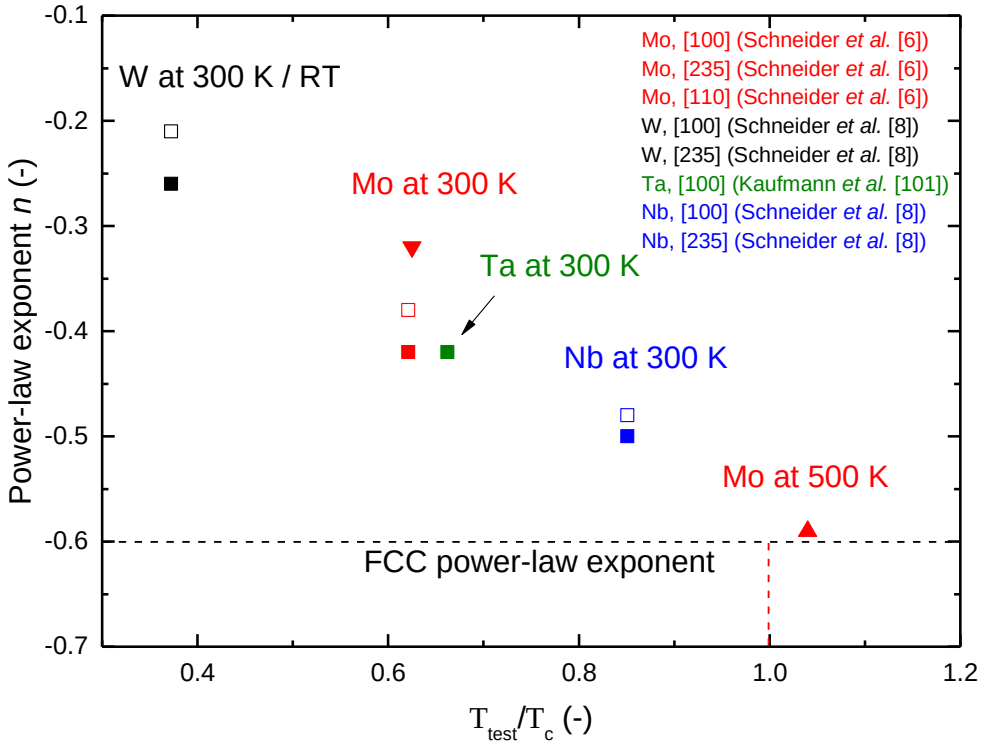

Figure 2.10: Data of size effect exponents as a function of the ratio of T_{test} to T_c for different BCC metals. The dashed black line corresponds to the power-law exponent of FCC metals, constant along the whole T_{test}/T_c range (adapted from Ref. [8]).

On the contrary, Lee *et al.* [132] compressed [001]-oriented W and Nb sub-micron pillars (from 400 to 1300 nm in diameter) far below the T_c of these materials, at 165 K. The results showed a decrease in the size effect with decreasing T_{test}/T_c. However, the scaling effect cannot be directly compared to the values of Schneider *et al.* [8] since smaller pillars and a different yield criterion were used.

2.2.5 Dependence of the size effect on the flow stress of bulk materials

Over the last few years, it has been discussed how to interpret the data obtained from compression of micropillars, suggesting that there is some degree of dependence of the size effect on the flow stress of bulk materials.

Firstly, Uchic *et al.* [5,127] and Dou and Derby [131] studied the size effect in different FCC metals and proposed different ways of plotting the measured yield stresses based on Equation 2.9. As seen in Figure 2.8, proposed by Uchic *et al.* [5], all FCC metals are found to converge on a linear fit between pillar diameter and yield stress with an exponent *n* of -0.6. However, Dou and Derby [131] discussed that the normalization of the Burgers vector of each material by that of nickel, as presented by Uchic *et al.* [5], was not very intuitive. Therefore, they proposed to plot the size effect using dimensionless variables on both axes: the critical resolved shear stress τ_{CRSS} normalized by the shear modulus μ as a function of the pillar diameter d normalized by the Burgers vector b. Hence, based on Equation 2.9, the following relationship was assumed [131]:

$$\frac{\tau_{CRSS}}{\mu} = A\left(\frac{d}{b}\right)^{n} \qquad \text{Equation 2.10}$$

Secondly, Korte and Clegg [138] noted that any assumption as to what mechanism is operative should be avoided due to the differences in controlling length scale, which might be expected between the different types of materials. Therefore, they suggested the following form to fit the data:

$$\frac{\tau_{CRSS} - \tau_0}{\mu} = A'(d)^{n} \qquad \text{Equation 2.11}$$

where τ_0 is the bulk material flow stress resolved on the slip plane, and A' and n are the fitting variables. It was argued that on one hand, for soft metals, the same fitting parameters as the ones presented in literature are expected since $\tau \approx \tau - \tau_0$ for $\tau >> \tau_0$. On the other hand, for harder metals such as BCC metals, subtraction of the bulk flow stress would result in a better comparison since it would separate the increase in yield stress due to size from the intrinsically high strength of these materials. However, Korte and Clegg [138] were not able to fit their data in this way as an accurate determination of τ_0 was not possible. The main problems encountered in determining a representative τ_0 were the dependence of τ_0 on dislocation density and strain rate.

Later, Lee and Nix [142] proposed a power-law relationship similar to that of Korte and Clegg. They carefully analyzed the effect of different material parameters, dislocation density and temperature on the size dependence of FCC and BCC micropillars by using Parthasarathy's model [113] (see Equation 2.7), and suggested the following universal scaling law:

$$\frac{\tau_{CRSS} - \tau_0}{\mu \cdot b} = A''(d)^n \quad . \qquad \text{Equation 2.12}$$

The proposed relationship is the same as the one Korte and Clegg elucidated, but includes the magnitude of the Burgers vector *b*. This was rationalized for FCC and BCC micropillars that present an initial dislocation density of about 10^{12} m^{-2}. Furthermore, Lee and Nix indicated that the main factor responsible for the different size effects shown by FCC and BCC metals might be the magnitude of bulk stress (friction stress) τ_0, which is temperature-dependent.

Last, Han *et al.* [143] investigated the effect of the bulk yield stress on the size effect of BCC micropillars in a similar approach as Korte and Clegg [138]. A size effect model dependent on the critical temperature, i.e., the Peierls stress, was presented in this study. Based on strengthening factors such as lattice friction and dislocation elastic interactions that contribute to yield stress [142], the yield stress of a micropillar can be expressed as:

$$\sigma_y = \frac{\tau_p}{S} + \sigma_x \qquad \text{Equation 2.13}$$

with τ_P as the Peierls stress, which does not depend on the pillar size *d*, *S* as the Schmid factor and σ_x as the yield strength depending on strengthening factors different from the Peierls lattice friction, such as the activation stress for dislocation sources and the stress associated with dislocation interactions [142].

In this study, it was considered that, when the testing temperature is higher than T_c, the Peierls stress can be neglected, so that the strengthening mechanism is similar to that of FCC metals with the size-effect exponent *n* in the range of -0.6 to -1.0:

$$\sigma_y \approx \sigma_x = A \cdot d^n \qquad \text{Equation 2.14}$$

On the other hand, when $T<T_c$, such as for Mo, Ta and W, the effect of the Peierls stress cannot be neglected as it may be as high as 800 MPa for BCC metals [144,145]. Therefore, the following model was assumed:

$$\sigma_y = \frac{\tau_p}{S} + \sigma_x = \frac{\tau_p}{S} + A \cdot d^n = B \cdot d^{\beta} \qquad \text{with } -0.6 > n > -1.0 \qquad \text{Equation 2.15}$$

where B and β would be the size-effect exponents commonly used to fit the results. From the mathematical point of view, it is clear that the exponent β is always smaller than n (see Figure 2.11), showing that the Peierls stress cannot be disregarded when determining the size effect in BCC micropillars. Moreover, it was deduced that n would decrease with increasing Peierls stress. Figure 2.11 depicts the aforementioned. The room-temperature size effect in [001]-oriented V was determined to be $n \approx -0.79$. Since V presents a T_c in the range of 200 - 380 K (room-temperature values), the Peierls stress τ_P was considered to be zero. Nevertheless, if a larger Peierls stress were considered, for instance 72 or 293 MPa, the effective yield stress could be calculated by summing τ_P/S to each V data point. Hence, the 'imaginary' size effects β would be 0.57 and 0.34, respectively, matching the size exponent shown by single crystalline Mo micropillars.

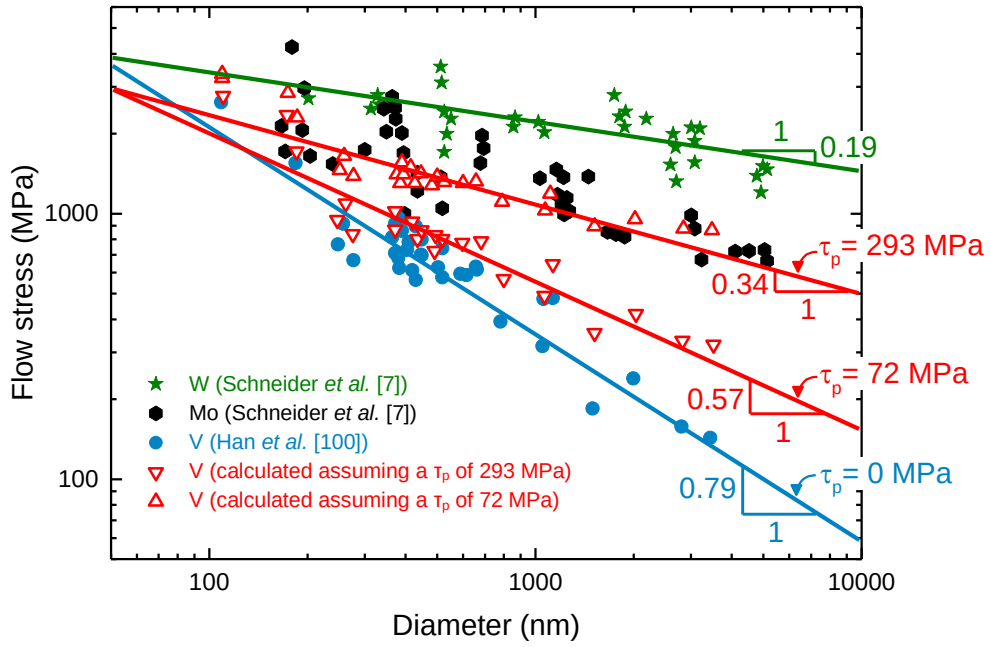

Figure 2.11: Flow stress against pillar size for W, Mo, and V. The V data (solid circles) are taken from the work by Han *et al.* [100] and the W and Mo data are taken from Schneider *et al.* [7]. Furthermore, two data sets for V are also shown and calculated using Equation 2.15 based on the V data (solid circles) and the corresponding τ_p (adapted from Ref. [143]).

All these studies indicate that bulk stresses influence the measured power-law exponent. However, no clear evidence has been provided until very recently. Soler *et al.* [146] evaluated the role of the lattice resistance on the size effect. Chemically etched LiF micropillars (an ionic compound) were manufactured with a defined initial dislocation density. Subsequently, they were compressed at different temperatures. By knowing the initial dislocation density and using Parthasarathy's model, the researchers asserted that size effects on strength emerge from the relative contributions of bulk stresses and size-dependent stresses. At room temperature, bulk stresses governed the inexistence of size

effect, whereas at 250 °C, both contributions were similar, hence bringing about a considerably large size effect.

2.3 Summary and motivation

The mechanical behavior of bulk BCC-based metals and alloys has been extensively studied. It was not until the late 1920's that the defect peculiarities of these metals, responsible for their mechanical properties, started to be studied in depth thanks to the advent and development of transmission electron microscopy. On the other hand, microcompression testing has become a suitable technique to study deformation processes at the nano- and microscale. Through this technique, it has been repeatedly demonstrated that sample size-dependent strengthening effects may arise independently of grain size or the existence of strain gradients. The literature review shows that, over the last decade, a certain amount of research has been carried out to study size effects in BCC micropillars at room temperature. These studies revealed that the size dependence of BCC metals is essentially different to that of FCC metals. More importantly, it was shown that this size dependence relies strongly on a relative temperature ratio between the test temperature and the critical temperature characteristic of the material [7], thus indicating that screw dislocations play a crucial role on the deformation of BCC metals at the nano- and microscale. Despite this, only very recently, Schneider *et al.* [8] and Lee *et al.* [132] have studied the size effect in BCC micropillars at different temperatures.

To date, no effort has been made to systematically study the paired effects of temperature and specimen size on the plasticity of BCC metals. The current findings are not conclusive and further research is required to fully understand the deformation behavior of BCC metals in small volumes and their differences with respect to better-studied metal classes such as FCC metals. An open question is whether the temperature will influence strongly the flow stress in small volumes, as is the case for bulk samples [20,21], and whether the underlying dislocation mechanisms will be the same. Furthermore, the deformation behavior, at the sub-micron and microscale, of other metals with a BCC-based crystal structure is completely unexplored. This is the case of B2 alloys such as β-CuZn and NiAl, for which the influence of elastic and plastic anisotropy as well as screw dislocation mobility (lattice resistance) at the nano- and microscale is not known.

With that, this thesis focuses on consistently studying the influence of bulk strength, more precisely, the influence of lattice resistance on size dependent strengthening effects. This will in turn shed light not only on the comprehension of the plasticity mechanisms responsible for the deformation of BCC-based metals and alloys in small volumes, but will also serve as a guideline to improve the mechanical properties of micron-sized devices.

The size effect on the strength of W, Ta, β-CuZn and NiAl will be studied in a size regime between 200 nm and 5 µm in diameter. For this, single crystal micropillars will be manufactured using the FIB technique and further compressed at different testing conditions using instrumented nanoindentation testing inside an SEM. The influence of temperature on the plasticity of BCC W and Ta metal micropillars will be studied systematically up to 400 °C to determine the extent of the Peierls potential at this scale. The results of these experiments will be the main topic of chapter 4. The influence of the sample size and crystal orientation on the room-temperature strength of β-CuZn and NiAl micropillars will be the main subject in chapters 5 and 6, respectively. For both alloys, pillars oriented for single and multiple slip will be compressed. Furthermore, the loading rate will be varied to examine strain rate sensitivities, thus insights into the deformation rate limiting mechanisms are assessed. For all materials tested, the effects of temperature, sample size and loading rate on the stress-strain and deformation behaviors will be carefully analyzed with regard to BCC screw dislocation theory and microscale plasticity models.

3 Experimental methods

The fabrication as well as the mechanical characterization of micropillars are not trivial tasks to perform. Special care must be taken at each step in order to precisely manufacture specimens and interpret the data obtained from nanomechanical tests since the results may be significantly influenced by experimental artifacts. This chapter describes the methods employed to produce, test in compression and characterize focused ion beam machined micropillars. Furthermore, the different experimental constraints that these methods exhibit are reviewed.

3.1 Sample preparation

3.1.1 Bulk sample preparation

As model metals with a BCC and a B2 crystal structure, single crystals of W and Ta as well as β-CuZn and NiAl polycrystalline samples were used in this study. High purity samples were obtained by different methods. On one hand, W and Ta high purity single crystals (99.999%) were grown via the Czochralski method by the Max Planck Institute for Intelligent Systems in Stuttgart. Both samples were cut by electron discharge machining so as to obtain cylinder-shaped samples with surface normals parallel to the [100] crystallographic direction for the W sample, and to [111] for the Ta sample. The orientations of the single crystals were determined by electron backscatter diffraction (EBSD, EDAX, New Jersey, USA). On the other hand, a β-CuZn and a NiAl polycrystalline sample with a composition of 56 wt% Cu and 47 wt% Zn and 69 wt% Ni and 31 wt% Al, respectively, were produced by melting high purity elements (99.99%) in a furnace. The samples were subsequently annealed in an argon atmosphere at different temperature and time conditions followed by furnace cooling to room temperature (work performed at INM).

The bulk materials were prepared by using standard metallographic methods, so that the samples could be glued on SEM specimen mounts. Bulk samples were carefully cut by using a diamond wire saw (Walter Ebner GmbH, Germany). They were then hand ground with silicon carbide particles of decreasing grit size down to 5 µm using a custom-made stainless steel cylindrical holder that was employed to produce parallel-sided samples. Subsequently, the samples were electropolished to reduce the damage produced by the harsh cutting and grinding procedures, and to obtain a flat surface needed for the later microcompression experiments. The electropolishing conditions used for each of the samples are summarized in the following table (Table 3.1).

Table 3.1: Electropolishing conditions of the different samples.

Sample	**Parameter**	
W	Solution	97% distilled water and 3% NaOH
	Voltage	20 V
	Time	40 sec
Ta	Solution	95% CH_3OH and 5% H_2SO_4
	Voltage	34 V
	Time	30 s
β-CuZn	Solution	60 wt% H_3PO_4 and distilled water
	Voltage	1.5 V
	Time	4 min
NiAl	Solution	Struers electrolyte A2-I and A2-II (C_2H_6O, $C_6H_{14}O_2$, $HClO_4$, H_2O)
	Voltage	33 V
	Time	90 s

The W and Ta samples were mounted onto SEM stubs using silver-based electrically and thermally conductive paste (Pyro-Duct 597-A, Aremco Products, New York, NY), which is suitable for elevated-temperature usage. The bonded arrangement was then cured at 70 °C and degassed in vacuum in a furnace (Gero Hochtemperaturöfen, Neuhausen, Germany) to avoid additional hydrocarbon contamination of the SEM used to carry out further *in situ* compression tests at high temperatures. The β-CuZn and NiAl samples were glued onto an aluminum holder using conventional silver paste (Acheson Henkel Silver DAG 1415, Germany), which is widely used for electron microscopy purposes.

3.1.2 Micropillar preparation

Small compression pillars were machined via focused ion beam (FIB) milling into the surface of the bulk materials. This technique was used because it allows extreme control over both the location and the size of the sample [4,128].

In this study, an FEI Versa 3D DualBeam (Hillsboro, OR) microscope with a liquid gallium source was used. This system combines an SEM and an FIB, which enables the reduction of gallium ion exposure experienced by the sample significantly. This was reduced if the FIB was used for structuring only, while imaging was mainly performed with the SEM. The pillar milling procedure was carried out in two steps as shown by Volkert and Lilleodden [87]. First, coarse pillars were milled by using circular stock milling patterns (see Figure 3.1a). Circular craters of 30 µm diameter were machined with a rough shaped pillar at the center. This first step was necessary to assure that the surroundings of the pillars were not compressed during testing. It was performed at a beam voltage of 30 kV and beam currents ranging from 3 to 30 nA depending on the material and size of the pillars to be manufactured. Afterwards, a second milling procedure, which consisted of multiple steps, was carried out at very low currents, between 10 and 100 pA (see Figure 3.1b). This step was carried out in order to reduce the gallium ion damage of the pillars and adjust the final size of the pillars to aspect ratios ranging from 1.5:1 to 5:1 (height:diameter). The diameters of the machined pillars ranged from 200 nm to 5 µm. Also, square-cross-section pillars made of β-CuZn were milled in a similar way. The specimens were machined with crystallographically defined side faces in order to better identify the slip systems activated during compression. The pillar milling approach produced no perfect pillars, but pillars with the shape of a truncated cone or pyramid, i.e., pillar taper shape. However, the relatively lower ion exposure compared to other FIB micropillar milling techniques reduced ion damage [147].

A detailed description of the dimensions as well as crystallographic orientations of the microspecimens can be found in their respective research chapters (sections 4.2, 5.2 and 6.2).

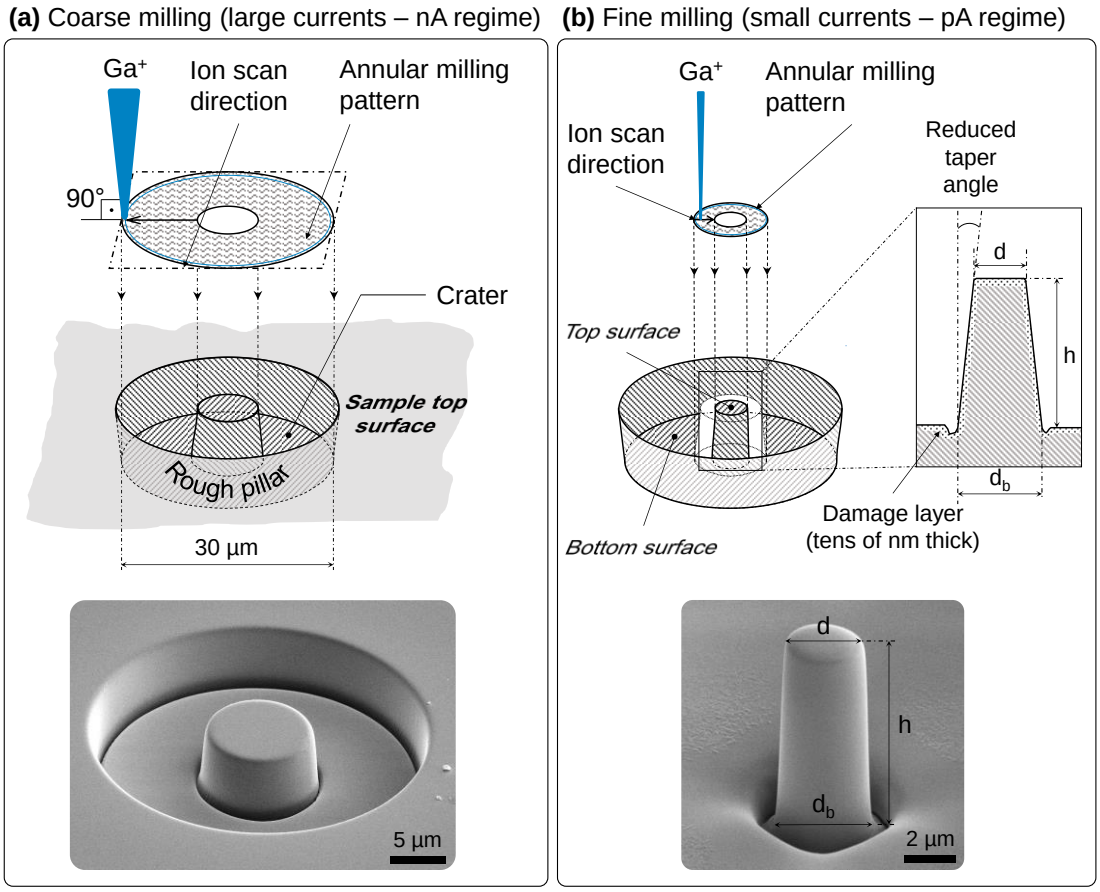

Figure 3.1: Schematic illustration of the FIB-milling procedure used: (a) Coarse milling of a pillar using a circular stock pattern of 30 µm in diameter, and (b) fine milling of the pillar in order to reduce damage layer and taper angle as well as to adjust pillar size. The incident gallium ion beam was kept perpendicular to the sample surface. SEM images taken at 52° tilt of a FIB machined [001]-oriented W micropillar are also shown. The diameter *d* measured at the top of the pillar, the diameter d_b measured at the base of the pillar, and the pillar height *h* were employed to determine the engineering stress-strain data.

3.2 Micromechanical characterization: compression testing

In this work, all micropillars were tested in uniaxial compression in vacuum, at pressures between 10^{-6} and 10^{-5} mbar, hence minimizing oxidation of the samples. Two different nanomechanical systems were employed, which are presented below. High-temperature tests were run with an Alemnis *in situ* indenter (Thun, Switzerland) modified to work at elevated temperatures inside a Zeiss DSM 962 SEM (Jena, Germany). Such tests were performed at the Laboratory of Mechanics of Materials and Nanostructures, headed by Dr. Johann Michler, at Empa - Swiss Federal Laboratories for Materials Science and Technology, Switzerland. On the other hand, room-temperature measurements were

carried out with our in-house Hysitron PI 87 SEM PicoIndenter (Minneapolis, MN) inside the same system used to fabricate the micropillars, i.e., the FEI Versa 3D DualBeam.

Before testing, the sizes of the different micropillars were measured from SEM images (FEI Versa 3D DualBeam) since the length and diameter of the pillars are needed to convert the load-displacement data into stress-strain data. Engineering stresses were calculated considering the diameter at the top of the pillar *d* (see Figure 3.1b). True stress and true strain were not estimated since the deformation mostly occurred heterogeneously by slip of few systems. The top diameter was preferred since it is well defined and easy to measure through SEM imaging. In addition, the stress is highest at the top due to the tapered pillar shape. The distance between the approximated intersections of the tapered pillar with the base material and the pillar top (see Figure 3.1b) was defined as the height of the pillar *h*. Thus, the engineering stress σ and engineering strain ε were calculated using the following:

$$\sigma = \frac{4 \cdot F}{\pi \cdot d^2} \qquad \text{Equation 3.1}$$

and

$$\varepsilon = \frac{\Delta x}{h} \qquad \text{Equation 3.2}$$

where F is the load and Δx is the displacement of the pillar top.

To accurately determine the specific stress/strain rate of the micropillars and Δx [87,148], corrections of the compliance of the frame and the sample were required. For that, Sneddon's solution [87,148] was used. Assuming that the pillars and the substrate have the same properties, the displacement Δx of the pillar top can be written as:

$$\Delta x = \Delta x_{meas} - \frac{1-\nu_i^2}{E_i}\left(\frac{F_{meas}}{d}\right) - \frac{1-\nu_s^2}{E_s}\left(\frac{F_{meas}}{d_b}\right) \qquad \text{Equation 3.3}$$

where Δx_{meas} is the measured displacement and F_{meas} is the measured force. E_s and ν_s are Young's modulus and Poisson's ratio of the tested material, while E_i and ν_i are Young's modulus and Poisson's ratio of the indenter, respectively. The pillar diameter at the top is d, while the diameter at the bottom is d_b.

To conduct the elevated-temperature compression tests, a calibration of the different sample-tip temperature was also required since minimizing thermal drift is crucial for measuring reliable strain values. This was performed as indicated by Wheeler and Michler [149]. The indenter and sample heaters were set to heat to the desired test temperature so

as to reduce the drift produced during testing. After an initial stabilization period at the target temperature of approximately 10 min, prior to full system stabilization, the indenter was switched to constant heating power to perform temperature tuning indentations to match the indenter and sample surface temperatures. Since this temperature matching process was accomplished using temperature measurements instead of displacement drift measurements, the temperatures could be accurately matched while the thermal gradients within the system frame were still stabilizing. This was significantly more time efficient than displacement drift measurements, which would require the frame to be completely stable before a direct relationship between drift and indenter/sample temperature mismatch would be expected. The tuning procedure involved indentations at 4 or 5 different indenter/sample temperatures and lasted approximately 1 h. A default displacement rate of 20 nm/s was used during displacement control approach and retraction. If the initial target for the indenter was correct, this temperature shift profile measured no significant variation during contact. If the temperature was observed to change, the indenter temperature was adjusted in the opposite direction of the shift. This procedure was repeated until the indenter temperature matched the sample surface temperature.

3.2.1 Elevated-temperature in situ SEM indenter

The elevated-temperature mechanical testing platform employed consists of an *in situ* SEM Alemnis indenter heavily modified (by Empa) to provide it with heating as well as with active and passive cooling mechanisms. On one hand, tip and sample heating are integrated and controlled by using independent thermocouples. On the other hand, the frame of the system is made of highly thermal conductive alloys and is water-cooled, thus containing heat and protecting sensitive components from overheating. Furthermore, the load cell is kept from excessive heat by providing a low thermal resistance shortcut for heat coming from the sample.

The system is intrinsically displacement-controlled, that is, a certain displacement rate is imposed via a piezoelectric actuator placed behind the tip, and force is then recorded with a capacitive transducer positioned behind the sample holder. The piezoelectric actuator has a displacement range of 20 µm, and the load cell has a maximum force of 500 mN and an instrumental noise level of 15 µN. A sketch of the system is presented in Figure 3.2. For more detailed information of the system, see reference [149].

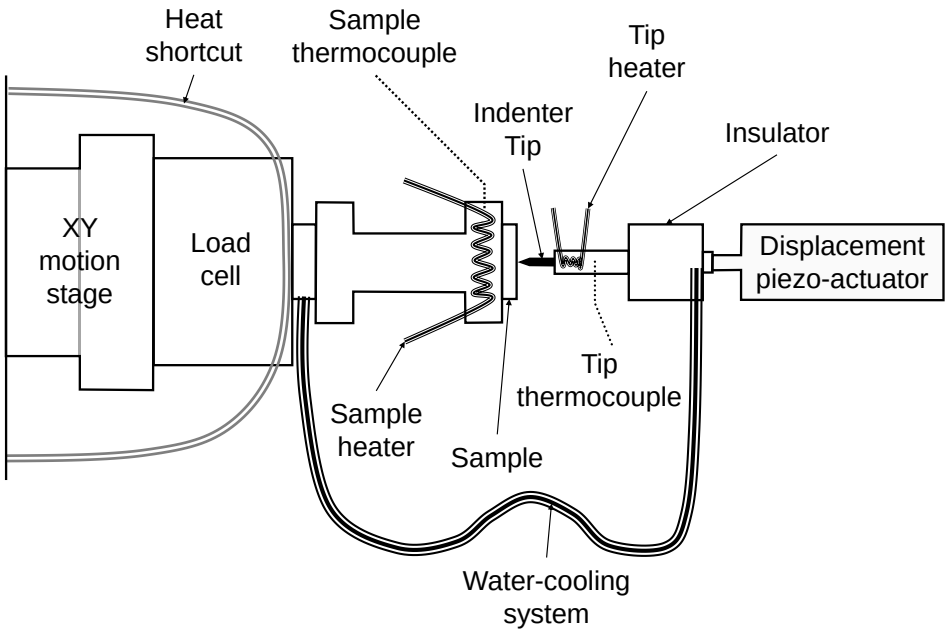

Figure 3.2: Illustration of the elevated-temperature *in situ* SEM nanomechanical system used, adapted from reference [149]. The independent sample-tip heaters and passive/active cooling set-up allow for accurate control of temperature and minimization of thermal drifts. The instrumental noise level of approximately 15 µN hinders compression of sub-micropillars at elevated temperatures.

3.2.2 Room-temperature in situ SEM indenter

Room-temperature compression tests were carried out using a Hysitron PI 87 SEM PicoIndenter equipped with a conductive diamond flat punch of approximately 9 µm wide. This nanomechanical platform includes a set of piezoelectric actuators that provides 5 degrees of freedom: x, y, z movement as well as tilt and rotation. This allows for accurately positioning the sample and reducing, to a great extent, contact misalignments between tip and sample.

In contrast to the elevated-temperature *in situ* SEM Alemnis indenter, this system is inherently load/displacement controlled, which allows us to perform tests in either load or displacement control. A three-plate capacitive sensor provides a force electrostatically and displacement is measured capacitively. Such a device is highly sensitive. It ensures very low load instrumental noise levels, of the order of 0.2 µN and 1 nm, respectively. However, it is limited to a maximum load of 30 mN and a maximum compression displacement of 5 µm. A sketch of the system is presented in Figure 3.3.

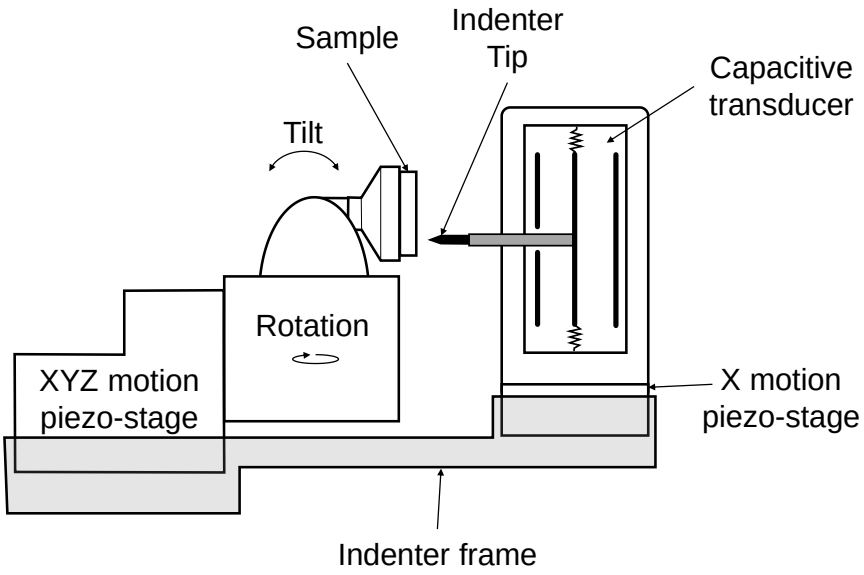

Figure 3.3: Illustration of the room-temperature *in situ* SEM nanomechanical system used. This system has 5 degrees of freedom via different sub-nanometer resolution piezo-actuators; thus accurate positioning of the sample is achieved. A three-plate capacitive transducer allows for high resolution force sensing (well below 1 µN), remarkably suitable for testing micropillars.

3.3 Microstructure characterization

To gain further insight into the deformation mechanisms of compressed micropillars, EBSD and transmission electron microscopy (TEM) were employed on several compressed micropillars. For this, lamellae were cut out of different 2 µm diameter micropillars. These lamellae were fabricated using the same system used to prepare the pillars, the FEI Versa 3D DualBeam, as well as an argon ion polishing machine Nanomill - Fischione Instruments (Export, PA). The procedure followed was the so-called 'lift-out method with internal grid mounting'. For EBSD purposes, lamellae of approximately 1 µm in thickness were produced whereas lamellae of about 100 nm thick were prepared for TEM imaging. The fabrication procedure is shown in Figure 3.4 and was as follows.

First of all, a platinum (Pt) layer was deposited on top of the pillars to protect it from being FIB damaged and sputtered away during subsequent milling steps (Figure 3.4b). This process consisted of two steps. A thin Pt layer of approximately 100 nm thick was deposited via electron beam induced deposition (EBID), a local assisted chemical vapor deposition (CVD) technique. This was meant to protect the pillar from the subsequent step, which consisted of depositing a thicker Pt layer of about 1 µm wide and 2 µm thick by using the ion beam induced deposition (IBID) technique instead. The IBID process

was used to save time as the EBID requires longer periods to deposit the same amount of Pt.

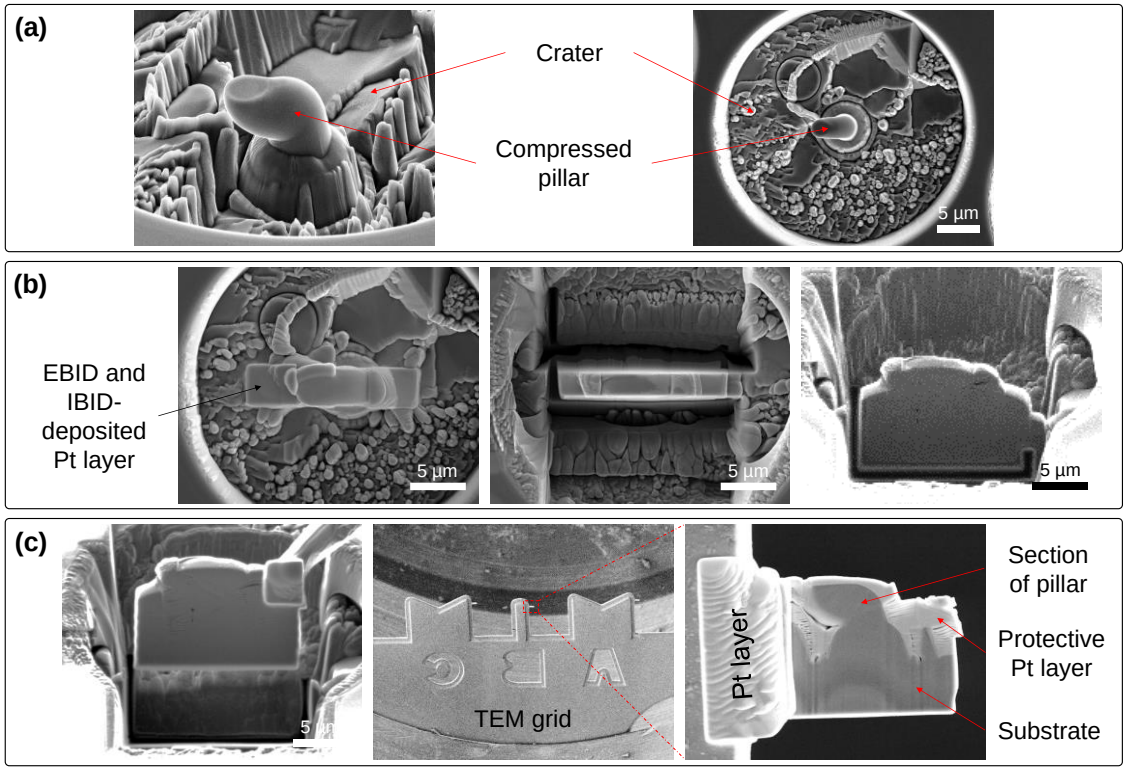

Figure 3.4: Preparation procedure used for producing thick and thin lamellae of micropillars for further EBSD and TEM analysis. (a) SEM images of a compressed [001]-oriented NiAl pillar. (b) Deposition of Pt layer on top of pillar, cutting of 2 trenches (one on each side of the pillar) and further cut-off procedure to free the thick lamella from the substrate. (c) Attachment of the lamella to a manipulator via Pt-IBID, transfer of the lamella to a TEM grid, and final thinning of the lamella using the FIB.

Second, a high gallium ion beam current of 3 nA was used to mill large amounts of material away from the front and back portion of the region of interest (Figure 3.4b). Two trenches of about 20 µm long, 7 µm wide and 12 µm deep were milled on both sides of the Pt layer. Both trenches were created using stair-case step milling patterns, which remove less material but enough to observe the cut from a 52° angle via SEM imaging. A thick lamella of approximately 1 µm thick was left.

Third, a micro-manipulator pluck-out needle was used to transfer the thick lamellae onto a Cu TEM grid (Figure 3.4c). The micro-manipulator was glued at one edge of the thick lamella using the Pt assisted CVD. Then, the lamella was plucked from the substrate by milling small trenches at both edges and bottom of the lamella. Once free, the lamella was placed on a TEM grid by gluing it through the Pt assisted CVD process, and plucking the micro-manipulator via FIB milling.

Last, the thick lamellae, meant for EBSD imaging, were slightly thinned at lower voltages and currents (5-8 kV and 49-77 pA), and subsequently polished with the argon polishing machine at 900 V and 112 µA. This last step was carried out to reduce the damage produced by the gallium ion beam. For TEM imaging, thinner lamellae were required, so that lamellae were thinned down to a thickness of approximately 100 nm. This was performed by gallium ion milling the lamellae at an incident angle of 2° at low beam currents (49 – 77 pA) and low voltages (5 – 8 kV), and by further argon ion polishing at the same beam conditions used as for the thick lamellae.

3.4 Scanning electron microscopy / Electron backscatter diffraction

The fact that all tests were conducted inside SEMs allowed for secondary electron imaging of the microspecimens while monitoring the force and displacement of the tests. Furthermore, all pillars were secondary electron imaged using the SEM capabilities of the FEI Versa 3D DualBeam before, during and after testing. The DualBeam was also used to find the orientations of the crystals of the different materials as well as to analyze the local misorientations of compressed pillars (thick lamellae) by using the EBSD technique.

In summary, an electron beam, produced with a field emission source, is accelerated and focused on the sample with magnetic lenses. The electrons impacting the sample either are scattered on the surface or emit secondary electrons and characteristic X-rays. The sample is usually raster scanned, so that the electrons are detected to create images. Furthermore, by using an EBSD detector by EDAX (New Jersey, USA), the Kikuchi patterns originated from the diffraction of backscattered electrons can be detected, so that microtexture information is also accessible.

3.5 Transmission electron microscopy

Transmission electron microscopy (TEM) was used to observe the deformation mechanisms that had taken place in compressed micropillars. For imaging, a JEOL JEM-

2100 LaB6 (Tokyo, Japan) microscope was employed at an accelerating voltage of 200 kV under bright-field imaging.

The bright-field imaging technique is based on the interactions of highly energetic electrons with matter. When electrons are projected to a sample, the degree of absorption or diffraction of electrons varies within the different regions of the sample. The electrons that are transmitted through the sample are collected from below the sample on a phosphorescent screen or via a camera. In the areas where electrons are scattered or absorbed, the image is dark whereas in the regions where electrons are transmitted, the illustration is brighter. There is a spectrum of greys depending on the way the electrons are scattered and interact with the microspecimens studied.

3.6 Experimental constraints

Both the preparation of microspecimens via FIB machining and the micropillar compression approach exhibit several drawbacks that are subject of controversy. To understand, in this case, how BCC and B2 metals deform at the (sub-) microscale, such experimental uncertainties must be borne in mind.

First, the bombardment of specimens with highly accelerated gallium ions may affect the mechanical properties of the actual micropillars [150]. An affected layer is produced at the free surface of the micropillars [5,150]. This is characterized by an amorphous layer, which typically contains defects such as point defects, dislocations and precipitates [84,85,150]. Such an amorphous layer may range in thickness from a few nanometers to tens of nanometers as shown by different TEM studies [84,85] and ion-matter interaction simulations [151–153]. The existence of these defects and the thickness of the affected layer depend on material properties such as atomic weight and interatomic bonding, as well as on energy and impact angle of the ions [150,154,155]. It has been shown that pillars of the order of micrometers (Cu) are barely affected by the damaged layer [150]. For pillars on the nanometer scale, however, the influence of the damaged layer on strengthening of samples may become significant [82,150]. The defects introduced by FIB milling may work as dislocation sources [156], which may influence the strengthening effect on the samples. Nevertheless, *in situ* TEM compression of Ni nanopillars has shown that the amorphous layer does not prevent dislocations from escaping the micropillars [82], thus suggesting that the amorphous layer may not confine

deformation. The ion currents used in this work were of the order of previous studies. Furthermore, the interatomic bonding of the refractory BCC metals (Ta and W) as well as of B2 alloys (β-CuZn and NiAl) employed are rather stable compared to other metals given their low homologous temperatures. Therefore, it is expected that the effect of ion irradiation may be comparable to other studies on FCC and BCC metals.

Other disadvantages come from the actual FIB milling technique used, in which a normal incident gallium ion beam is directed to the sample surface, and hence, tapered pillars with typical angles from 2° to 5° [5] are produced. This irregular pillar shape leads to inhomogeneous deformation along the compression axis, errors in the engineering stress and strain curves, overestimated elastic modulus, false strain hardening and increased apparent yield stresses caused by the irregular applied stress field within the micropillar [82,157]. In that respect, the 'ion-lathe' technique, introduced by Uchic and Dimiduk [128], could be used to obtain micropillars without taper. However, this method is very time consuming and exposes the samples to significantly more ion irradiation [147]. As a result, this potentially increases the thickness of the damage layer. Moreover, it becomes rather difficult to machine pillars smaller than 1 µm diameter [5]. Because of these reasons, the two-step milling method [87] was employed in this work instead. In addition, the fact that the pillar tapering contributes to the heterogeneity of the micropillar stress state prevents the comparison of specimens of different size and taper angle [130,157]. Therefore, effort was made to produce microspecimens with low taper angles, similar to previous studies [6,7]. Care was taken to keep the taper angle relatively constant for pillars with different crystallographic orientation, thus allowing for direct comparison among pillars of different orientations.

There are three main aspects of testing that need to be addressed in order to perform tests with as few artifacts as possible. One is the presence of dirt on the sample and/or tip surfaces, which may affect the uniform loading of the pillar and the measurement of the pillar displacement [5]. To reduce such effects, the tips were cleaned with ethanol before testing, and the samples were stored in cases. Another issue, which may become critical, is the alignment between the micropillar and the flat punch [5]. Misalignments greater than 1° lead to the underestimation of the yield point and elastic modulus, to changes in the strain-hardening response, and to buckling [157,158]. Consequently, all tests were carried out *in situ* in the SEM, so that the indenter could be placed as precisely as possible onto the pillar surface, and pillars were visualized to verify that no bending/buckling occurred during testing. Furthermore, for room-temperature tests, a thin platinum stripe

was deposited by means of IBID on the bulk sample surface, relatively close to the micropillars. This stripe provides a soft surface on which indentations were performed. This allowed for additional adjustments on the tilting/rotation angle and thus for reductions in contact misalignments. Also, it has been observed through microcompression experiments and finite element simulations of isotropic and anisotropic materials [157,159–161] that the lateral stiffness of indenter and friction between the indenter tip and the pillar surface contribute considerably to the deformation behavior of the microspecimens. Assuming pillars with tapered angles perfectly aligned with respect to the indenter tip, friction has shown to slightly influence the load-displacement response [160]. However, the deformation shape is relatively different in the presence or absence of friction. Plastic instabilities occur more readily in the absence of friction and/or with the use of cylindrical pillars (no taper) and pillars with large aspect ratios (length:diameter). Particularly, it has been observed that stress-strain curves are not affected strongly if the specimens possess aspect ratios of 2-3, at relatively low strain levels (<5%) [160]. Therefore, to reduce plastic instabilities and influence as less as possible the mechanical response of the samples, in the current study, mostly pillars with an aspect ratio of approximately 3 and with a slight taper were employed.

Last, one of the cornerstones for obtaining reliable elevated-temperature load-displacement data is the minimization of thermal drift and noise since this may be the main cause of errors in strain measurement. Temperature fluctuations of the order of 1 K within the sample-indenter system can cause thermal expansions of several nanometers [149], which can be crucial for microcompression testing. Therefore, thermal stability of the indenter-sample system is required, requiring stable thermal gradients. To address this, an elevated-temperature indenter with accurate control of tip and sample heating as well as equipped with water-cooling and insulation was used (see section 3.2.1).

Other concerns related to compression testing, such as the compliance of the testing system and the constraint of the pillar by the underlying material and substrate, were discussed above in this section (3.2).

4 Temperature-dependent size effects on the strength of Ta and W micropillars

The strength of metals increases with decreasing sample size, a trend known as the size effect. In particular, focused ion beam-milled BCC micropillars exhibit a size effect known to scale with the ratio of the test temperature to the critical temperature (T_c) of the BCC metal, a measure of how much the yield stress is governed by the lattice resistance. In this work, this effect is systematically studied by performing high-temperature compression tests on focused ion beam-manufactured Ta and W single crystal pillars ranging in diameter from 500 nm to 5 µm at temperatures up to 400 °C, and discussed in the context of bulk strength and size dependent stresses. Both metals show larger size effects at higher temperatures, reaching values that are in the range of FCC metals at temperatures near T_c. However, it is demonstrated that size effects can be considerably affected by material parameters such as dislocation density and lattice friction, as well as by the yield criterion used. Furthermore, for W, a change from uniform wavy deformation to localized deformation is observed with increasing temperature and pillar size, further indicating that the temperature ratio strongly influences the relative motion of screw and edge dislocations.

Chapter published by O. Torrents Abad, J. M. Wheeler, J. Michler, A. S. Schneider and E. Arzt in Acta Materialia 103, 483–494 (2016).

O.T.A. co-designed the project, prepared the samples, produced the micropillars as well as performed experiments, material characterization and analysis of the data. Also, O.T.A. interpretated the data and wrote the manuscript. A.S.S. and E.A. co-designed, supervised the project and contributed to the writing of the final paper. J.M.W. performed experiments and analyzed data. All authors read and commented on the manuscript.

4.1 Introduction

The mechanical properties of sub-micron and micron-sized structures differ from those of bulk material. When the dimensions of a sample are similar to or smaller than the microstructural length scales, interfaces and free surfaces become important. In particular, such 'size effects' have been observed for metals, where the strength usually increases with decreasing sample size. The 'dimensional constraint' on dislocation processes then overrides the 'microstructural constraints' that usually dictate the strength in bulk metals [1], or 'external size effects' dominate over 'internal effects' [104]. Researchers have described such size effects by relating mechanical properties and a geometrical or microstructural size scale of interest as follows:

$$\sigma_y = \sigma_0 + kd^n, \qquad \text{Equation 4.1}$$

where σ_y is the yield strength of the structure, σ_0 is the bulk strength of the material, d is the characteristic length scale, and k and n are constants. For example, the Hall-Petch relationship predicts a power-law exponent n of -0.5 for metallic materials in which d is the grain size [122,123]. Thin film tests and compression tests on micropillars have shown typical values for n in the order of -0.5 to -1, where d is the film thickness or pillar diameter. When strain gradients are present, size effects can emerge naturally ('strain gradient plasticity') [162–164], an effect that is ruled out for micropillar compression testing.

Micropillar compression studies have mostly focused on metals with the face-centered cubic (FCC) crystal structure (Ni [4,82–84], Au [85–90], Cu [91,92] and Al [93]) and the body-centered cubic (BCC) crystal structure (W [7,8,97,132], Mo [6–8,88,89,94–97], Nb [7,97–99,132], V [100] and Ta [7,101]). These experiments have reported that, for pillars with diameters ranging from 200 nm to a few micrometers, an inverse power-law relation between yield strength and sample size is observed. For FCC metals, in which the bulk strength, σ_0, is usually negligible, the power-law exponent, n, lies in the range of -0.6 to -1.0 [5,83,84,86,87,91,93,104,128–130]. On the contrary, BCC metals have shown a weaker size dependence than FCC metals; their behavior was found to correlate with their critical temperature that signifies the transition from a strong to a weak temperature dependence of the flow stress in BCC metals [7]. The different degrees of size dependence have been attributed to different contributions of the lattice resistance to plastic strength

of each particular BCC metal (which is dependent on the Peierls potential of the metal and is independent of size) [7,88]. Unlike in FCC metals, screw dislocations in BCC metals have a rather complex non-planar core structure with a threefold symmetry [26]. Consequently, BCC metals present high Peierls potentials that lead to low mobility of the screw dislocations in comparison to edge dislocations [165]. As the ratio of the test temperature to the critical temperature (T_c) was found to correlate with the magnitude of the size dependence, it was proposed that the decreasing size dependence in BCC micropillars reflects the decreasing mobility of the screw dislocations [7,8]. However, size effects in BCC metals have been typically determined without considering the contribution of bulk stresses, σ_0, which are often in the order of hundreds of MPa for BCC metals at room temperature and should not be neglected [101,138,144,145].

Different studies have tried to understand the role of bulk stresses, more precisely the role of the lattice resistance on the size effect of micropillars [8,138,142]. Lee and Nix [142] have carefully compared the power-law exponents of FIB machined FCC and BCC micropillars by considering different material parameters. Material parameters such as lattice friction, dislocation density, shear modulus and Burgers vector, which are size independent but can depend on temperature, affect the size dependence in sub-micron and micron-sized pillars [8,142,166–168]. Lee and Nix suggested that the main argument for the different power-law exponents is the value of lattice friction, and this was rationalized in terms of the single-arm dislocation source model first proposed by Parthasarathy *et al.* [113]. At a moderate dislocation density (10^{12} - 10^{13} m $^{-2}$), the strength of micropillars with diameters of a few micrometers was assumed to be controlled by the operation of single-arm dislocation sources, which are Frank-Read sources truncated at the free surface [142,168]. Through this model, the critical resolved shear stress of a pillar with a diameter of a few micrometers can be calculated as the linear superposition of the lattice resistance in shear, τ_0, a work-hardening term containing the total dislocation density, ρ_{tot}, and a size-dependent term:

$$\tau_{CRSS} = \tau_0 + 0.5\mu b\sqrt{\rho_{tot}} + \frac{\alpha\mu b}{\bar{\lambda}_{max}(d,\rho_{tot},\beta)} \cong \tau_{bulk} + \tau_{size\ dependent}, \qquad \text{Equation 4.2}$$

with the shear modulus μ, the Burgers vector b, the line tension of the weakest single-arm dislocation source determined by the statistical average length of the weakest source $\bar{\lambda}_{max}$, and a geometrical constant of order of unity α [113]. The dependence of the power-law exponent on lattice friction has been recently demonstrated by Soler *et al.* [146]. Chemically etched LiF micropillars, with a controlled initial dislocation density, were

tested at different temperatures and rigorously analyzed by using Parthasarathy's model. The authors concluded that size effects are the result of the relative contributions of bulk stresses and size-dependent stresses. It was shown that at room temperature, bulk stresses dominated the absence of size effect, while at 250 °C, both contributions were of the same order, thus giving rise to a large size effect.

To improve the understanding of the size effect in BCC metals, tests conducted at different relative temperatures (compared to the critical temperature) are required. So far, only two studies have varied this parameter in BCC metal pillars [8,132]. Schneider *et al.* [8] have shown that Mo micropillars tested at 500 K (above T_c for this materials) exhibit a size dependence very close to that of FCC metals, suggesting that the better mobility of screw dislocations above T_c allowed Mo micropillars to deform as FCC micropillars. As a result, it was suggested that the dislocation process controlling the size dependence in BCC micropillars may be the same as in FCC micropillars: source truncation [113], mechanical annealing [82] and/or dislocation starvation [90]. On the other hand, Lee *et al.* [132] have recently studied the size dependence of Nb and W nanopillars at 165 K (far below T_c for these materials), and also assessed the stochastic nature of nanopillar deformation together with dislocation dynamics simulations. It was suggested that the surface-controlled dislocation multiplication is restricted when the mobility of screw dislocations is similar to that of edge dislocations, thus resulting in smaller plastic strain bursts at temperatures close to T_c or above. What is lacking so far, however, is a study in which the test temperature is varied systematically.

The aim of the present paper was to investigate the plasticity of BCC pillar structures at the micron and sub-micron regimes, for the first time, at different temperatures up to 400 ºC. Emphasis was placed on Ta and W micropillars. The implications of lattice resistance and dislocation density as well as straining are discussed in the context of size effect dependence on temperature.

4.2 Experimental method

High purity Ta and W single crystals (99.999%) with dimensions of approximately 5 mm x 5 mm x 1 mm were used for this study. The Ta crystal had a [111] and the W crystal a [100] orientation. These orientations were selected to have the same orientations as in previous room temperature studies [7,101]. In addition, two multiple slip orientations

were selected to study the influence of orientation on the temperature dependent size effect of BCC metals. The samples were ground with silicon carbide papers down to a grit size of 4000 using a stainless steel cylindrical holder that was employed to produce parallel-sided samples. Subsequently, they were electropolished to reduce the grinding damage and to obtain a flat surface needed for the subsequent microcompression testing. 72 micropillars per sample were FIB manufactured with an FEI Versa 3D DualBeam equipped with a gallium ion source. The pillar milling procedure was carried out in two steps as described by Volkert and Lilleodden [87]: The first step was performed at a beam voltage of 30 kV and beam currents of 7 and 13 nA depending on the pillar dimensions. A second milling procedure, which consisted of multiple steps, was carried out at very low currents, between 10 and 100 pA, to reduce the ion damage and adjust the final pillar shape. The pillars, ranging from 500 nm to 5 µm in diameter with an aspect ratio (length/diameter) of approximately 3, had a taper angle of 2.5 ± 0.4 ° for the Ta sample and 2.2 ± 0.3 ° for the W sample.

Compression of the pillars was performed at different temperatures up to 400 ºC using an Alemnis indenter at Empa, modified to run at high temperatures inside a Zeiss DSM 962 scanning electron microscope (SEM) [149,169] at a chamber pressure of about $5 \cdot 10^{-5}$ mbar. The indenter was equipped with a diamond flat punch of approximately 9 µm in diameter. The fact that the tests were performed inside the SEM minimized oxidation of the samples at high temperature. The system had two independent thermocouples, one on the indenter tip and another on the sample, such that temperature was accurately controlled. Two different calibrations were made prior to testing: a calibration of the sample-tip temperature difference and a calibration of the compliance of the whole indenter-sample system as described previously by Wheeler and Michler [149]. First, the indenter and sample heaters were set to heat to the desired test temperature to reduce the drift produced during testing. Second, a small correction for the compliance of the load frame, as well as another one for the sink-in compliance of the pillars, which rest on the same substrate material, were applied for each test to precisely determine the specific load rate and strain of the micropillars. The effect of the pillar acting as a flat punch and elastically deforming the substrate during compression as well as the effect of the indenter itself elastically deforming were considered using the Sneddon's solution [87,148].

The Ta micropillars were tested at 25, 100 and 200 °C. On the other hand, W micropillars were compressed at 25, 200 and 400 °C. The tests were conducted under displacement control at fixed displacement rates. The displacement rates were scaled with the pillar

height in order to obtain a constant strain rate of 10^{-3} s^{-1} for pillars with different heights and a maximum strain of approximately 0.10. The experiments at 25 °C were carried out before those at 100 °C, and the ones at 200 and 400 °C were performed at the end to avoid any possible annealing effect.

To convert the obtained load-displacement data into stress-strain curves, the measured lengths and diameters were used. In view of the tapered pillar shape, the diameter at the top of the pillars was used to determine engineering stress. True stress and true strain were not meant to be determined as the deformation mostly occurred heterogeneously by slip of a few systems. The top diameter was chosen because it is well defined and easy to determine via SEM imaging. Furthermore, the stress is the highest at the top due to the tapered pillar shape. The implications on the determined stress level by choosing an appropriate reference diameter were discussed in detail by Frick *et al.* [84] and Kiener *et al.* [130].

4.3 Results

4.3.1 Plastic deformation morphology

Figure 4.1 shows SEM images of representative compressed Ta and W micropillars as a function of size and test temperature. Irrespective of pillar diameter and test temperature, all Ta micropillars exhibited slip bands reaching the surface of the pillars as previously reported in the literature [7,101]. Although the [111] is a multiple slip orientation, slip occurred mainly for the preferred slip system and the deformation was localized close to the upper end of the pillars. On the other hand, W micropillars showed traces indicative of multiple slip as observed before [7,98,132]. All W pillars compressed at room temperature exhibited a homogeneous, wavy deformation, indicating cross-slip of screw dislocations. This wavy deformation was also exhibited by small pillars (500 nm in diameter) compressed at higher temperatures. However, larger pillars compressed at higher temperatures showed a transition in deformation mechanism from homogeneous to localized deformation (see Figure 4.2). This indicates that a more avalanche dominated behavior caused by the activation of only a few slip systems took place for larger pillars at 200 and 400 °C.

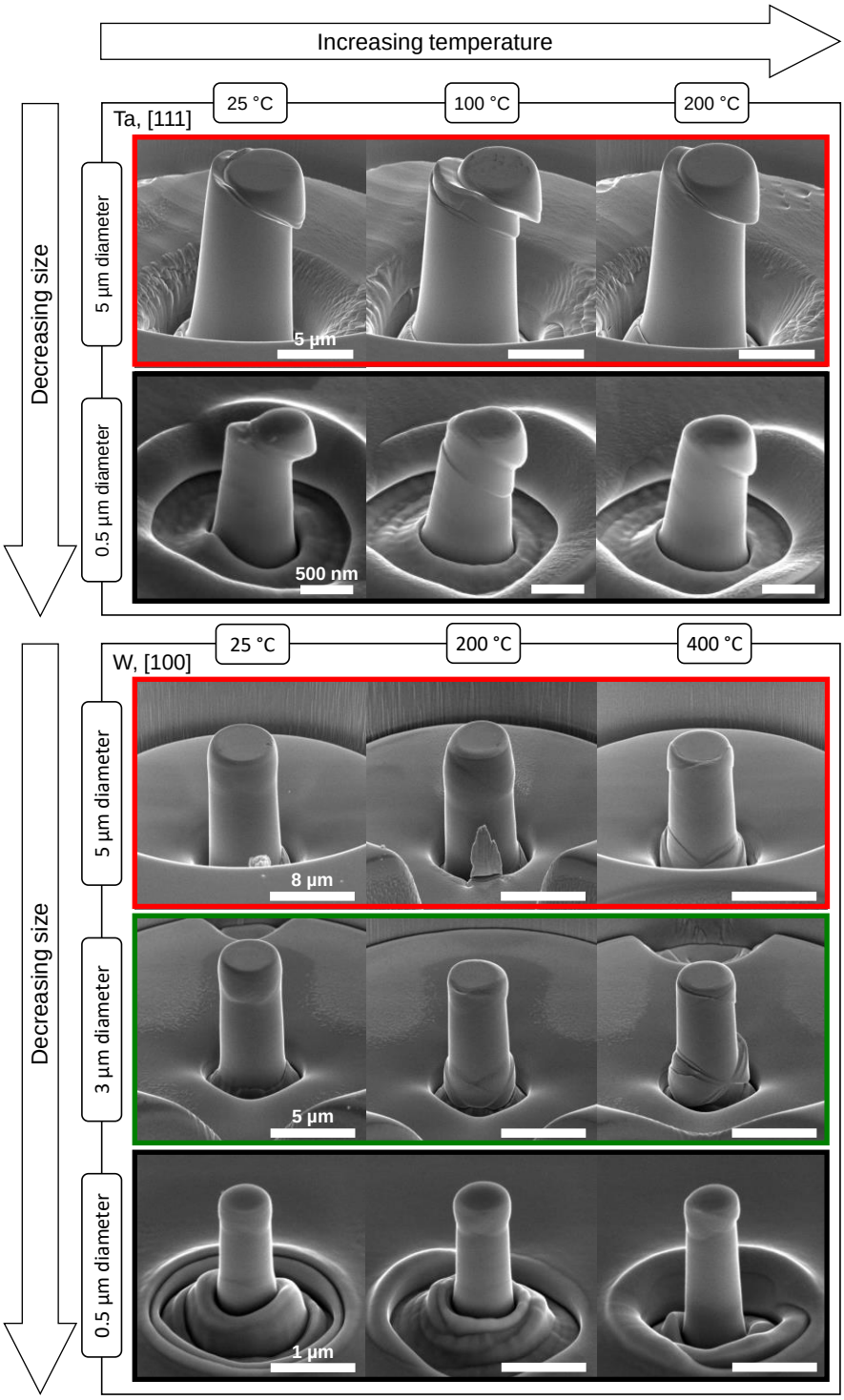

Figure 4.1: Scanning electron microscopy images of representative micropillars after testing: (a) [111]-oriented Ta, with diameters of 5 and 0.5 µm compressed at 25, 100 or 200 °C, and (b) [100]-oriented W, with diameters of 5, 3 and 0.5 µm compressed at 25, 200 or 400 °C.

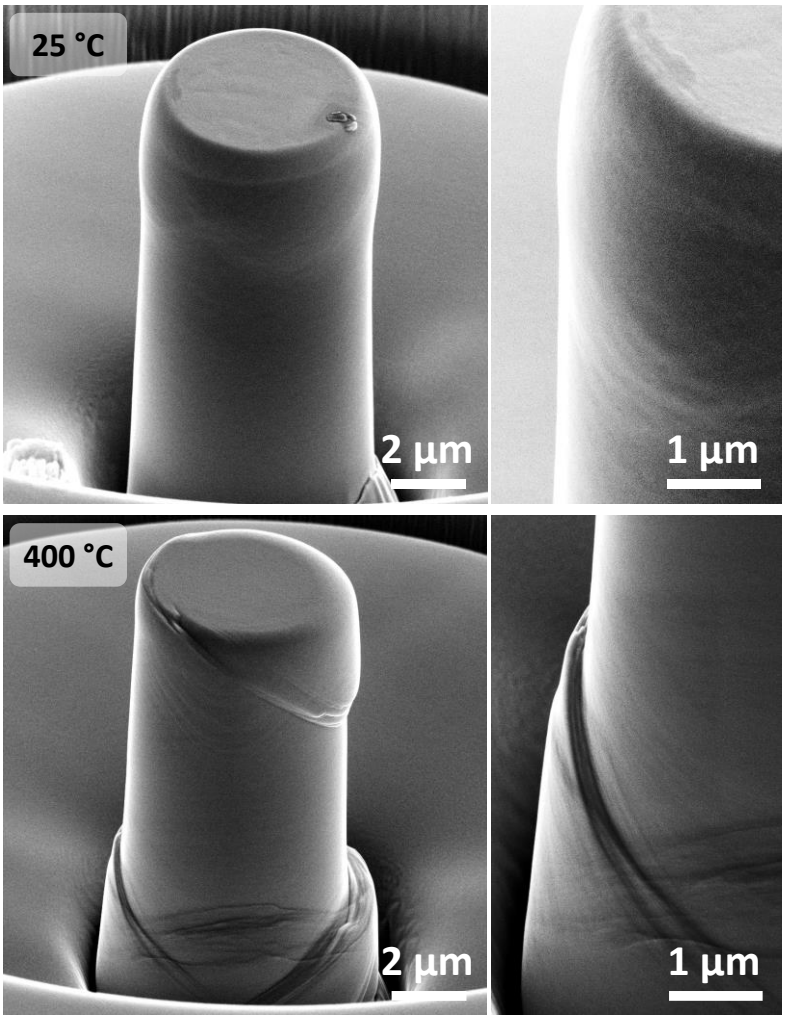

Figure 4.2: Scanning electron microscopy images of two representative [100]-oriented W pillars with a diameter of 5 µm compressed at 25 and 400 °C. High-resolution insets emphasize a change in deformation morphology with increasing test temperature: from homogeneous to localized deformation.

4.3.2 Stress-strain response as a function of pillar size and temperature

Stress-strain curves of representative Ta micropillars compressed at 25, 100 and 200 °C, and W micropillars compressed at 25, 200 and 400 °C are depicted in Figure 4.3 and Figure 4.4, respectively. The distinctive behavior of displacement controlled compression was observed in these curves. Low stiffness artifacts were recorded during first loading as initial contact of the flat punch on pillars took place [87]. Stiffness values then increased and elastic loading started before yield occurred at a critical point. The stress-strain curves of the micropillars with diameters larger than 2 µm were relatively continuous, while, for micropillars between 500 nm and 1 µm diameter, the loading curves showed pronounced stress drops along the whole strain range, indicating that the stress-strain behavior became more stochastic as the diameter of the micropillars decreased. This is in consonance with other experimental studies where such behavior

was attributed to the reduction in the number of available dislocation sources as sample size decreased [93,170]. It is readily apparent that the curves for the 500 nm diameter pillars, and to a smaller extent, those for a diameter of 1 µm, exhibited sizeable stochastic scatter. This may be attributed to the small testing loads: in the extreme case, i.e., for Ta pillars tested at 200 °C, loads as low as 100 µN were required for yielding, relatively close to the instrumental noise level (15 µN). This noise level caused an uncertainty of about 70 MPa in the extreme case (Ta pillars of 500 nm in diameter compressed at 200 °C). Still, the smallest load drops were noticeably above the instrumental noise. Their amplitude increased with increasing test temperature, indicating that larger dislocation avalanche events occurred at higher temperatures. For comparison, Figure 4.3d and Figure 4.4d show representative stress-strain curves of the largest and smallest micropillars for both Ta and W samples compressed at different temperatures. It can be observed that flow stresses scaled with pillar diameter for both Ta and W samples, and above all, that flow stresses were altered greatly by the test temperature. Furthermore, flow stress data converged for small pillars, implying that small pillars were less susceptible to temperature conditions.

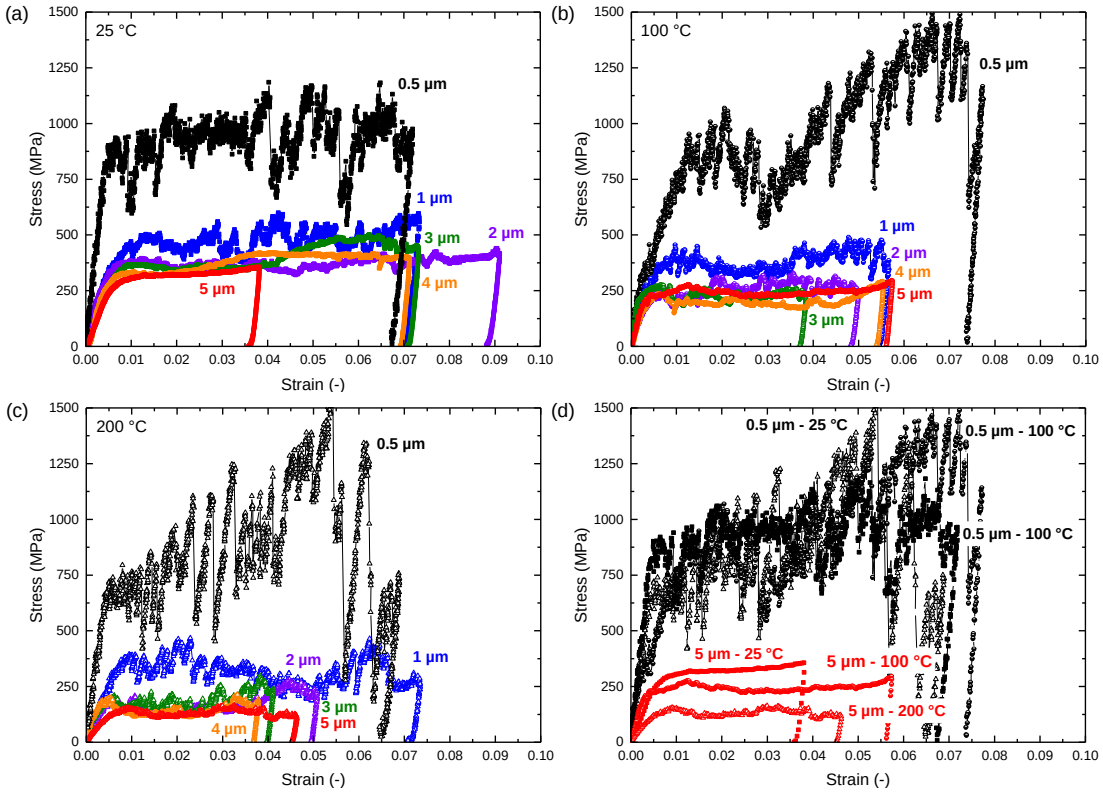

Figure 4.3: Typical compressive stress-strain curves of different Ta micropillars with diameters ranging from 0.5 to 5 µm tested at different temperatures, (a) 25 °C, (b) 100 °C and (c) 200 °C. (d) Comparison of stress-strain curves for micropillars of 0.5 and 5 µm diameter taken from (a), (b) and (c). Squared solid symbols represent micropillar tests performed at 25 °C while triangular open symbols depict tests performed at 200 °C and circular semi-open symbols at 100 °C.

Some W micropillars showed a stress maximum between 1 and 2% total strain, mostly the largest pillars compressed at room temperature (see Figure 4.4a). This peak was followed by stress relaxation at small strains and has been previously attributed to contact misalignment between the flat punch and the top surface of micropillars as well as a slight geometrical tilt of the pillars [171]. This maximum can obscure the estimation of the yield point and subsequent determination of size effects as discussed later.

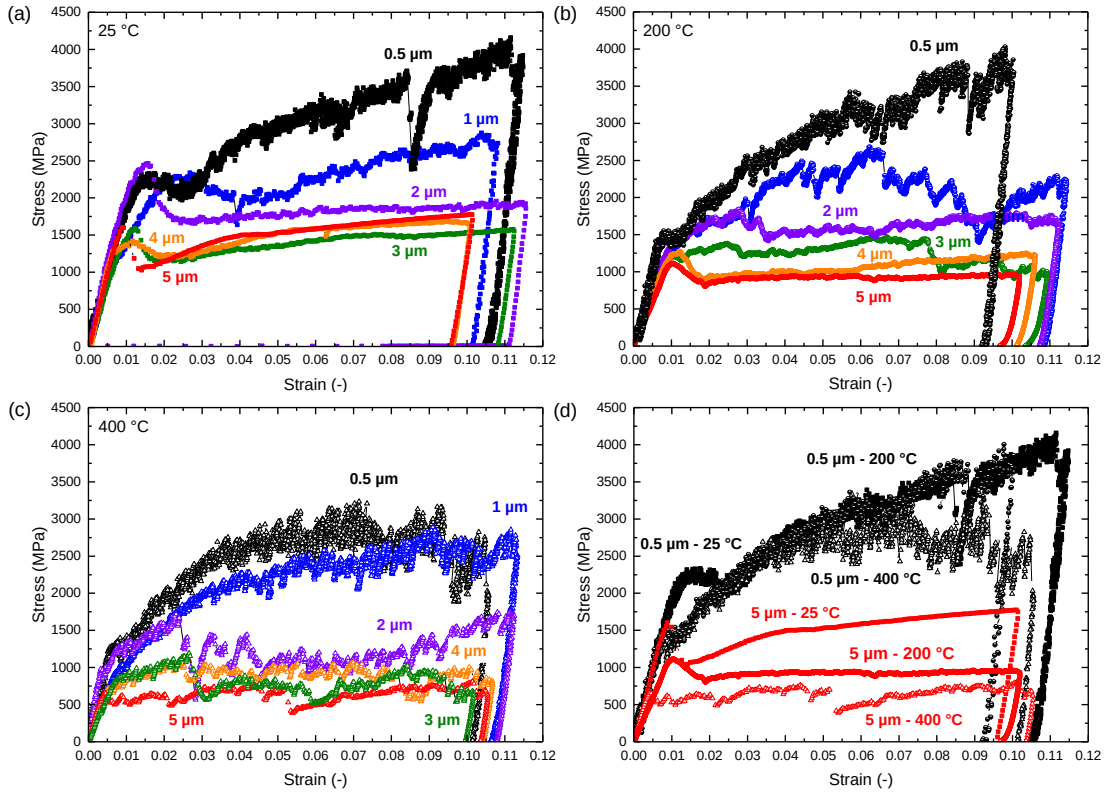

Figure 4.4: Typical compressive stress-strain curves of different W micropillars with diameters ranging from 0.5 to 5 µm tested at different temperatures, (a) 25 °C, (b) 200 °C and (c) 400 °C. (d) Comparison of stress-strain curves for micropillars of 0.5 and 5 µm diameter taken from (a), (b) and (c). Squared solid symbols represent micropillar tests performed at 25 °C while triangular open symbols depict tests performed at 400 °C and circular semi-open symbols at 200 °C.

Observing Figure 4.3 and Figure 4.4, it is clear that the apparent strain hardening behavior was size dependent. It increased with decreasing diameter as previously reported in other BCC studies [6,7,96,97,101]. This was quantified in Figure 4.5, which shows apparent strain hardening rate (SHR) as a function of pillar diameter at the different test temperatures. The SHR was determined as the slope in stress between 2 and 5% strain. Despite the significant scatter, a general trend was observed, where SHR values decreased with increasing temperature as opposed to what is observed for bulk BCC metals [21]. The W pillars generally showed a higher size dependence in the SHR than the Ta pillars, and the SHR values of W micropillars compressed at room temperature are consistent

with previous room temperature W pillar studies [97]. In addition, the difference in SHR values as a function of temperature was larger for the W pillars than for the Ta pillars.

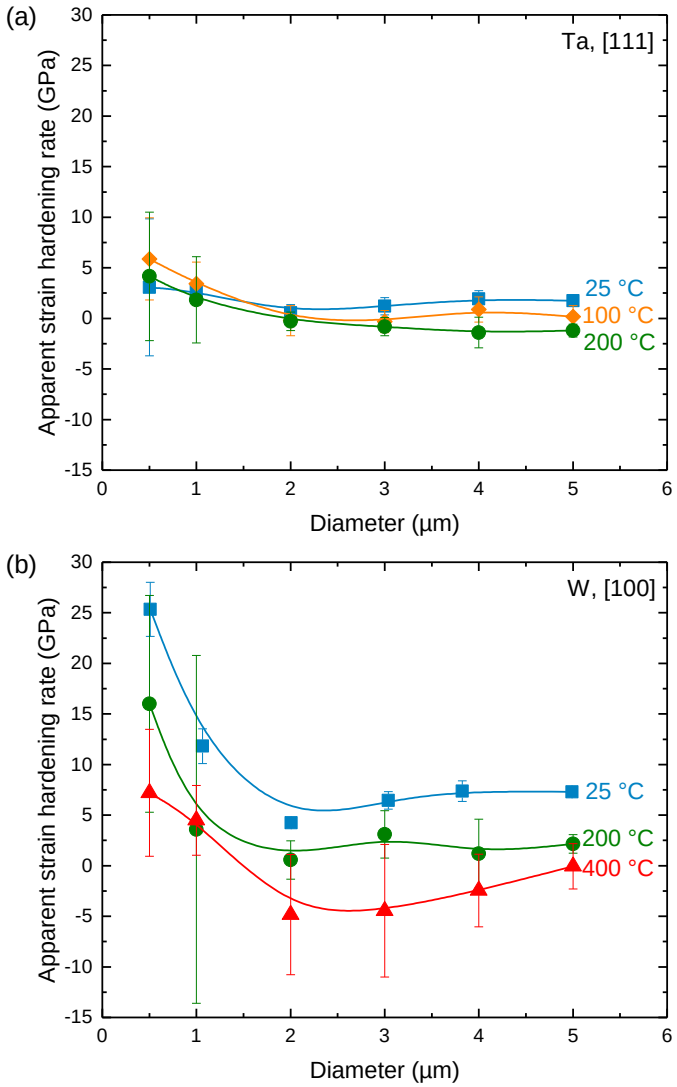

Figure 4.5: Temperature dependence of the apparent strain hardening rate in (a) Ta and (b) W as a function of pillar diameter. The blue squares correspond to the averaged strain hardening rate (SHR) at 25 °C while the orange diamonds correspond to the averaged SHR at 100 °C, the green circles to the averaged SHR at 200 °C and the red triangles to the averaged SHR at 400 °C. Error bars illustrate the standard deviations in the measured SHR.

4.3.3 Dependence of size effect on yield criterion and temperature

In contrast to bulk compression tests, where the yield stress is usually defined as the stress at 0.2% plastic strain, the yield stress for micropillars is commonly determined by the stress at a given total strain value, typically between 2 and 10% [5]. This is done in order to minimize errors due to the initial stiffness artifacts and to ensure that the stress considered as the yield stress is beyond the first observed yield event, but not affected by strain hardening [87]. Here, the yield stress was carefully evaluated given the stochastic

nature of the stress-strain curves and the noise shown by the compression system, which hindered the accurate determination of the yield stress.

The size effect on the strength of Ta and W micropillars is summarized in Figure 4.6. The considered flow stress values were taken directly from the data at a certain strain level regardless of the stochastic behavior of the smallest pillars. By plotting the flow stress and the micropillar diameter on a log-log scale, power-law exponents were determined for the linear fit, as shown in Figure 4.6a for both Ta and W samples at a total strain of 2.5% and at different temperatures. The stresses at 2.5% total strain were chosen in agreement with previous BCC micropillar studies [6,97,135]. This figure shows that flow stresses scaled inversely with the pillar diameter for both Ta and W samples, and more importantly, that test temperature had a significant influence on flow stress as also seen in high temperature nanoindentation measurements [172,173]. Interestingly, the data for Ta and W converged for small pillars, indicating that small pillars were less sensitive to temperature conditions as also reported by Schneider *et al.* [97]. Moreover, the room temperature flow stresses shown by both samples were consistent with previously reported data for W and Ta pillars [97,101].

For comparison, the power-law exponent was also calculated as a function of yield criterion, i.e., as a function of defined strain level. This was achieved by taking the stress values at different discrete strain values (every 0.025% strain) from 1 to 8% strain, and calculating, for each strain and respective stress level, the power-law exponent as shown for 2.5% strain in Figure 4.6a. Figure 4.6b and c depict the power-law exponents for the Ta and W samples. For W, the power-law exponents are shown for a strain range between 1 and 8% at different temperatures, while for Ta, only data between 1 and 5% are depicted as the larger Ta pillars were only deformed to a maximum strain of approximately 5% (see Figure 4.3b). The power-law exponents determined in this way exhibited a general tendency despite of the inherent stochastic behavior of the stress-strain curves. For both samples, the exponents remained fairly constant at 25 °C with increasing strain while at higher temperatures, the exponents increased with increasing strain. An averaged power-law exponent between total strain values of 2 and 5% was determined at each temperature as most BCC studies on size effects have used different strain levels ranging between 2 and 5% [6–8,97,98,101,135,166]. Data below 2% total strain were not considered because these were influenced by the elastic behavior of the micropillars and the stress peaks described above. The resulting deviations at low strains are particularly observed in Figure 4.6c for W micropillars.

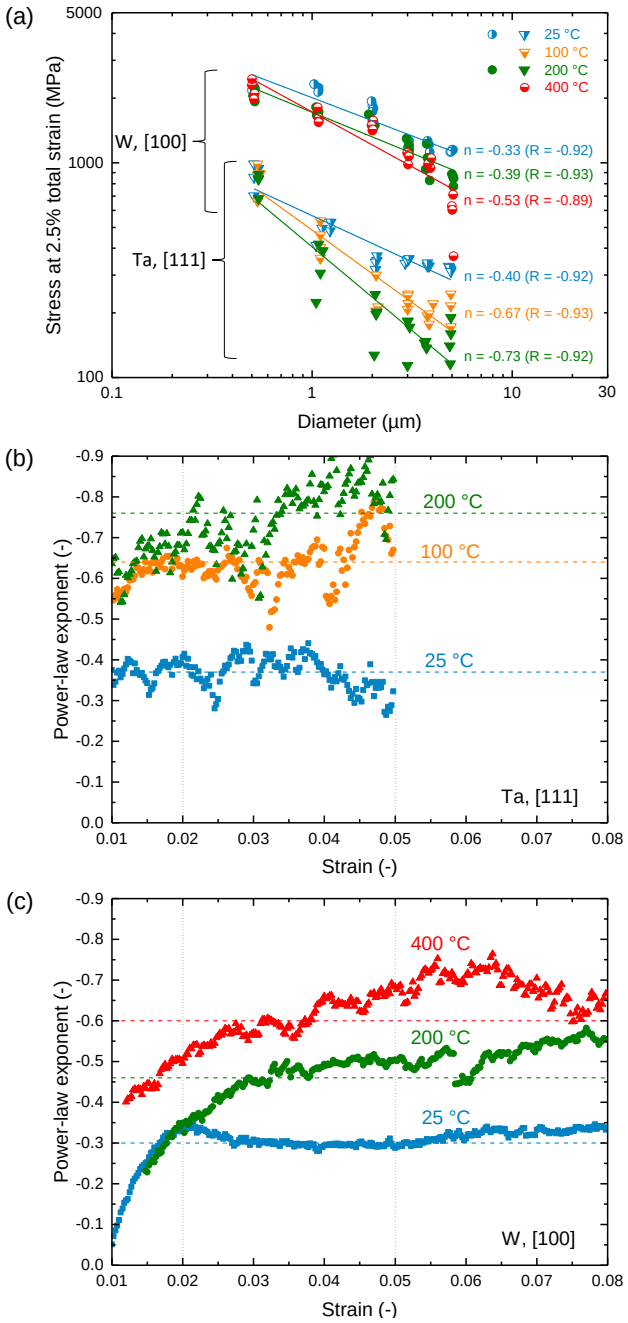

Figure 4.6: Temperature dependence of the size effect in Ta and W: (a) Log–log plot of the flow stress taken at 2.5% total strain as a function of the top diameter of the W and Ta micropillars in the temperature range 25-400 °C. The solid lines depict best fit power-law functions. Influence of the yield criterion (strain) on the power-law exponent, *n*, at different temperatures for Ta (b) and W (c). The dashed horizontal lines in (b) and (c) correspond to the average *n* values listed in Table 4.1 while the dotted vertical lines correspond to the lower and upper strain bounds of the average *n* values.

As seen in Table 4.1, the averaged power-law exponents *n* are - 0.37 ± 0.04, - 0.64 ± 0.06 and - 0.76 ± 0.07 for the Ta micropillars tested at 25, 100 and 200 °C and - 0.30 ± 0.01, - 0.46 ± 0.05 and - 0.60 ± 0.05 for the W micropillars tested at 25, 200 and 400 °C. A clear trend is observed that, with increasing temperature, the exponent increased in magnitude, reaching values that are in the range of previous FCC micropillar studies, i.e,

-0.6 [5,83,84,87,150]. The results obtained at room temperature for both Ta and W micropillars were in close agreement with the literature [7,101].

Table 4.1: Temperature conditions and averaged power-law exponents *n* obtained from 2 to 5% total strain results presented in Figure 4.6b and c. Critical temperatures taken from Ref. [7].

	Temperature T_{test} (°C, K)	**Melting temperature T_m (°C, K)**	**Critical temperature T_c (°C, K)**	**T_{test}/T_c**	**T_{test}/T_m**	**2-5% averaged total strain power-law exponent *n***
Ta, [111]	25 (298 K)	3017 (3290 K)	177 (450 K)	0.66	0.09	-0.37 ± 0.04
	100 (373 K)			0.83	0.11	-0.64 ± 0.06
	200 (473 K)			1.05	0.14	-0.76 ± 0.07
W, [100]	25 (298 K)	3422 (3695 K)	527 (800 K)	0.37	0.08	-0.30 ± 0.01
	200 (473 K)			0.59	0.13	-0.46 ± 0.05
	400 (673 K)			0.84	0.18	-0.60 ± 0.05

4.4 Discussion

4.4.1 Effect of temperature on the deformation morphology of BCC pillars

In the present study, Ta and W micropillars have, for the first time, been compressed at elevated temperatures. Ta micropillars were compressed at relatively large temperature ratios (test temperature/critical temperature between 0.66 and 1.05). Previous studies have shown two distinct deformation behaviors in BCC micropillars: a more localized slip deformation produced by the activation of a few slip systems, typically observed in BCC metals with low T_c (such as Ta), and a more uniform deformation (wavy slip) related to the cross-slip of screw dislocations, seen in BCC metals with a high T_c (such as W) [7]. These two different behaviors have been attributed to the temperature ratio, which, in turn, controls the mobility of screw dislocations. In view of this hypothesis, it is expected that, in our Ta micropillars, screw dislocations were relatively mobile. Hence, dislocations were mainly of mixed character and limited to specific slip planes. As a result of this confinement, localized slip was observed [7].

For W pillars, the elevated temperature tests shed light, for the first time, on a temperature-dependent change of deformation morphology from uniform deformation to localized deformation (see Figure 4.1 and Figure 4.2). This indicates that, indeed, the temperature ratio has a strong influence on the motion of dislocations. At temperature

ratios close to one, screw and edge dislocations have comparable mobility due to the thermal activation. Thus, mixed dislocations are bound to particular slip planes [7]. As a consequence, large pillars compressed at high enough temperatures show localized slip. As T_{test}/T_c decreases, screw dislocations become less mobile, and thus edge dislocations move faster toward the free surface of the micropillar, leaving the pillar in an edge dislocation-starved situation. Long and straight screw dislocation segments then lead the deformation via their ability to cross-slip between crystallographic planes which intersect along the ⟨111⟩ direction and cause a more uniform deformation of the pillar. In this respect, no transition from uniform to localized deformation is observed for the smallest W pillars with increasing temperature because the annihilation distance for edge dislocations will be shorter than for bigger pillars. Therefore, the pillars become edge-starved faster, so that the deformation is mainly controlled by the cross-slip of screw dislocations. This is in agreement with Figure 4.1, where uniform wavy slip is observed for 500 nm pillars regardless of test temperature. In addition, it has been proposed that the motion of screw dislocations may be enhanced by the increase of surface-to-volume ratio with decreasing pillar size [8,101]. The explanation given is that edge dislocations near the free surface may assist kink nucleation and hence improve the mobility of screw dislocations [101]. Thus, the lattice resistance would be more easily overcome and the strength for small micropillars would not necessarily increase with decreasing pillar size. Also, at the sub-micron scale, the deformation is believed to be dominated by dislocation surface nucleation [174]. Thus, the strength size dependence of nanopillars would be expected to be weaker [175]. This is observed for 500 nm diameter W pillars in Figure 4.6a, where a plateau in flow stress values is observed as the size decreases, i.e., flow stress values barely increase below 1 µm pillar diameter. The fact that the lattice resistance is more easily overcome at this size could also explain why the Ta and W pillars tested at different temperatures have the same strength.

4.4.2 Influence of yield criterion on size effects: effect of strain hardening on size effects

As can be seen in Figure 4.5, the SHR increases with decreasing sample size, as also observed for FCC and BCC micropillars compressed at room temperature [87,97,176]. This is in agreement with another BCC study of micropillar compressions performed at room temperature which has proposed that dislocation multiplication and related forest hardening are not the main factors for the strain hardening behavior as also observed for bulk BCC metals at temperatures well below T_c [21,135]. It has been observed that pre-

straining of Mo micropillars does not influence their hardening behavior [135]. Moreover, the 'reset' of their mechanical properties after repeated FIB machining suggests that their deformation is controlled by dislocation sources, i.e., defects caused by the ion cutting procedure. The strain hardening dependence of micropillars has been related to the same mechanism as observed in FCC micropillars, i.e., exhaustion hardening, where the consumption of the weakest dislocation sources increases the stress needed to activate another dislocation source [87,168]. Nevertheless, this size dependence may be an artifact stemming from the pillar taper angle, which varies slightly as a function of pillar size. Although the Ta micropillars show some correlation between pillar taper as a function of diameter and SHR, the W micropillars clearly exhibit no direct correlation between these two parameters. Thus, this suggests that pillar taper does not account for such a strong size dependence (see Table A.1 and Table A.2 in Appendix I: Taper angle vs. pillar diameter).

More importantly, Figure 4.5 shows that, for both Ta and W, the strain hardening behavior also depends on test temperature: lower SHRs are observed at higher temperatures. However, this temperature effect is opposed to bulk BCC metals, where the easier mobility of screw dislocations at higher temperatures increases dislocation forest hardening [21]. This different trend may be explained by the stress needed to activate a dislocation source, which can be approximated as being composed of an athermal nucleation stress, given by the nucleation barrier Q^* and activation volume V, and a thermal stress [175]:

$$\sigma = \frac{Q^*}{V} - \frac{kT}{V} ln \frac{kTN\nu_0}{E\dot{\varepsilon}V}. \qquad \text{Equation 4.3}$$

The latter term is characterized by a ratio between the thermal energy ($k \cdot T$) and V, given by the Boltzmann's constant k and absolute temperature T, as well as a logarithmic function based on the competition between the thermal ($k \cdot T \cdot N \cdot \nu_0$) and mechanical ($E \cdot \dot{\varepsilon} \cdot V$) parameters. N is the number of equivalent nucleation sites, ν_0 the nucleation rate, E the Young's modulus, and $\dot{\varepsilon}$ the strain rate. Assuming a relatively small V, in the range of 1 to 9 b^3 (characteristic of BCC micropillars compressed at similar strain rates) [136], and considering an elastic strain rate in the order of $5 \cdot 10^{-4}$ s^{-1}, an increase in the test temperature would be expected to decrease the nucleation stress. This was also suggested by atomistic simulations of surface dislocation nucleation [175]. A consequence will be a lower strain hardening as seen in Figure 4.3, Figure 4.4 and Figure 4.5. Moreover, the increase in strain hardening rate with decreasing sample size would explain the trend

shown in the power-law exponent-strain curves in Figure 4.6b and c, where a slight increment in the power-law exponent is observed as a function of increasing strain.

4.4.3 Size effects as a function of temperature

The present results indicate that the deformation mechanisms of sub-micron and micron-sized FIB machined BCC pillars depend on size as well as on temperature. In addition to an increase in yield strength with decreasing pillar diameter, both Ta and W pillars show lower yield strengths with increasing temperature (given a pillar diameter), as observed by Schneider *et al*. [8] for Mo only. This combined size and temperature dependence of strength of W and Ta micropillars can be assessed in terms of the different strengthening mechanisms as proposed by Parthasarathy *et al*. [113] (see Equation 4.2).

The strength is assumed to be the sum of a size independent bulk contribution and a size dependent contribution. For the latter, the statistical average length of the weakest single-arm dislocation source, $\bar{\lambda}_{max}$, must be calculated as the probability that a certain pillar with a diameter *d*, number *p* of dislocation sources and a primary slip plane oriented at an angle β to the compression axis has λ_{max} as the maximum source length [113]:

$$\bar{\lambda}_{max} = \int_0^{d/2} \left[1 - \frac{4\left(\frac{d}{2}-\lambda_{max}\right)\left(\frac{d}{2\cos\beta}-\lambda_{max}\right)}{\frac{d^2}{\cos\beta}}\right]^{p-1} \cdot \left\{\frac{4\left[\left(\frac{d}{2}-\lambda_{max}\right)+\left(\frac{d}{2\cos\beta}-\lambda_{max}\right)\right]}{\frac{d^2}{\cos\beta}}\right\} p\lambda_{max} d\lambda_{max}. \quad \text{Equation 4.4}$$

The number of sources, *p*, depends on the pillar dimensions (diameter *d* and height *h*) and initial mobile dislocation density ρ_{mob} as follows [113]:

$$p = Integer\left[\rho_{mob}\frac{\pi(d/2)^2 h}{L_{seg}}\right] = Integer\left[\frac{\pi\rho_{tot}(d/2)h}{s}\right], \quad \text{Equation 4.5}$$

where L_{seg} is the average length of dislocation segments in the pillar, considered to be the pillar radius, and *s* is the number of primary slip systems, which is 12 for BCC metals ({112}<111> [165]). FIB machined micropillars are non-defect free, so that it is assumed that the current Ta and W micropillars have a moderate total dislocation density, ρ_{tot}, characteristic of annealed single crystals, i.e., 10^{10}-10^{13} m^{-2} [113,142]. The dislocation density for both materials is assumed to be stable in the tested temperature range as temperature induced dislocation annealing, i.e., recovery, can be neglected at these low homologous temperatures (see Table 4.1).

The material parameters needed to evaluate the equation by Parthasarathy *et al.* are presented in Table 4.2. The lattice resistance values, τ_0, of Ta at different temperatures

were taken from Smialek *et al.* [177], who tested single slip oriented Ta single crystals at different temperatures at similar strain rates as in the present study. For W, no lattice resistance values are available for [100]-oriented single crystals in compression. However, data taken from Brunner [178], who performed tensile tests of W crystals up to 800 K, were used as a first approach. The temperature-dependent values of the shear moduli of [111]-oriented Ta and [100]-oriented W single crystals were taken from two different studies [179,180]. The weak temperature dependence of the Burgers vector was neglected.

Table 4.2: Material parameters of Ta and W at different temperatures.

Material	**Temperature (°C)**	**Schmid factor *S***	**τ_0 (MPa)**	**μ (GPa)**	**b ($\dot{A}$)**	**β (°) – slip plane orientation**
Ta	25	0.314	45 [177]	69 [179]	2.860	19.5
	100		15 [177]	68 [179]		
	200		~0	67.4 [179]		
W	25	0.471	384 [178]	159 [180]	2.741	35.3
	200		213 [178]	156 [180]		
	400		48 [178]	152 [180]		

Lattice resistance in shear, τ_0, of Ta from Ref. [177], and τ_0s of W from Ref. [178]. Corresponding shear moduli, μ, of W from Ref. [180] and of Ta from Ref. [179].

The yield stresses calculated from Equation 4.2, Equation 4.4 and Equation 4.5 as a function of size and temperature are shown in Figure 4.7. The predicted results for Ta agree very well with the experimental data. For W micropillars, the agreement between experimental and theoretical values is not as good as for the Ta pillars (Figure 4.7b): the experimental yield stress values are much less dependent on temperature than the calculated values; there are also indications that the size dependence is weaker than predicted. The predicted values generally come to lie below the experimental ones. While the assumed lattice friction stresses affect mainly the absolute level of the predicted yield stresses, the dislocation density strongly affects the size dependence. Lee and Nix [142] suggested that an increase in the dislocation density would affect the yield stress of pillars differently depending on their size: weakening for sub-micron-sized pillars and hardening for micron-sized pillars. Higher dislocation densities would then decrease the size effect as observed in Figure 4.7b and also by Lee and Nix [142]. This would also decrease the temperature dependence of the yield stresses as seen in Figure 4.7b. However, this does not explain yet the different sign of curvature shown by the W experimental data,

suggesting that other strengthening factors may govern the plastic deformation of W micropillars. For instance, the effective stress needed to yield might be affected by the enhancement of the screw dislocation mobility due to kink nucleation at the pillar surface [97,134]. Due to the larger surface to volume ratio, the lattice resistance would be more easily overcome with decreasing pillar size. Thus, less mechanical work than expected would be needed to overcome the lattice friction for the small W pillars. The fact that the lattice friction values of Ta are close to zero at the current temperature regime might explain why the model works well for Ta, while for W, with larger lattice friction values, the model does not follow the experimental trend. In addition, this might also explain why the W pillars are less sensitive to temperature changes as sample size decreases.

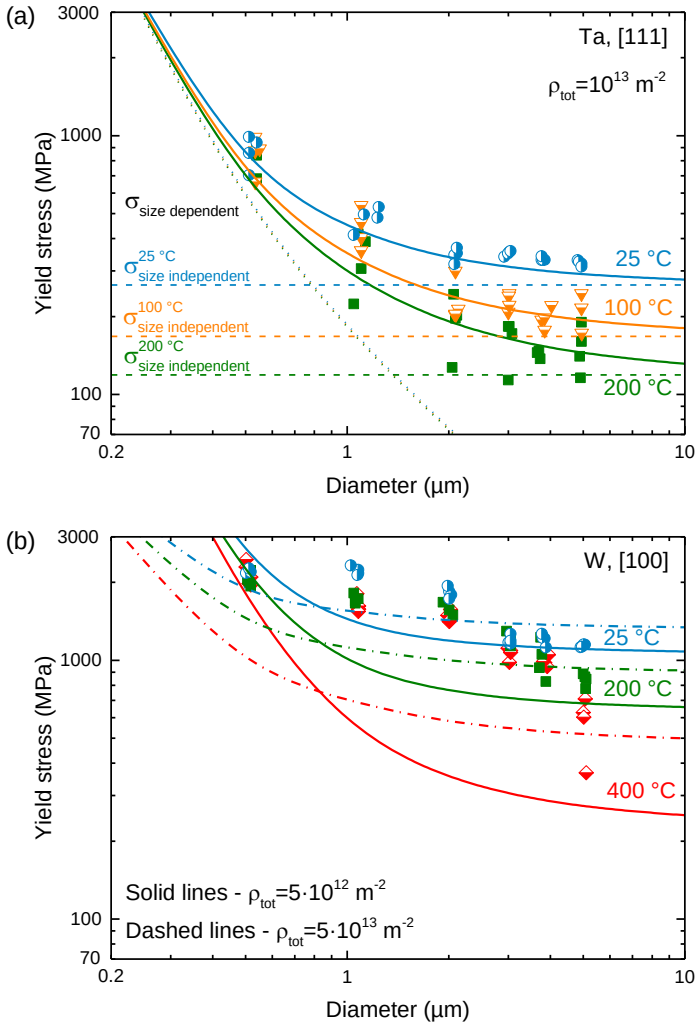

Figure 4.7: Comparison between experimental yield stresses determined at 2.5% total strain and calculated ones using the model by Parthasarathy *et al.*(Eqs. 2, 4 and 5) of (a) Ta micropillars compressed at 25, 100 and 200 °C and (b) W micropillars tested at 25, 200 and 400 °C. In (a), the solid lines represent the predicted yield stresses as a function of pillar diameter, assuming a dislocation density of 10^{13} m^{-2}. The dashed and dotted lines correspond to the size independent and size dependent contributions to the yield stresses, respectively. In (b), the solid lines correspond to the predicted yield stresses assuming a dislocation density of $5\cdot10^{12}$ m^{-2} while the dashed-dotted lines correspond to an alternative calculation with a dislocation density of $5\cdot10^{13}$ m^{-2}.

The different power-law exponents shown by the Ta and W micropillars can be correlated with the relative test temperature, i.e., T_{test}/T_c, as first shown by Schneider *et al.*[7]. The lattice resistance strongly depends on T_{test}/T_c for BCC metals [14]. Thus, it is expected that size effects scale with this relative test temperature [7]. Figure 4.8 provides an overall view of power-law exponents as a function of this temperature ratio. The average experimental power-law exponents of Ta and W micropillars shown in Table 4.1 for the current study are depicted (closed symbols) together with a schematic of the different exponents observed for other BCC metals [7,8,97,101,135,137]. In addition, the power-law exponents for Ta and W micropillars predicted by the model of Parthasarathy *et al.* are presented (open symbols). As observed in Figure 4.8, the power-law exponents of the Ta and W micropillars decrease with increasing relative test temperature as was previously reported for Mo [7,8]. It is emphasized that the present results fit well into the overall picture: for relative temperatures approaching 1 (for W: 400 °C, Ta: 200 °C), a size dependence typical for FCC micropillars [83,87], with $n \leq -0.6$, is found. The pillars tested at higher temperatures show a more negative exponent, i.e., a more pronounced size effect, which indicates that the size-independent terms in Equation 4.2 lose in relative importance. This could be explained, for example, by a progressive decrease in the lattice resistance. On the defect level, this behavior can be attributed, as suggested previously [8], to the important role of screw dislocations: as their mobility increases with rising temperature, especially when the critical temperature is exceeded, the deformation approaches that of FCC metals.

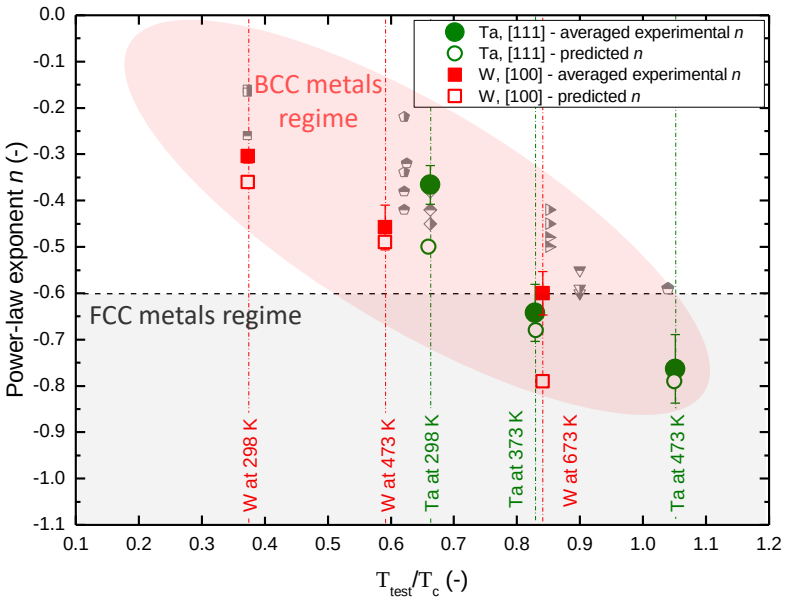

Figure 4.8: Power-law exponent n as a function of the relative test temperature T_{test}/T_c. The solid symbols represent the experimental results of this work while the open symbols depict the theoretical prediction of n calculated according to the model by Parthasarathy *et al.* Included for comparison are different size effects of BCC micropillars determined in other studies [7,8,101,137].

Also, the experimental power-law exponents of Ta agree reasonably well with the exponents predicted using the single-arm dislocation source model. However, the predicted power-law exponents of the W micropillars compressed at 400 °C are much lower than the experimental ones. The fact that the predicted yield stresses calculated as a function of the pillar diameter do not capture the experimental trend produces such overestimation of the size effects. As discussed above, the actual W micropillars may have larger initial dislocation density and lattice resistance values than the ones used for the estimation, which together with other strengthening mechanisms, may produce this disparity. Nevertheless, it is apparent that the initial dislocation density and temperature dependence of the lattice friction play an important role in determining the size dependence on strength of micropillars. Assuming a constant initial dislocation density with increasing temperature, the lattice resistance dictates the size effect in BCC micropillars as a function of temperature.

In order to arrive at a better estimate of the different strengthening mechanisms and to go beyond this study, knowledge of the initial dislocation density of the pillars would be helpful. Moreover, the determination of the exact lattice resistance of the samples as a function of temperature would be of significant importance since it has been observed that it plays a crucial role in the deformation of BCC micropillars. Also, questions arise regarding the emergence of plastic flow and evolution of plasticity (strain hardening) in BCC micropillars and its temperature dependence, which are directly related to the activation of single-arm dislocation sources, surface dislocation annihilation, dislocation storage and consequent dislocation interactions. Therefore, *in situ* transmission electron microscopy compression experiments as well as computational simulations would give further fundamental information to the understanding of BCC plasticity confined in micron-sized samples as a function of temperature.

4.5 Conclusion

For the first time, elevated temperature compression tests were carried out on [111]-oriented Ta and [100]-oriented W pillars with diameters of a few micrometers in order to study the influence of temperature on the size effect. The following conclusions can be drawn:

- The temperature ratio (T_{test}/T_c) has a strong influence on the relative motion of screw and edge dislocations. Slip traces characteristic of localized single slip were observed on the surfaces of the tested Ta pillars irrespective of test temperature. In W pillars, a change from uniform wavy deformation to localized deformation was observed with increasing temperature and pillar size.
- The stress-strain behavior became more stochastic as the pillar size decreased, and their plastic intermittencies (load drops) were altered by the amount of thermal energy provided: at higher temperatures, plastic intermittency was qualitatively larger.
- The apparent strain hardening behavior was not only size dependent but, more importantly, test temperature dependent. Despite significant experimental scatter, strain hardening was clearly found to decrease with increasing temperature. This effect was attributed to easier activation of dislocation sources near the surface and better dislocation mobility at higher temperatures.
- Both materials exhibited larger size effects at higher temperatures. The size dependence scaled with the ratio of test temperature to critical temperature. For test temperatures close to or larger than T_c, FCC size dependence was reached.
- The contributions of bulk strength and size-dependent stresses to size effects at different temperatures were analyzed by using the single-arm dislocation source model. While the model reproduced the Ta results very well, it could not capture the experimental trend shown by the W micropillars. Assuming a constant initial dislocation density, the temperature-dependent size effects of BCC micropillars depend mainly on the magnitude of the lattice resistance (T_{test}/T_c).

By reporting microcompression tests at elevated temperatures, this work provides new evidence on the effect of temperature on the plasticity of micron-sized BCC samples as well as further insight into their deformation mechanisms. Such studies help to establish a basis for the design of BCC metal microstructures in high-temperature applications and to estimate material strength for a given sample dimension.

4.6 Acknowledgements

The authors thank Prof. Dr. C. Motz from the Department of Materials Science and Methods, Saarland University (Saarbrücken, Germany), and Dr. A. Caron from the INM-Leibniz Institute for New Materials for valuable discussions about data analysis and interpretation. Also, thanks to Mr. B. Medina Clavijo for his assistance. E. A. acknowledges partial support through the European Union's Seventh Framework Program (FP/2007-2013) / ERC Grant Agreement No. 340929.

5 Size dependent deformation of β-CuZn

Previous research has shown that size scale in the micron to sub-micron regime strongly influences material strength, reaching into the Gigapascal range. However, the influence of crystal structure on this ‘size-effect’ is not well understood. The vast majority of these studies have focused on FCC and BCC metals. Therefore, investigation into other crystal structures has the potential for developing a more comprehensive understanding. In the present chapter, the deformation behavior of β-CuZn, which has a CsCl (B2) crystal structure and a low thermal component to the room temperature strength, was studied through the compression of focused ion beam manufactured pillars with diameters ranging from 200 nm to 5 μm. The size dependence of β-CuZn is found to be close to that observed in FCC metals although the deformation processes differ significantly. While its dislocation behavior resembles that of FCC metals, its slip behavior is typical of BCC metals. Furthermore, the crystal orientation dependence of the yield strength changes as sample size decreases. These findings are discussed in the context of the mobility of screw dislocations as well as surface dislocation nucleation, which might promote such a change in orientation dependence.

5.1 Introduction

For metals, the investigation into the mechanical deformation behavior has overwhelmingly shown that mechanical strength increases when size decreases down to the micron and sub-micron regime [1,104,181,182]. Plasticity remains strongly linked to material defects: specimens considered to be relatively defect-free exhibit strengths near the theoretical limit [105,183,184] while other manufacturing techniques, which leave behind inherent defects, such as electroplating [185,186], nanoprinting [187,188] and focused ion beam (FIB) machining [4,86,87] lead to a so-called 'size effect'. It is generally believed that dislocations annihilate on the surface, and therefore dislocation nucleation processes that scale with the smallest sample dimension dominate strength. This size effect is hallmarked by an inverse power-law relationship between the specimen diameter and yield strength, usually written as:

$$\sigma_y = \sigma_0 + kd^n, \qquad \text{Equation 5.1}$$

where σ_y is the yield strength of the small specimen, σ_0 the bulk yield strength, k a material constant, d the pillar diameter, and n the power-law exponent.

Investigations into the size effect using innovative manufacturing techniques continue to emerge, yielding insights into fundamental dislocation behavior. For example, several authors have compressed pillars made of body-centered cubic (BCC) metals [6–8,95–101,132,166]. The load required for dislocation motion in BCC metals is thought to be controlled, at comparatively low temperatures, by the high lattice friction (i.e. Peierls) stress of the $1/2\langle 111\rangle$ screw segments [20,21,165]. This leads to a strong temperature and strain rate dependence of the flow stress. Each BCC metal can be characterized by a critical temperature, T_c, (sometimes referred to as a knee or athermal temperature) at approximately 0.2 the absolute melting temperature [24]; above T_c, the mobility of screw and non-screw dislocations is similar, as is generally the case for face-centered cubic (FCC) metals [32]. Small-scale compression studies of BCC pillars have demonstrated that n (Equation 5.1) is significantly smaller in magnitude than observed for FCC metals. This implies that the effect of screw dislocation mobility affects the size dependence. Furthermore, comparison between several BCC metals has shown that as T_c approaches room temperature, n increases in magnitude towards the 0.6 value observed for FCC metals. Consistent with these observations and predictions by a modified single-arm

dislocation source model [142], we have recently confirmed, by elevated temperature testing of Mo, Ta and W at T_c, that n increased in magnitude to 0.6 [8,189]. All BCC compression pillar studies have focused on pure metals with a critical temperature above room temperature.

β-CuZn, with a B2 crystal structure, possesses a T_c below room temperature (i.e., 20% of its melting temperature, approximately -45°C). It has been observed that the slip plane in β-CuZn varies with temperature and crystallographic orientation, sometimes deviating from the maximum resolved shear stress plane. Ardley and Cotrell showed that the tensile flow stress of β-CuZn single crystals below room temperature increased rapidly with decreasing temperature as is often the case for pure BCC metals [48]. Below 115 K, slip occurs predominantly on the $\langle 111 \rangle \{112\}$ slip system while at room temperature, slip takes place mostly on the $\langle 111 \rangle \{110\}$ slip system. The opposite change of the slip system from the $\{110\}$ plane at lower temperatures to the $\{112\}$ plane at higher temperatures has been observed for other BCC metals, and is attributed to the specific core structure of the screw dislocations [165]. Slip traces in compressed β-CuZn single crystals have been shown to be long and straight irrespective of crystal orientation [43]. Nevertheless, the distribution of slip is dependent on crystal orientation: specimens with the loading axis close to the $[001]$ orientation show coarse slip in comparison to $[\bar{1}49]$, $[\bar{1}11]$ and $[011]$-oriented crystals. The closer the specimen is to the $[001]$ orientation, the coarser the slip is [43]. In addition, alloys with a B2 structure are known to show slip vectors parallel to either the $\langle 100 \rangle$ or $\langle 111 \rangle$ crystallographic directions. For instance, dislocation motion along the $\langle 100 \rangle \{110\}$ slip system has been observed for other B2 alloys such as NiAl [36,64] and CoTi [190]. The slip direction in any given B2 alloy is thought to be governed by a complex interplay of elastic anisotropy, displacement vectors of metastable stacking-fault-like defects, and energies of these faults [37]. For β-CuZn, several studies have convincingly demonstrated that the $\langle 111 \rangle$ direction is preferred [53,55,61,63], leading to relatively ductile behavior.

β-CuZn occupies an intermediate position between BCC and FCC metals at room temperature. While the slip behavior is typical of BCC metals, the dislocation behavior resembles that of FCC metals; the mobilities of edge and screw dislocations are comparable. Thus, the purpose of this study was to determine how much β-CuZn inherits from BCC and FCC structures at the (sub-) micron scale in terms of plasticity. The size and orientation dependent deformation behaviors were studied above the critical temperature. We discuss the mechanisms controlling such behavior in the context of

dislocation motion in BCC and FCC metals, highlighting the influence of dislocation annihilation and nucleation at the free surface in the sub-micron sized pillars. With the exception of shape-memory alloys [10,11], which undergo a stress-induced martensitic phase transformation, we are aware of no studies that have explicitly investigated the size effect in a B2 alloy.

5.2 Experimental method

A bulk polycrystalline β-CuZn sample of nominal composition Cu-47 wt% Zn with a diameter of approximately 10 mm and a thickness of 5 mm was produced by arc melting 99.999% pure Cu and Zn (MaTecK GmbH, Jülich, Germany). The sample was subsequently annealed in an argon atmosphere at 600 °C for 60 min followed by furnace-cooling to room temperature. An average grain size of approximately 1100 µm was measured following the linear intercept method on EBSD images. The cylindrical specimen was ground with silicon carbide particles of decreasing grit size down to 5 µm using a custom made holder to produce parallel-sided samples. Then, it was electropolished at 1.5 V for approximately 4 min in a 60 wt% H_3PO_4 and H_2O solution in order to reduce the damaged layer produced by the grinding procedure. X-ray and electron backscatter diffraction verified that the material was single-phase with the fully ordered B2 crystal structure.

The specific pillar fabrication process and data interpretation techniques used in this study are similar to previous work [9,84,189]. Free-standing cylindrical pillars were fabricated using a dual FIB and scanning electron microscope (SEM) (FEI Versa 3D DualBeam), where a gallium ion beam voltage of 30 kV and final currents ranging between 100 and 10 pA were used. Pillar diameters ranged from approximately 5 µm to below 200 nm, with aspect ratios (length:diameter) near 3:1. Fabrication of pillars with the sample surface held normal to the FIB invariably creates a slight taper, listed in Table 5.1 (further details in Table A.3 of Appendix I: Taper angle vs. pillar diameter). The taper angle was determined by measuring the length, top and bottom diameters of the pillars from SEM images taken from a 38° angle with respect to the base of the specimen. The pillar diameter measured at the top of the column was used to calculate the stress, which represents an upper bound to the stress experienced by the sample.

To test the influence of crystal orientation, compression samples were FIB machined in four grains with average orientations close to [001], [$\bar{1}$49], [$\bar{1}$11] and [011]. For this purpose, an EBSD map of the grain structure was obtained before pillar cutting. The actual crystal orientation of each grain is shown in Table 5.1 alongside the intended ideal orientation, relative crystal rotation and Schmid factor for the expected slip systems. These crystal orientations were chosen so that single slip, multiple slip on equivalent and on dissimilar slip systems could take place. These were determined assuming that slip occurred on the systems with the highest resolved shear stresses (Schmid's law). From here on, all orientations will be referred to as [001], [$\bar{1}$11], [011] and [$\bar{1}$49].

A Hysitron PI 87 SEM Picoindenter (Minneapolis, MN) equipped with a flat tipped pyramidal indenter with a 10 μm diagonal was used to perform *in situ* compression testing inside the dual FIB/SEM. To estimate the actual deformation of the pillars, the elastic deformation beneath the pillar during compression was calculated by applying the solution of a cylindrical punch pressed into an elastic half-space [87,157] and subtracting it from the measured total deformation. A total of 168 pillars were compressed at a constant stress rate of 30 MPa/s. Moreover, to determine the strain rate dependence, further compression tests of 96 pillars with diameters of 200 nm and 2 μm oriented along the [$\bar{1}$11] and [$\bar{1}$49] directions were carried out at different strain rates (10^{-2}, 10^{-3} and 10^{-4} s^{-1}).

Table 5.1: Grain orientation, taper angle and calculated Schmid factors for the β-CuZn grains from which pillars were manufactured.

Grain orientation	**Intended grain orientation**	**Crystal rotation (°)**	**Taper angle (°)**	**Schmid factor**		
				⟨111⟩{110}	**⟨111⟩{112}**	**⟨100⟩{110}**
[$\bar{1}$ 1 8]	[001]	10.0	2.7 ± 1.5	0.45	0.50	0.17
[$\bar{1}$ 6 12]	[$\bar{1}$49]	3.0	2.9 ± 1.0	0.50	0.44	0.33
[$\bar{12}$ 13 13]	[$\bar{1}$11]	2.3	2.5 ± 1.1	0.30	0.34	0.48
[$\bar{3}$ 19 18]	[011]	6.7	2.7 ± 0.9	0.44	0.50	0.41

After compression, all pillars were imaged via SEM. Also, eight pillars with a square cross-section with an edge length of 2 μm and aspect ratio 3 were fabricated in each grain using the dual FIB/SEM. They were manufactured to better identify the active slip systems. The pillars were cut such that the different faces were crystallographically defined. This was achieved by using the EBSD technique *in situ* in the dual FIB/SEM. Based on the angles between the slip traces on both side faces of the samples and the compression axis, the determination of the active slip systems was possible. This was

carried out in a similar way as described by Cao *et al.* [191]. The specimens with the $[001]$ loading axis were prepared such that the side faces included the (100) and (010) crystallographic planes. For the $[\bar{1}49]$-oriented pillars, the planes $(1\bar{2}1)$ and $(11\,5\bar{1})$ were chosen as side faces, while the pillars with the $[\bar{1}11]$ loading axis were machined with the side faces oriented on (110) and $(1\bar{1}2)$ crystallographic planes. The $[011]$-oriented pillars were machined in a way that the (001) and $(01\bar{1})$ planes were side faces.

In addition, a 1 µm thick lamella and a ~100 nm thin TEM lamella were fabricated from two different $[001]$-oriented pillars with a diameter of about 2 µm using the dual FIB/SEM and an argon polishing machine (Nanomill - Fischione Instruments, Export, PA). Both lamellae were cut with their faces parallel to the (010) crystallographic face. The thick lamella was cut out to be scanned via EBSD in a way similar to that shown by Kheradmand and Vehoff [192] while the thin lamella was made for TEM imaging purposes. The fabrication procedure was the following: First, a 100 nm thick layer of platinum coating was deposited using electron beam induced deposition followed by the deposition of another platinum layer of 2 µm using ion beam induced deposition on both pillars. The rationale for this was to protect them from sputtering of the ion beam during lamella fabrication. The pillars were then cut using the FIB to a thickness of approximately 1 µm before being transferred to a TEM grid using a micromanipulator inside the FIB. Subsequently, the first thick lamella was polished using beam currents as low as 30 pA at a gallium ion beam voltage of 30 kV and further polished using the argon polishing machine operated at 900 V and 112 µA. The last step was done to reduce the damage produced. The thick lamella was observed under EBSD conditions in the dual FIB/SEM. The second lamella was thinned to a final thickness of approximately 100 nm using the FIB and subsequently polished using the argon polishing machine under the same beam conditions as the first lamella. The TEM sample obtained was observed under bright-field imaging using a JEOL JEM-2100 LaB6 (Tokyo, Japan) operated at 200 kV.

5.3 Results

5.3.1 Deformation morphology - Slip analysis

Figure 5.1 shows SEM images of representative β-CuZn pillars after compression. Compressed micropillars exhibited slip bands visible on the surface of the pillars irrespective of size and crystal orientation. This has consistently been reported previously for pure FCC and BCC metals, e.g., refs. [4,6,7,83–85,87,90,97,100,135,193]. In Figure 5.1, ridges are observed on the pillar side faces. These are artifacts that stem from the FIB process, an effect called curtaining that is caused by surface and material inhomogeneity [194]. Most of the 200 nm diameter pillars exhibited defined slip steps. While the pillars oriented along the [001] and $[\bar{1}11]$ exhibited traces of multiple slip (see Figure 5.1a and g), the $[\bar{1}49]$ and [011]-oriented pillars showed traces of mainly one primary slip system (see Figure 5.1d and j).

All compressed pillars thicker than 200 nm exhibited an 'S' shape in which multiple slip traces were observable on the pillar surfaces (see Figure 5.1b, c, e, f, h, i, k and l). To better observe the slip traces present on the surface of the pillars, Figure 5.2 shows square cross-section pillars with a width of 2 µm and different crystal orientations that were compressed up to 5% strain. The 'S' shape was also visible for the square cross-section pillars. Analysis of the slip traces shown in Figure 5.2a evidences the activation of multiple slip systems on a [001]-oriented pillar. On each of the side faces, (010) and (100), three sets of well-defined and straight slip lines were observed. These sets likely correspond to the ⟨111⟩{110} slip system family; the rationale for this conclusion is as follows. Considering Schmid's law and the rotation of the crystal lattice with respect to the [001] orientation (see Table 5.1), there are two equivalent slip systems of the ⟨111⟩{110} family that are expected to dominate the plastic deformation. These are $[\bar{1}11](101)$ and $[1\bar{1}1](011)$, which have a Schmid factor of 0.45. The former slip system is supposed to form a 38° angle between the slip trace and the parallel to the pillar top surface on the (010) plane and a 7° angle on the (100) plane, and the latter slip system vice versa. These expectations match the observations in Figure 5.2a, where angles of approximately 38° and 8° are visible. In addition, there are two equivalent slip systems more from the same family that closely match the traces shown on the [001] pillars side faces in Figure 5.2a. These are the $[111](\bar{1}01)$ and the $[111](01\bar{1})$, which

are actually the next most favorably oriented systems, with a Schmid factor of 0.43. The first one exhibited a 51° angle on the (010) and a 8° angle on the (100) plane while, according to Schmid's law, it should show a 52° angle on the (010) and a 7° angle on the (100) plane. The second one showed the opposite traces on both faces. These slip traces should be compared with possible $\langle 100\rangle\{110\}$ slip systems. Nevertheless, it is improbable that the slip lines shown in this figure were caused by the activation of slip systems of this family since the Schmid factor of the $\langle 100\rangle\{110\}$ slip system with such slip traces is very low (0.17) (see Table 5.1) and has never been reported for bulk β-CuZn. Also, the slip lines observed in this figure most probably do not belong to the $\langle 111\rangle\{112\}$ slip family since the expected angles for these systems do not match the observed ones.

In Figure 5.2b, the slip traces of a $[\bar{1}49]$-oriented pillar are depicted. In this case, several sets of reasonably well defined slip traces are observed, and these seem to belong primarily to $\langle 111\rangle\{110\}$ slip systems. From the Schmid factor calculations (see Table 5.1), we would expect primarily $\langle 111\rangle\{110\}$ slip systems. Particularly, the $[111](\bar{1}01)$ slip system shows the highest Schmid factor (0.5), which might correspond to two sets of slip lines shown in Figure 5.2b since the angles measured are in close agreement with the ones estimated using Schmid's law. A ~3° angle was observed on the $(11\ 5\bar{1})$ face and a~45° angle on the $(1\bar{2}1)$ face. These resemble the calculated ones: a 2° angle on the $(11\ 5\bar{1})$ face and a~46° angle on the $(1\bar{2}1)$ face. Looking again at the most favorable systems, there are two more slip systems, $[\bar{1}11](101)$ and $[11\bar{1}](011)$, with the second and third highest Schmid factor (0.47 and 0.28, respectively) of the $\langle 111\rangle\{110\}$ slip family that might be visible in Figure 5.2b. While $[\bar{1}11](101)$ would lead to slip lines forming approximately a 47° angle on the $(11\ 5\bar{1})$ face and a 43° angle on the $(1\bar{2}1)$ face, the $[11\bar{1}](011)$ would exhibit a 16° angle on the $(11\ 5\bar{1})$ face and a 12° angle on the $(1\bar{2}1)$ face. In addition, two of the observed sets of slip might belong to the $\langle 111\rangle\{112\}$ slip system family since they also match the expected angles dictated by Schmid's law. These are the $[111](\bar{2}11)$ and the $[111](11\bar{2})$, which possess high Schmid factors, 0.44 and 0.42, respectively. According to Schmid's law, the former would form angles between the slip lines and the parallel to the top surface of 37° on the $(11\ 5\bar{1})$ face and 47° on the $(1\bar{2}1)$ face. The latter, instead, would from an angle of 40° on the $(11\ 5\bar{1})$ face and 47° on the $(1\bar{2}1)$ face, closely resembling the slip traces observed in Figure 5.2b. Observing the smallest pillars between 200 and 500 nm in diameter (see Figure 5.1d), it seems that these mainly show one preferential slip system

that might correspond to the $[111](\bar{2}11)$ since the observed slip line angle configuration does not match any other possible slip system. This is better observed in Figure 5.3a, where a 200 nm diameter pillar shows one single slip that corresponds to such slip system. This exhibits an angle of approximately 46° on the $(1\bar{2}1)$ face and an angle of 37° on the $(11\ 5\bar{1})$ face.

Figure 5.2c and d show the slip traces on $[\bar{1}11]$ and $[011]$-oriented pillars, respectively. These two specimen orientations exhibited less defined slip traces, which strongly hindered the determination of the active slip systems. This might be due to the high loading symmetry and therefore multiple slip of these crystal orientations. Moreover, the pronounced ridges present on some of the side faces as a consequence of the FIB machining process further complicated the determination of the active slip systems. Nevertheless, in the 2 µm diameter pillars with $[\bar{1}11]$ orientation, several low angle slip systems could be observed. These form angles of approximately 20 and 30°, which correspond to slip on $\{110\}$ planes. On the other hand, only one slip system could be identified for $[011]$-oriented pillars. This slip system forms a 48° angle between the slip trace and the top surface on the $(01\bar{1})$ face and a 1° angle on the (001) face, which can only be indicative of a $\langle 111\rangle\{112\}$ slip system since no $\langle 111\rangle\{110\}$ slip system matches such angle configuration. Particularly, the $[111](\bar{2}11)$ slip system seems to be active with the highest possible Schmid factor of 0.5. This can be also observed for a 200 nm square cross-section pillar in Figure 5.3b, which shows the activation of this slip system for a 200 nm square cross-section pillar oriented along the $[011]$ direction.

To further investigate the deformation morphology of the compressed pillars and elucidate its origin, a bright field TEM image, an EBSD map, a kernel average misorientation (KAM) map and a misorientation distribution map of two 2 µm diameter pillars oriented along the $[001]$ direction are shown in Figure 5.4. Dislocations are observed throughout the length of the pillar extending into the bulk material below (Figure 5.4a), with no evidence of twinning or phase transformation as shown in the EBSD map (Figure 5.4b). Interestingly, dislocations are shown to accumulate in different bands, probably as a consequence of the activation of different slip systems as seen in the TEM image and the KAM map (Figure 5.4a and c). The KAM map is used to determine the areas of the pillars with higher dislocation densities. Such a map quantifies the local misorientation within a pillar, i.e., the average misorientation around a measurement point with respect to a set of nearest neighboring points. This gives higher values for deformed

areas, which are correlated to higher geometrically necessary dislocation densities within the microstructure [192,195]. Furthermore, the local misorientation of the pillar with respect to a pristine crystal orientation (sample substrate) is depicted in Figure 5.4d. This shows that the misorientation of a [001]-oriented pillar is present primarily within the core of the pillar, contained in two dislocation bands as observed in Figure 5.4c and d. Such slip bands form an angle of approximately 51° between the slip band and the top surface of the pillar. These traces likely correspond to the $[111](\bar{1}01)$ slip system, as previously stated and observed in Figure 5.2a.

In summary, these results are consistent with bulk β-CuZn studies, which have convincingly demonstrated that the main operative slip system at room temperature is $\langle 111\rangle\{110\}$ regardless of crystal orientation [43,53,55,61,63]. However, there are indications that also $\langle 111\rangle\{112\}$ slip systems are activated for $[\bar{1}49]$ and [011]-oriented pillars. Table 5.2 summarizes the different slip systems observed as a function of crystal orientation.

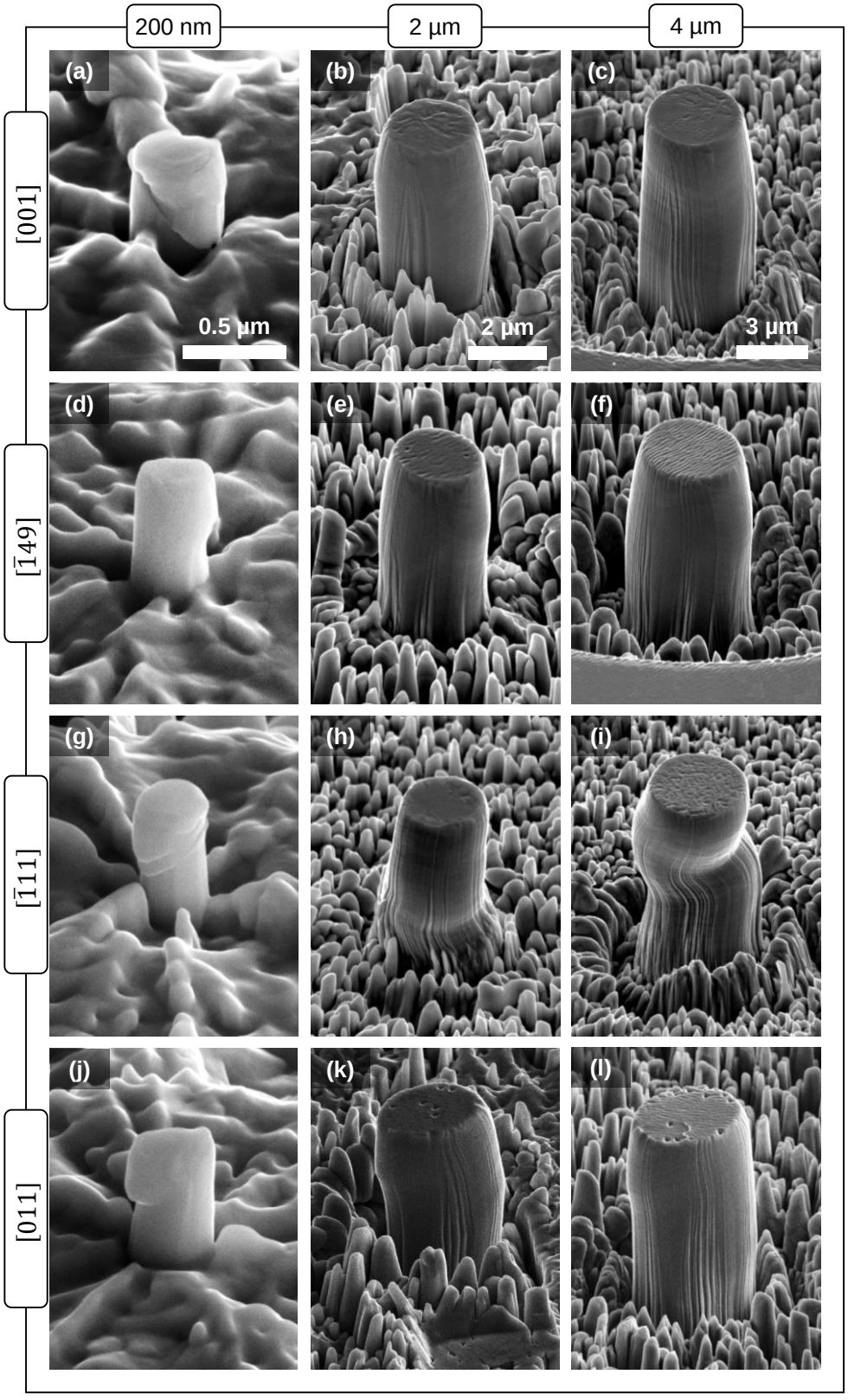

Figure 5.1: Scanning electron microscopy images of pillars after compression, with nominal diameters of 200 nm, 2 and 4 µm. With exception of the 200 nm diameter pillars, all pillars exhibit an ‘S’ shape.

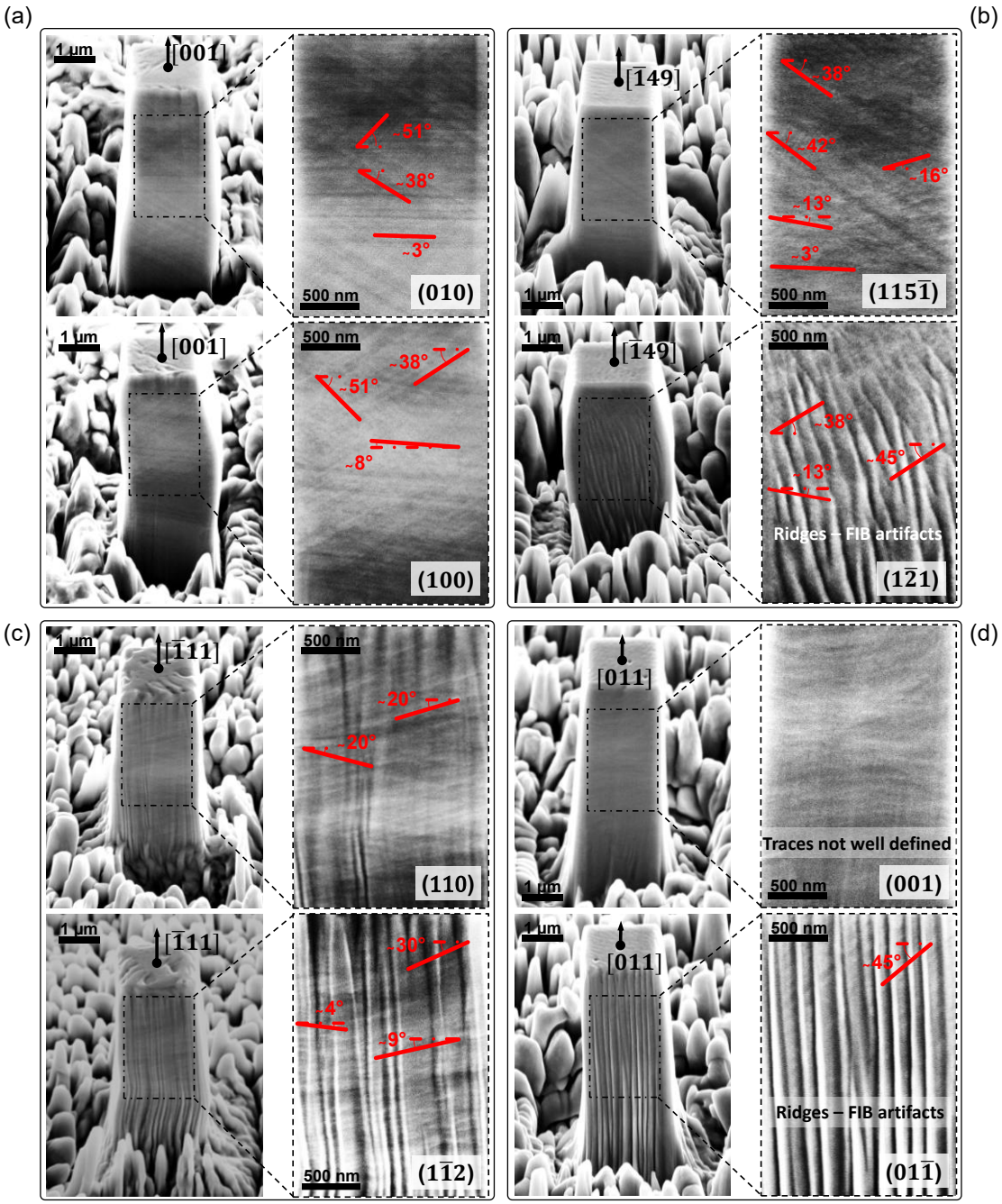

Figure 5.2: Scanning electron microscopy images of pillars with square cross-section and crystal orientations: (a) [001], (b) [$\bar{1}$49], (c) [$\bar{1}$11] and (d) [011]. Compressive strain was up to 5%. The ridges shown on some of the side faces are a consequence of FIB machining and were already present before testing.

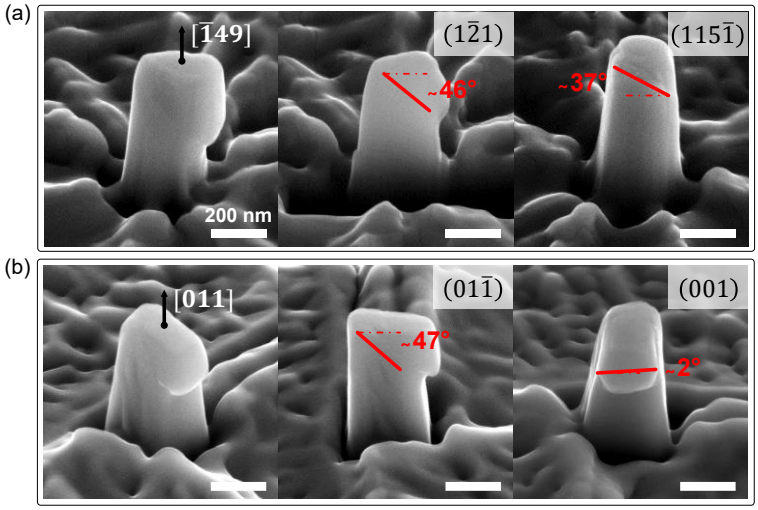

Figure 5.3: Scanning electron microscopy images of (a) a 200 nm diameter pillar oriented along the $[\bar{1}49]$ direction and (b) a square cross-section pillar with a side length of approximately 200 nm and oriented along the $[011]$ direction. Both pillars show the activation of $\langle 111 \rangle \{112\}$ slip systems.

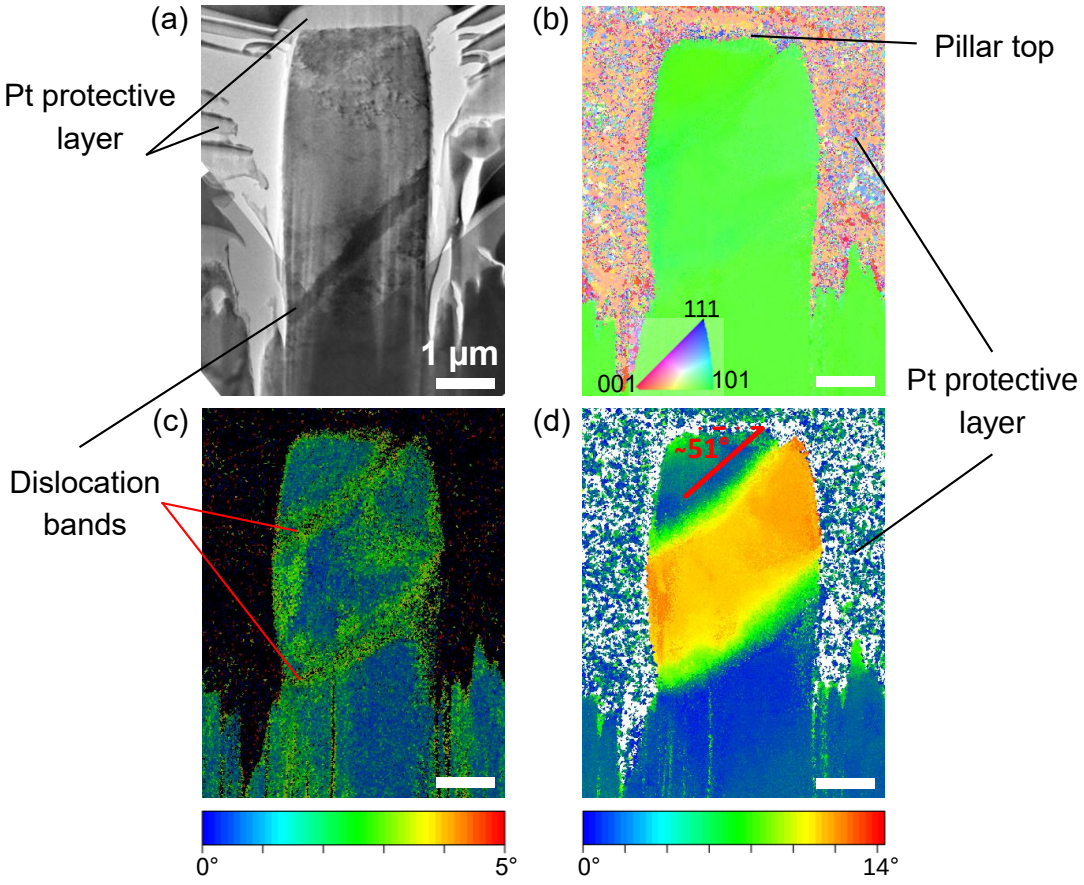

Figure 5.4: (a) Transmission electron microscopy image, (b) electron backscatter diffraction map, (c) kernel average misorientation (KAM) map and (d) misorientation angle distribution map with respect to the pristine orientation in the bulk material of two post-compression pillars sectioned using focused ion beam machining. The contrast band evidenced in (a) as well as green color bands in (c) and (d) are oriented along ~51° with respect to $[001]$] and correspond to dislocations in $\{110\}$.

Table 5.2: Summary of the slip systems observed in the compressed pillars as a function of crystal orientation.

Grain orientation	Observed slip system	Schmid factor	Expected angles between top surface and side face (°)	
			(010)	(100)
[001]	$[\bar{1}11](101)$	0.45	38	7
	$[1\bar{1}1](011)$	0.45	7	38
	$[111](\bar{1}01)$	0.43	52	7
	$[111](01\bar{1})$	0.43	7	52
			$(1\bar{2}1)$	$(115\bar{1})$
$[\bar{1}49]$	$[111](\bar{1}01)$	0.5	46	2
	$[\bar{1}11](101)$	0.47	43	47
	$[11\bar{1}](011)$	0.28	12	16
	$[111](\bar{2}11)$ (only system observed for 200 nm diam. pillars)	0.44	47	37
	$[111](11\bar{2})$	0.42	47	40
			(110)	$(1\bar{1}2)$
$[\bar{1}11]$	Ill-defined slip traces			
	$[111](\bar{1}10)$		18	33
	$[111](\bar{1}01)$	0.3	18	21
			$(01\bar{1})$	(001)
[011]	Ill-defined slip traces			
	$[111](\bar{2}11)$	0.5	48	1

5.3.2 Stress-strain response

Stress-strain behavior of representative β-CuZn compression pillars with diameters ranging from 5 µm to 200 nm are shown in Figure 5.5 as a function of crystal orientation. These stress-strain curves have distinctive features typical of load-controlled micropillar deformation. During the initial loading (well under 1% strain), relatively low and inconsistent stiffness values are recorded. This is thought to be caused by pillar surface features and initial seating of the indenter on the pillar [87]. Quickly the stiffness increases and the pillar undergoes elastic loading, until a critical point is reached and strain increases sharply under a constant applied load. Interestingly, such strain bursts remained prevalent for relatively large diameters. This is in contrast with previous studies on various FCC and BCC metals that have shown decreasing strain bursts for pillar diameters

of 2 µm or larger [6,7,84,97,135]. Nevertheless, bulk deformation of β-CuZn has demonstrated 'jerky' or 'serrated' flow stress, somewhat resembling the strain bursts observed in micropillar testing [48,49].

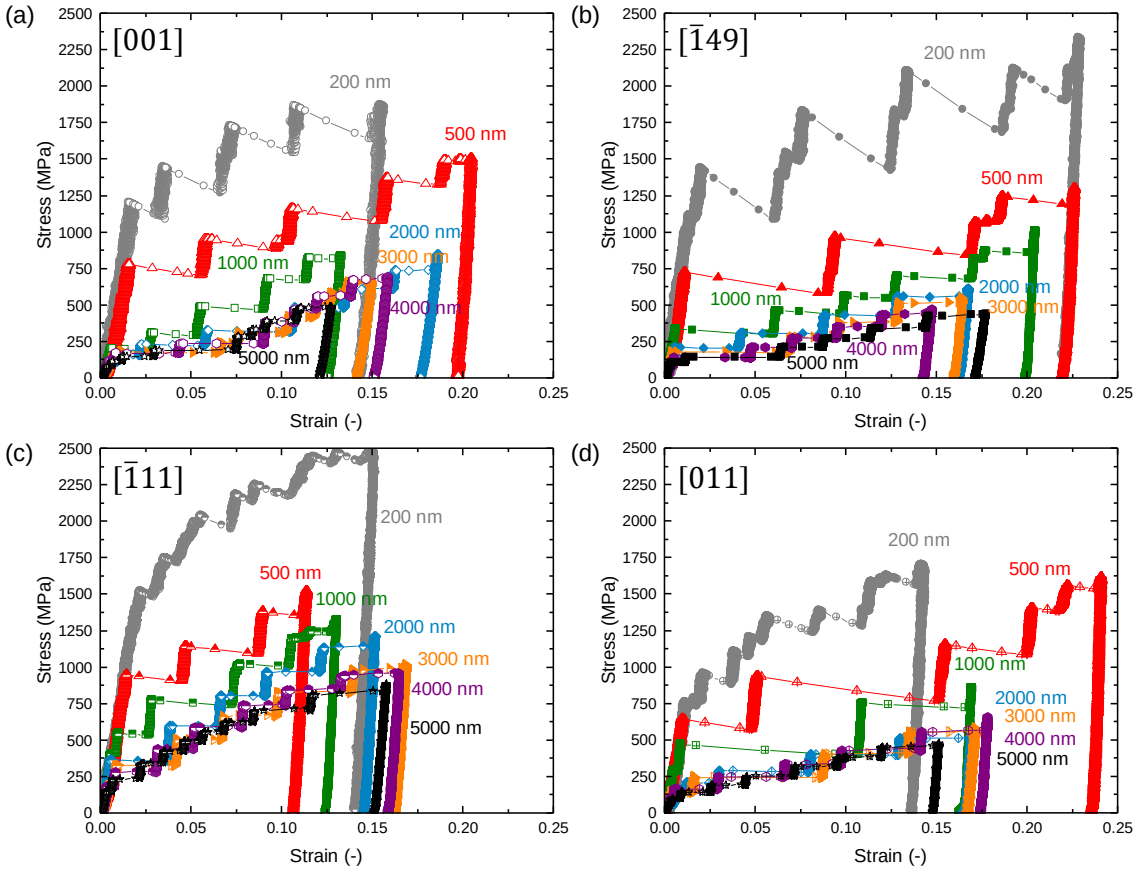

Figure 5.5: Representative stress-strain behavior of β-CuZn compression pillars. The curves fundamentally change shape with decreasing diameter.

Figure 5.6a shows the critical resolved shear stress (CRSS) values at 2.5% strain for all samples tested. A 2.5% strain value was chosen because it is beyond the first observed strain burst, yet still low enough to be minimally affected by strain hardening. Although there is evidence of the activation of ⟨111⟩{112} slip systems in some cases, particularly at the sub-micron scale, the resolved shear stresses were determined assuming slip occurred preferentially on ⟨111⟩{110} systems; these were compared to bulk behavior, which has shown ⟨111⟩{110} slip at room temperature [43,53,55,61,63]. Figure 5.6a clearly demonstrates that the yield strength increased as the diameter of the β-CuZn pillars decreased. CRSS values of bulk single crystals with a similar composition and crystal orientations (adapted from refs. [59,61]) are also shown for comparison. It is plausible that a size effect is still prevalent for the largest pillars. All pillars showed comparable critical shear stress values for the different crystal orientations, giving rise to similar best-fit power law curves. This is evidenced in Figure 5.6b, which depicts the orientation

dependence of the power-law exponent as a function of strain. At 2.5% strain, best fit power law curves yield *n* values ranging from -0.65 to -0.54, similar to previous FCC [5,83,84,87,193] and high temperature BCC pillar studies [8,189]. A characteristic of this graph is that the power-law exponent decreases in magnitude at strain levels beyond about 3%, a behavior different to that of BCC metals, which has shown a slight increase in magnitude of the power-law exponent with increasing strain level [133,189]. The fact that the power-law exponent changes in magnitude with strain level (see Figure 5.6b) implies that the apparent strain hardening behavior is size dependent.

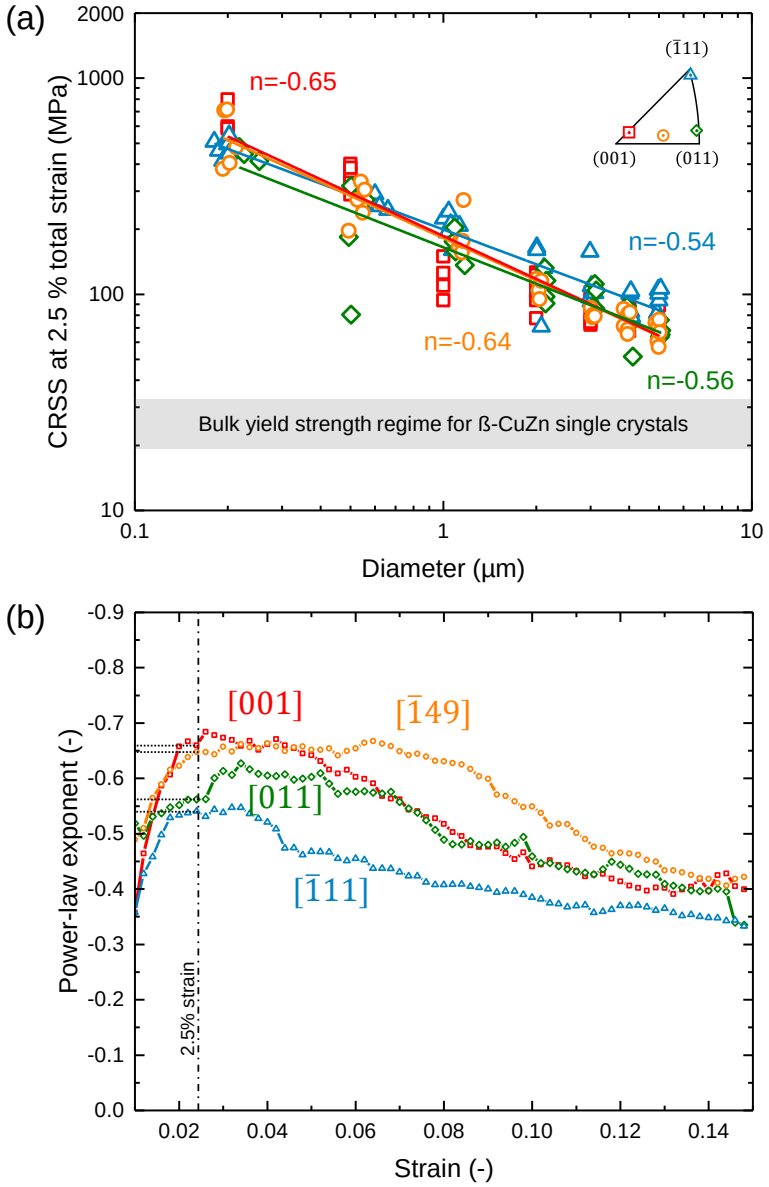

Figure 5.6: Analysis of stress-strain curves: (a) Critical resolved shear stress measured (CRSS) at 2.5% strain as a function of pillar diameter for all cylindrical samples tested at a constant stress rate of 30 MPa/s and (b) crystal orientation dependence of the power-law exponent as a function of strain. The bulk strength regime in (a) is adapted from refs. [59,61] and corresponds to single crystals with similar composition and heat treatment. The power-law exponents *n* denoted in (a) are indicated in (b) with dotted lines.

Typically, the crystallographic orientation dependence of BCC plasticity has been characterized by an angle χ, defined as the angle between the maximum resolved shear stress plane (MRSSP) and the $(\bar{1}01)$ plane (all of them with $[111]$ zone axis). This method has been mainly employed because of the non-planar core structure and associated high lattice friction of the $1/2\langle 111\rangle$ screw dislocations, which dominate the plastic deformation of BCC metals and β-CuZn at low temperatures [20,56]. Thus, plastic deformation occurs primarily by cross-slip on $\{110\}$ planes along the $[111]$ direction, leading to apparent slip planes (i.e., MRSSPs). Figure 5.7 shows the variation of the average CRSS at 2.5% strain for all specimens tested at 30 MPa/s as a function of crystallographic orientation. The value of χ is positive when the MRSSP lies between the $(\bar{1}11)$ and $(\bar{2}11)$ planes on the great circle of the $[111]$, and negative when it lies between the $(\bar{1}01)$ and $(\bar{1}\bar{1}2)$ planes [30]. As observed in Figure 5.7, the crystal orientation dependence of the CRSS seems to be size dependent in spite of the notable scatter shown by the 200 nm diameter pillars, where the sign of the slope (see solid lines) changes from small pillars (200 nm to 1 μm in diameter) to larger pillars (2 to 5 μm). This change can be better observed for the pillars oriented along the $[\bar{1}49]$ loading direction ($\chi \approx 0°$): the smallest pillars, with diameters between 200 nm and 1 μm, show higher strength values while the largest pillars, 5 μm in diameter, exhibit lower strength values compared to the pillars oriented along the other crystal directions. Note that special effort was made to keep the taper angle of the pillars independent of crystal orientation, so that crystal orientation dependences could be evaluated (see Table A.3 in Appendix I: Taper angle vs. pillar diameter).

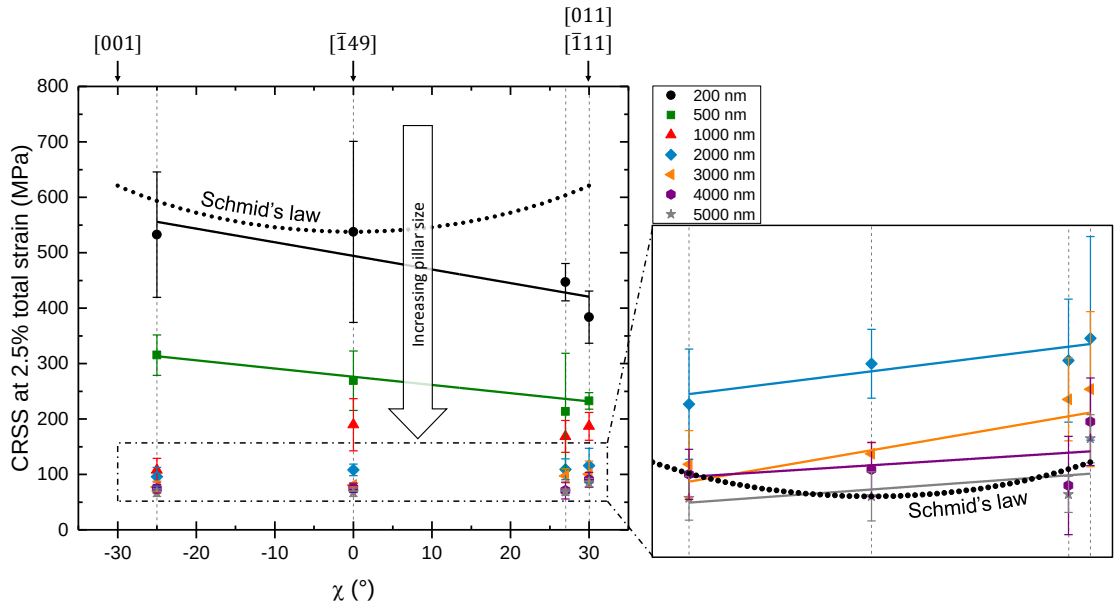

Figure 5.7: Average critical resolved shear stress (CRSS) at 2.5% strain against the angle χ, defined as the angle between the normal of the MRSS plane and the pole of the $(\bar{1}01)$ plane when [111] is taken as the slip direction. The error bars correspond to the standard deviation of the different CRSS values of the compressed pillars. The solid lines shown in the inset indicate the trend of the average CRSS values as a function of crystal orientation. The dotted lines correspond to the trend that the 5 µm and 200 nm diameter pillars would follow if Schmid's law applied.

To interpret the orientation dependence of the yield stress as a function of specimen size, it is worth studying the strain rate sensitivity of β-CuZn pillars. Tests conducted at different constant strain rates, between $2\cdot10^{-4}$ and $2\cdot10^{-2}$ s^{-1} for 200 nm and 2 µm diameter pillars oriented along the [$\bar{1}$11] and [$\bar{1}$49] loading axis, are shown in Figure 5.8. It is seen that the flow stress at 2.5% strain is slightly dependent on strain rate irrespective of pillar size and crystal orientation, as in bulk β-CuZn [196]. This behavior is quantified through the rate sensitivity and the activation volume. The rate sensitivity *m* is defined as [197]:

$$m = \frac{\partial \ln \sigma}{\partial \ln \dot{\varepsilon}}. \qquad \text{Equation 5.2}$$

The activation volume *V* can be determined as follows [31,197]:

$$V = \frac{kT}{S}\left(\frac{\partial \ln \dot{\varepsilon}}{\partial \sigma}\right), \qquad \text{Equation 5.3}$$

where *S* is the Schmid factor, *k* Boltzmann's constant, *T* the absolute temperature, $\dot{\varepsilon}$ the strain rate and σ the stress. The calculated strain rate sensitivity *m* and activation volume *V* values for 200 nm and 2 µm diameter pillars oriented along the [$\bar{1}$11] and [$\bar{1}$49] directions are shown in Table 5.3. The strain rate sensitivity slightly increased with decreasing specimen size and remained fairly constant as a function of crystal orientation. It ranged approximately from 0.01 to 0.06. With decreasing pillar size, the activation volume was found to decrease considerably regardless of crystal orientation: pillars with

a 2 µm diameter exhibited larger V values, between $44.7 \cdot b^3$ and $76.6 \cdot b^3$, where $b = a_0\sqrt{3}/2$ is the Burgers vector of β-CuZn and $a_0 = 0.4$ nm its lattice constant. By contrast, pillars with a diameter of about 200 nm showed V values between $3.8 \cdot b^3$ and $6.4 \cdot b^3$.

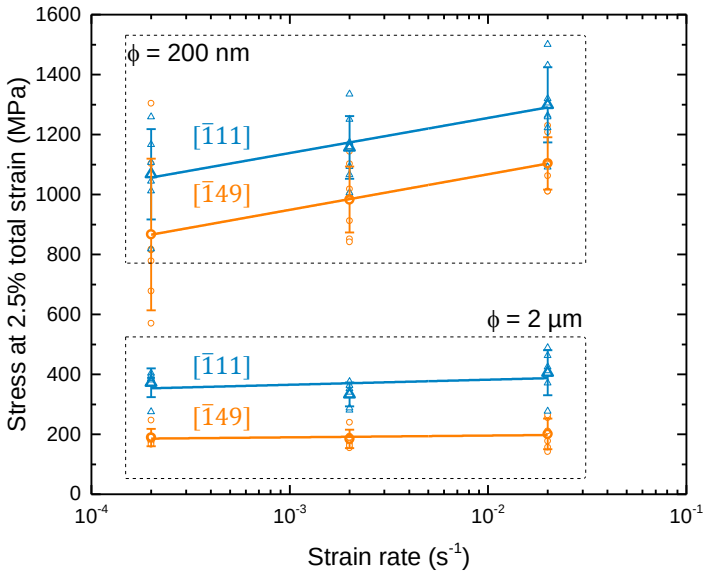

Figure 5.8: Flow stress measured at 2.5% strain versus strain rate for 200 nm and 2 µm diameter pillars with [$\bar{1}$11] and [$\bar{1}$49] crystallographic orientations. Bold data points correspond to the averaged flow stress values, and error bars represent the standard deviation in the measured flow stress. Eight pillars per size, crystal orientation and strain rate were compressed.

Table 5.3: Strain rate sensitivity m and activation volume V determined from constant strain rate compressions on pillars oriented along the [$\bar{1}$11] and [$\bar{1}$49] directions.

Crystal orientation	Pillar diameter (µm)	m	V ($\cdot b^3$)
[$\bar{1}$49]	2	0.009	76.6
[$\bar{1}$49]	0.2	0.059	3.8
[$\bar{1}$11]	2	0.017	44.7
[$\bar{1}$11]	0.2	0.044	6.4

5.4 Discussion

5.4.1 Unconventional serrated plastic flow

β-CuZn pillars with different crystal orientations and diameters ranging from 200 nm to 5 µm in diameter have been compressed at room temperature. Beyond initial yielding, the β-CuZn pillars exhibited unique deformation behavior in the following way. Large strain bursts were observed for relatively large diameters (>1 µm) (see Figure 5.5) compared to

previous FIB manufactured pillar studies of BCC materials (e.g., refs. [6–8,94,95,97–100,135,166]). Strain bursts are typical of load-controlled pillar compression testing, and have been shown via *in situ* TEM to be correlated to dislocation motion at the (sub-) micron scale [82]. However, bulk β-CuZn has exhibited 'serrated' flow similar to the strain behavior seen in micropillar testing [48,49]. This phenomenon has also been observed in numerous bulk materials, including other intermetallics with a B2 structure, and has been mainly attributed to plastic instabilities such as dynamic strain aging [198,199] or kinking [34,74]. Their origin mainly stems from a dislocation locking mechanism caused by either the diffusion of solute atoms into the cores of the dislocations or change of APB planes by climb dissociation or activation of non-favorable slip systems triggered by a first elastic buckling [73,200].

Kinking is an alternative deformation mechanism for materials that are unfavorably oriented to exhibit conventional slip. It has only been observed in intermetallic compounds with a B2 structure that experience slip in the ⟨100⟩{110} family [34,74]. Consequently, ⟨100⟩-oriented single crystals present a zero Schmid factor. Plastic flow under these conditions can only be initiated by elastic buckling and further activation of other slip systems. The comparison of the Schmid factors of the possible slip systems shows that kinking is not expected since the ⟨111⟩{110} or the ⟨111⟩{112} systems exhibit relatively high Schmid factors irrespective of crystal orientation (see Table 5.1). This coincides with our pillars, which generally seemed to deform by ⟨111⟩{110} slip (Figure 5.2), as in bulk β-CuZn [43,53,55,61,63]. This also indicates that the 'S' shape observed in our micron-sized pillars (Figure 5.1 and Figure 5.2) is not caused by either kinking or any stress induced phase transformation or deformation twinning. This together with the fact that the EBSD analysis (see Figure 5.4b) shows no indication of crystal reorientation or phase change provide strong evidence that the 'S' shape observed in our deformed micron-sized pillars (Figure 5.1 and Figure 5.2) is caused by another locking mechanism.

In situ TEM experiments have shown jerky motion of ⟨111⟩ superdislocations below 200 °C, which might be related to the pinning of these by local climb events [50,52]. Despite the fact that the authors disagree in the extent of climb dissociation operation, it is clear that, in a temperature regime between room temperature and 200 °C, diffusional mechanisms are active in β-CuZn. Climb dissociation events probably occur during glide as a consequence of interactions with point defects (e.g., vacancies). Climb-dissociated dislocations are sessile apart from pure screw dislocations. Hence, this mechanism might

explain the jerky flow behavior observed for our pillars. This would also explain why the slip traces observed on pillars larger than 200 nm in diameter are so fine compared to FCC or BCC metals.

5.4.2 Size and crystal orientation dependence of yield strength

It is remarkable that the β-CuZn pillars have a yield strength size dependence *n* between -0.54 and -0.65 consistent with that of FCC FIB manufactured pillars [5,83,84,87,193], although their plasticity is more complex than in pure FCC or BCC metals, e.g. due to superpartial formation [62]. An important general principle seems to arise from this observation: for negligible effective Peierls potential in a BCC or B2 structure, the size dependence of plastic strength is controlled by the similar deformation processes as in FCC metals. This also agrees with the fact that the β-CuZn pillars tested in this study have rather similar size dependence irrespective of crystal orientation. Furthermore, the slip traces observed on the pillar free surfaces correspond, mostly, to the ones determined by Schmid's law. Hence, this indicates that cross-slip might be limited at room temperature and further corroborates that β-CuZn behaves similarly to FCC metals. This is in accordance with previous studies on bulk BCC metals and β-CuZn, which showed that, at temperatures close to or above their critical temperature, the motion of $1/2\langle 111\rangle$ screw dislocations is comparable to that of edge dislocations, and thus the need for cross-slip is reduced [7,55].

If Schmid's law is applied to the present tests, the CRSS should be proportional to $\cos^{-1}(\chi)$ [30,201]. In Figure 5.7, the Schmid's law orientation dependence of the CRSS for 5 μm diameter pillars is depicted in the inset as a black dotted line. It is observed that, for large pillars (3-5 μm in diameter), the experimental values of CRSS slightly deviate from the crystal orientation dependent trend dictated by Schmid's law (see black dotted line). This is consistent with room temperature studies on bulk β-CuZn, which showed a similar trend [56]. In the sub-micron regime (200 to 500 nm diameter), however, the orientation dependence of the CRSS changes, showing a likely breakdown of Schmid's law (see black dotted line for the 200 nm diameter pillars); the stress required for plastic deformation shows a peak at a crystal orientation χ of approximately 0°. This observation is supported by the slip line analysis performed on the pillars via SEM imaging, which has shown that, at the sub-micron regime, activation of non-favorable slip systems belonging to the $\langle 111\rangle\{112\}$ family may dominate the plastic deformation (see Figure

5.3). Similarly, a breakdown of Schmid's law has been previously reported for FCC pillars as sample size decreased in the sub-micron range [202]. This has been explained through the comparison between Al micropillar compression experiments and Monte Carlo simulations, which have shown that, at this size scale, the slip system with the highest Schmid factor is not necessarily activated, but rather the one which comprises the longest dislocation source [202].

Also, it cannot be ruled out that FIB damage might promote the activation of dislocations on less favorable slip systems, as is evidenced by the activation of ⟨111⟩{112} for the 200 nm diameter pillars. This might be caused by either a change in the atomic order or the implantation of Ga. It is known that the addition of a third element to a B2 material causes a change in the anti-phase boundary energy and thus in the separation of superpartial dislocation pairs. In particular, it has been shown that alloying β-CuZn causes a change in the slip system, from ⟨111⟩{110} to ⟨111⟩{112} [43,203]. Moreover, it has been demonstrated that the addition of a third element facilitates the separation of superpartial dislocations and thus leads to planar slip [43,203]. This would explain why the pillars with diameters of only 200 nm show well defined slip steps at the free surfaces (see Figure 5.1), preferentially confined to specific slip planes, as well as a different orientation dependence of the yield strength of sub-micron β-CuZn pillars.

5.4.3 Strain rate sensitivity

The tests performed at constant strain rates (see Figure 5.8) show that the flow stress at 2.5% strain depends slightly on strain rate irrespective of pillar size and crystal orientation. The strain rate sensitivity *m* ranges from approximately 0.01 to 0.06, revealing considerably lower sensitivity than that shown for compression of FCC and BCC micropillars. Copper and nickel typically show *m* values between 0.08 and 0.11 for pillars ranging in diameter between 75 and 500 nm [197,204] while molybdenum shows *m* values between 0.07 and 0.1 for pillars with diameters varying between 200 nm and 5 µm [6]. Most investigations concerning jerky flow in bulk materials have concluded that negative *m* determined the occurrence of jerky flow [200,205]. This is not the case in the current study, although *m* values are very low. A modeling study has suggested that jerky flow might not necessarily lead to a negative *m* unless a combination of different dislocation locking mechanisms is present [206], which might explain why negative *m* values are not observed for our pillars.

With decreasing pillar size, the activation volume decreases considerably: pillars with a 2 µm diameter show V values up to $76.6 \cdot b^3$ while pillars with a diameter of about 200 nm reveal V values down to $3.8 \cdot b^3$. Similar scaling laws have also been observed in other microcompression studies on FCC [197,204] and BCC metals [6,97], where the metals with the largest size effect on strength exhibited also the largest size effect on activation volume. This also applies to the current β-CuZn pillars, which show a stronger size effect on strength and activation volume than BCC metals. This is directly related to thermally activated deformation processes. Materials with a high T_c, such as BCC metals, are expected to show a stronger dependence of the yield stress on strain rate, and thus smaller activation volumes irrespective of pillar size. This consequently reduces their actual size dependence of the activation volume.

For FCC metals [197,204], a similar increase in strain rate sensitivity and decrease in activation volume with decreasing sample size has been observed. This has been attributed to a change of the mechanism governing plastic deformation: conventional dislocation-dislocation interaction at the macroscale is replaced by truncated dislocation sources causing dislocation multiplication at the micron scale and by surface-controlled dislocation nucleation at the nanoscale [118,197,204]. For BCC metals, however, the plastic deformation is strongly dependent on the relative motion of the screw and edge dislocations [7,8,132,189], where thermally activated nucleation of kink-pairs plays a crucial role on the motion of screw dislocations. Thus, relatively low activation volumes have been observed between 1 and 9 b^3 for micropillars ranging in diameter from 200 nm to 3 µm [6,97]. At temperatures well below T_c (low mobility of screw dislocations), screw dislocation multiplication is believed to take place while at temperatures close to or above T_c, dislocation annihilation occurs at the free surface so that surface dislocation nucleation may control its deformation, as for FCC metals [132]. In view of these observations and assuming that the mobilities of screw and edge dislocations are similar for β-CuZn at room temperature, the small activation volume values for the 200 nm diameter pillars suggest that surface dislocation nucleation (kink-assisted), a thermally activated process [175,182,207], may govern the room temperature plastic deformation of β-CuZn in the sub-micron regime.

From the plasticity point of view, β-CuZn has been shown to hold an intermediate position between BCC and FCC metals. Its slip behavior is similar to that of BCC metals.

However, the size dependence of the yield stress is more typical of FCC metals, where the mobility of screw and edge dislocations is comparable. Questions still arise regarding the origin of the orientation dependence of the CRSS as a function of size, i.e., whether this is due to ion damage promoting a change in dislocation core structure or whether this is an inherent change promoted by surface effects favoring deformation in certain crystallographic orientations.

5.5 Conclusions

Plasticity in β-CuZn was studied in micropillars as a function of sample size and crystal orientation. The following conclusions can be drawn:

- All compressed pillars except the smallest ones exhibited a characteristic 'S' shape. This shape is believed to be caused by the activation of multiple slip systems, with traces corresponding to ⟨111⟩{110} and ⟨111⟩{112}. Furthermore, EBSD and TEM analyses provided no evidence of either kinking or stress induced phase transformation or deformation twinning.
- The yield strength showed a size dependence similar in magnitude to that of FCC pillars. All crystal orientations exhibited similar size dependences with power-law exponents ranging from -0.54 to -0.65. As the test temperature was above the critical temperature, screw and edge dislocations can be assumed to have similar mobility.
- All pillars, irrespective of size, exhibited a jerky flow behavior which is normally typical only of sub-micron sized pillars. This might be related to a dislocation locking mechanism that has also been observed in bulk β-CuZn.
- Constant strain rate tests showed that the strain rate sensitivity increased with decreasing specimen size and was considerably lower than for FCC and BCC pillars. This is in agreement with the observed jerky flow since a common feature of such behavior for different bulk materials is low strain rate sensitivity.
- A change from ⟨111⟩{110} to ⟨111⟩{112} seemed to take place as sample size decreased down to the sub-micron regime. This change might be connected to surface dislocation nucleation taking place at the sub-micron regime. Concerns arise from it, where gallium ion damage might induce such changes.

6 Size effects in NiAl micropillars and their crystal orientation dependence

Effects of specimen size on strength arise in confined geometries at the (sub-) micron scale. In single-crystalline FCC and BCC metals, these have been consistently shown to depend strongly on the nucleation and motion of dislocations. However, the influence of dislocations on the size effect in ordered structures such as B2 alloys is barely explored. In this work, we study the effects of sample size and crystal orientation on the compressive behavior of NiAl single crystal micropillars at room temperature. NiAl, a highly ordered B2 intermetallic, exhibits high and low lattice friction depending on crystal orientation, thus being a good candidate for studying the influence of such a parameter on size effects. The results show a strong crystal orientation dependence of the size effect as well as a four-fold increase in ductility compared to bulk NiAl single crystals. These findings are discussed with regard to the lattice friction and screw dislocation mobility dependence. Furthermore, we show that differences in yield strength with crystal orientation vanish with decreasing sample size down to 200 nm in diameter. Such a reduction is ascribed to surface effects and dislocation-source controlled deformation.

6.1 Introduction

Intermetallic compounds that possess a B2 structure deform by slip either along the ⟨111⟩ crystallographic direction, typical of body-centered cubic (BCC) metals, or along the ⟨001⟩ direction, in line with the slip direction in ionic materials [56]. The preferred slip direction is dictated by a combination of elastic anisotropy, motion of stacking-fault-like defects and energies of these defects [37]. B2 compounds that show the ⟨111⟩ slip direction are ductile [39]. On the contrary, in B2 alloys with preferred slip vectors in the ⟨100⟩ direction such as NiAl, only three independent slip systems are available, and therefore the von Mises criterion for polycrystalline ductility is not satisfied [39,208].

The B2 compound NiAl possesses high strength, rather low specific density, good oxidation resistance and high stability under heavy ion bombardment conditions [208,209]. These properties have made this intermetallic very attractive for high-temperature technological applications, particularly for nuclear applications. However, its semi-brittle behavior at room temperature has strongly limited its use [208]. Single-crystal NiAl shows limited plastic flow in compression before failure [34–36,64–66], strongly dependent on the loading orientation. For instance, stoichiometric single crystals reach maximum strain levels between 3 and 23% at room temperature [35,65,67,69,76,210]. This disparity in ductility depending on crystal orientation has been ascribed to the high plastic anisotropy of this material, i.e., large difference in critical resolved shear stress on different slip systems (in contrast to classical Schmid's behavior, which considers that the critical resolved shear stress is constant). On one hand, for non-⟨100⟩-oriented single crystals (soft crystals), slip mainly occurs along ⟨100⟩ directions on {110} planes irrespective of temperature [34,36]. On the other hand, ⟨100⟩ or near ⟨100⟩-oriented single crystals (hard crystals) deform by either conventional slip along the ⟨111⟩ direction on {110} and {112} planes or by a heavily localized deformation process called kinking [33,208]. The reason for this is that all possible slip systems with the ⟨100⟩ slip vector have a Schmid factor of zero. Consequently, other deformation mechanisms have to be activated to accommodate the deformation. Kinking is a mechanism based on the deformation of a single band that takes place on {110} planes in ⟨100⟩ slip directions [33], and has been observed at temperatures up to 773 K in NiAl [64,68,75]. The conditions under which conventional slip or kinking occur are still being debated.

Deformation has been described as the balance between ⟨100⟩ and ⟨111⟩ slip [66] and is believed to be related to crystallographic misalignments, the aspect ratio of the compression specimens and the strain rates. Kinking seems to be favored for specimens loaded slightly off the [001] direction, between 3 and 20° [76], with aspect ratios larger than 2.4 [33,77] and at strain rates larger than 10^{-4} s^{-1} [68].

Investigations into the mechanical behavior of metals have consistently shown changes in strength and deformation behavior between micron sized and bulk specimens [104,181,182]. Size effects on strength have been extensively observed in a wide variety of materials, ranging from metals and alloys to ceramics [5,103,104]. This size effect is typically characterized by a power-law relation between yield strength σ_y and pillar diameter d, $\sigma_y \propto d^n$, giving rise to a distinctive exponent n. For instance, a universal power-law exponent n of about -0.6 has been found for face-centered cubic (FCC) single crystals [5]. However, for body-centered cubic (BCC) metal single crystals, the power-law exponent has been observed to scale with the ratio between the test temperature and a critical temperature T_c specific of the BCC metal tested (lattice friction) [7]. The origin of this size effect is intimately related to the nucleation, activation and motion of dislocations at the nano-/microscale, which are influenced by an increase of the surface to volume ratio when reducing sample size [85].

Size strengthening effects in B2 intermetallics have barely been investigated. Mainly ductile B2 intermetallics (NiTi and β-CuZn), which deform by ⟨111⟩ slip, have been studied [9–11,211]. For B2 alloys that are inherently brittle, showing ⟨100⟩ slip, little is known about their behavior at small scales. So far, only few studies have dealt with the mechanical behavior of these intermetallic compounds at the microscale [212,213]. Particularly, the anisotropic fracture toughness of NiAl single crystal microbeams was assessed. However, nothing is known about size strengthening effects and size dependent deformation behavior of this material. For instance, it is not known if anisotropy effects are reduced and ductility improved, or if kink banding also occurs at the microscale.

The aim of this work was to improve the understanding of NiAl plastic behavior, particularly in the micron regime. Through the compression of NiAl single crystalline micropillars, the effect of size and crystal orientation on the deformation behavior of NiAl was investigated. Attention was paid to the influence of plastic anisotropy on the size effect, as well as to the occurrence of conventional slip or kinking and to the improvement

in ductility at this size regime. The response to compression is studied by scanning electron microscopy (SEM) and post-mortem transmission electron microscopy (TEM).

6.2 Experimental method

A polycrystalline NiAl sample of stoichiometric composition (Ni- 31 wt% Al) and 99.95% purity was purchased (supplier American Elements, Los Angeles, CA). The sample, with square cross-section, had an edge length of 10 mm and thickness of 5 mm. It was cut in 4 pieces of approximately 5 mm in length and in thickness. Subsequently, the samples were heat treated in an argon atmosphere at 600 °C for about 5 h and furnace-cooled to diminish defect populations and residual stresses. It is assumed that all samples present similar defect populations after heat treatment. A final average grain size of 500 μm was achieved according to the linear intercept method on EBSD images. The specimens were mechanically ground with polishing paper down to an average particle size of 8 μm and subsequently electropolished. The electropolishing was conducted at a voltage of 30 V for 50 s using a commercial solution made of ethanol, 2-butoxyethanol, perchloric acid 60% and water (electrolyte A2I-II, Struers, Willich, Germany). This last polishing step produced a smooth surface and reduced the damage layer created during cutting and grinding. NiAl B2 single phase was confirmed through X-ray diffraction.

EBSD was employed to determine the grain orientation of the samples. Three different grains with average orientations near $[1\bar{2}3]$, $[001]$ and $[1\bar{2}8]$ were selected (see Table 6.1). In these grains, pillar deformation occurred preferentially along either the $\langle 100 \rangle$ or $\langle 111 \rangle$ directions. Furthermore, most studies on bulk NiAl have been carried out with single crystals oriented along the $[001]$ and $[1\bar{2}3]$ directions so that comparisons to their bulk counterparts could be readily made. Single crystalline pillars ranging in diameter from 200 nm to 5 μm and with different aspect ratios (length:diameter 1.5-5) were fabricated within these grains. These micropillars were machined using a dual SEM and focused ion beam (FIB) (FEI Versa 3D DualBeam, Hillsboro, OR). The annular milling technique [9,84,87,189] was employed using a gallium ion beam voltage of 30 kV. First, high milling currents between 30 and 7 nA were used to form coarse pillars within craters, and second, final low currents ranging between 0.5 and 0.01 nA were employed to reduce ion damage on the specimen surface and carefully define the size of the pillars. This milling technique inherently creates slight tapered pillars, with typically larger taper

angles for smaller pillars (see Table A.4 in Appendix I: Taper angle vs. pillar diameter). Efforts were made to keep the taper angles of the different crystal orientations as similar as possible, which ranged from 2,9 ± 0.2 ° for large pillars to 4.6 ± 0.4 ° for small pillars. Consistent with other studies [7,189,211], the stresses experienced during compression were determined using the top pillar diameter. The elastic deformation of the substrate during compression was taken into account when determining strain values. For that, Sneddon's solution [87,157] of a punch pressed into an elastic half-space was used.

All pillars were compressed *in situ* in the dual beam using a Hysitron PI 87 SEM Picoindenter (Minneapolis, MN). The five degrees of freedom in this system allowed precise positioning of the indenter and minimization of contact misalignment. The indenter was equipped with a flat tipped pyramidal indenter made of diamond with a diagonal of 10 µm. Nine pillars per size and crystal orientation with a constant aspect ratio of 3 were compressed to an approximate total strain of 0.15 at a constant stress rate of 30 MPa/s. Maximum strains of up to 85% were reached in some cases due to the strong stochastic stress-strain response. The maximum load and testing time were scaled accordingly depending on the pillar diameter to keep the stress rate constant. The active slip systems were predicted according to Schmid's law.

Since it is expected that kink banding is strongly influenced by strain rate, aspect ratio of the sample and crystallographic misalignment, tests performed at different strain rates ($5\cdot10^{-2}$, $5\cdot10^{-3}$ and $5\cdot10^{-5}$ s^{-1}) were carried out for $[001]$-oriented pillars and the ~15° off-set $[1\bar{2}8]$-oriented pillars with diameters of 200 nm, 2 and 5 µm. Also, pillars with different aspect ratios of 1.5, 3 and 5 were tested at a constant strain rate of $5\cdot10^{-3}$ s^{-1}. A total of four pillars per size and strain rate were tested. To conduct the constant strain rate tests, the displacement rate was scaled according to the initial pillar length.

The deformation morphology of the microspecimens was characterized through SEM and TEM imaging. A TEM lamella was fabricated from a 2 µm diameter pillar oriented along the $[1\bar{2}8]$ crystallographic direction using the dual beam. The fabrication procedure was the same as the one previously employed in Chapter 5. Initially, a 2 µm layer of platinum coating was deposited using ion beam induced deposition. The rationale for this was to protect it from sputtering of the ion beam during lamella fabrication. The pillar was then cut using the FIB to a thickness of approximately 1.5 µm before being transferred to a TEM grid using a micromanipulator within the FIB. The lamella was then thinned to a final thickness of approximately 1 µm first for EBSD purposes and afterwards to

approximately 100 nm for TEM examination. The lamella was argon ion polished to minimize artifacts coming from the gallium ion polishing steps (Nanomill - Fischione Instruments, Export, PA). The thick lamella was scanned at 20 kV and 16 nA with a step size of 20 nm in the dual beam using an EBSD Hikari system (EDAX Ametek, Mahwah, NJ). The thin TEM sample was observed with a JEOL JEM-2100 LaB6 (Tokyo, Japan) operated at 200 kV under bright field imaging conditions and further analyzed using the Energy Dispersive X-Ray Spectroscopy (EDX) technique.

Table 6.1: Crystal orientation of the micropillars and rotation angle with respect to the intended 'ideal' orientation. Also, determined Schmid Factors for slip in either ⟨111⟩{110} or ⟨100⟩{110}, typically observed for bulk NiAl samples.

Grain orientation	Intended grain orientation	Crystal rotation (°)	Slip	Schmid Factor	
				$\langle\mathbf{111}\rangle\{\mathbf{110}\}$	$\langle\mathbf{100}\rangle\{\mathbf{110}\}$
$[6\bar{1}\bar{1}17]$	$[1\bar{2}3]$	1.3	Single slip	0.46	0.46
[1023]	[001]	2.5	Multiple slip	0.43	0.03
$[1\bar{2}8]$	[001]	15.6	Single slip	0.48	0.25

6.3 Results

6.3.1 Deformation morphology

SEM images of compressed micropillars oriented along the $[1\bar{2}3]$, [001] and $[1\bar{2}8]$ directions are shown in Figure 6.1. In this figure, a 0.2 and a 5 µm diameter pillars were chosen as being representative of the deformation behavior of $[1\bar{2}3]$-oriented pillars compressed in this study (Figure 6.1a,b and c) whereas a 0.2 and a 4 µm diameter pillars were chosen for [001]- and $[1\bar{2}8]$-oriented pillars (Figure 6.1d, e, f, g, h and i). Different deformation morphologies can be distinguished: $[1\bar{2}3]$-oriented pillars exhibit mainly one set of slip traces emanating from the top of the pillar, irrespective of pillar size (Figure 6.1a, b and c). These observations reveal the presence of only one independent slip system, as expected from Schmid's law. The slip planes exhibit an angle of approximately 55° with respect to the $(1\bar{2}3)$ plane and can only correspond to $\{110\}$ planes. The slip direction is most likely $\langle 001\rangle$ for such a soft crystal orientation according to TEM studies on bulk NiAl [67,208]. Therefore, the slip traces observed can be a consequence of the $[001](1\bar{1}0)$ slip system, which can be easily activated as a result of a large Schmid factor (0.46). A few 200 nm diameter pillars present an additional slip system formed at relatively large strain levels (over 20% strain, Figure 6.1a). Slip steps are observed on the

pillar surfaces after large deformation strains, as seen in Figure 6.1b and c for a 5 μm diameter pillar compressed up to 22% strain. Fewer slip bands are observed with decreasing sample size, but the existing slip bands seem to be much more active, as observed in Figure 6.1a.

The slip behavior of these micropillars resembles that of FCC and BCC micropillars with a low thermal component to strength when compressed under single-slip conditions [4,83,97]. $[001]$-oriented micropillars show no sign of kink formation. Instead, 200 nm diameter pillars show only single slip (Figure 6.1d) while larger pillars manifest traces characteristic of multiple slip (Figure 6.1e and f). A high magnification image of a 4 μm diameter pillar in Figure 6.1c shows very fine and straight slip traces, suggesting at least two independent slip systems. The slip traces form an angle of about 45° with respect to the (001) plane, indicative of $\{110\}$ planes as expected [67,208]. The slip directions must correspond to $\langle 111 \rangle$ since the Schmid factor for the alternative $\langle 001 \rangle$ directions are nearly zero (~0.03), and thus would require much higher stresses to activate. Therefore, the slip traces observed most certainly correspond to the $[1\bar{1}1](011)$ and $[111](01\bar{1})$ slip systems, which exhibit the largest Schmid factor (~0.43) and are expected to show an angle of about 45° with respect to the $[001]$ crystal orientation. Interestingly, compared to the $[1\bar{2}3]$-oriented pillars, the slip traces observed for the $[001]$-oriented pillars are much finer (Figure 6.1c and f). Similar fine slip traces have been previously observed for another B2 intermetallic, β-CuZn, and have been attributed to $\langle 111 \rangle\{110\}$ slip [211].

Micropillars compressed along the $[1\bar{2}8]$ direction, i.e., 15.6° away from the $[001]$ direction, illustrate very different deformation morphologies with changing specimen size. Small pillars, about 200 nm in diameter, exhibit one distinct slip step (Figure 6.1g). Larger pillars, however, were suddenly deformed by apparent bending/buckling once a certain stress was reached (Figure 6.1h and i). This produced the fracture of several specimens at the bottom as seen in Figure 6.1i for a 4 μm diameter pillar compressed up to 65% strain. Even if the pillars were heavily deformed, no slip traces are observed on the pillar surfaces apart from those caused by the sudden plastic instability. It must be noted that this effect occurred although special care was taken to minimize contact misalignments between the pillar top and the flat punch. Limited plastic deformation occurred prior to the sudden deformation of the micropillars.

It must be noted that all 200 nm diameter pillars exhibit clear distinctive slip steps regardless of crystal orientation, indicating a difference in the deformation mechanism compared to the larger micropillars.

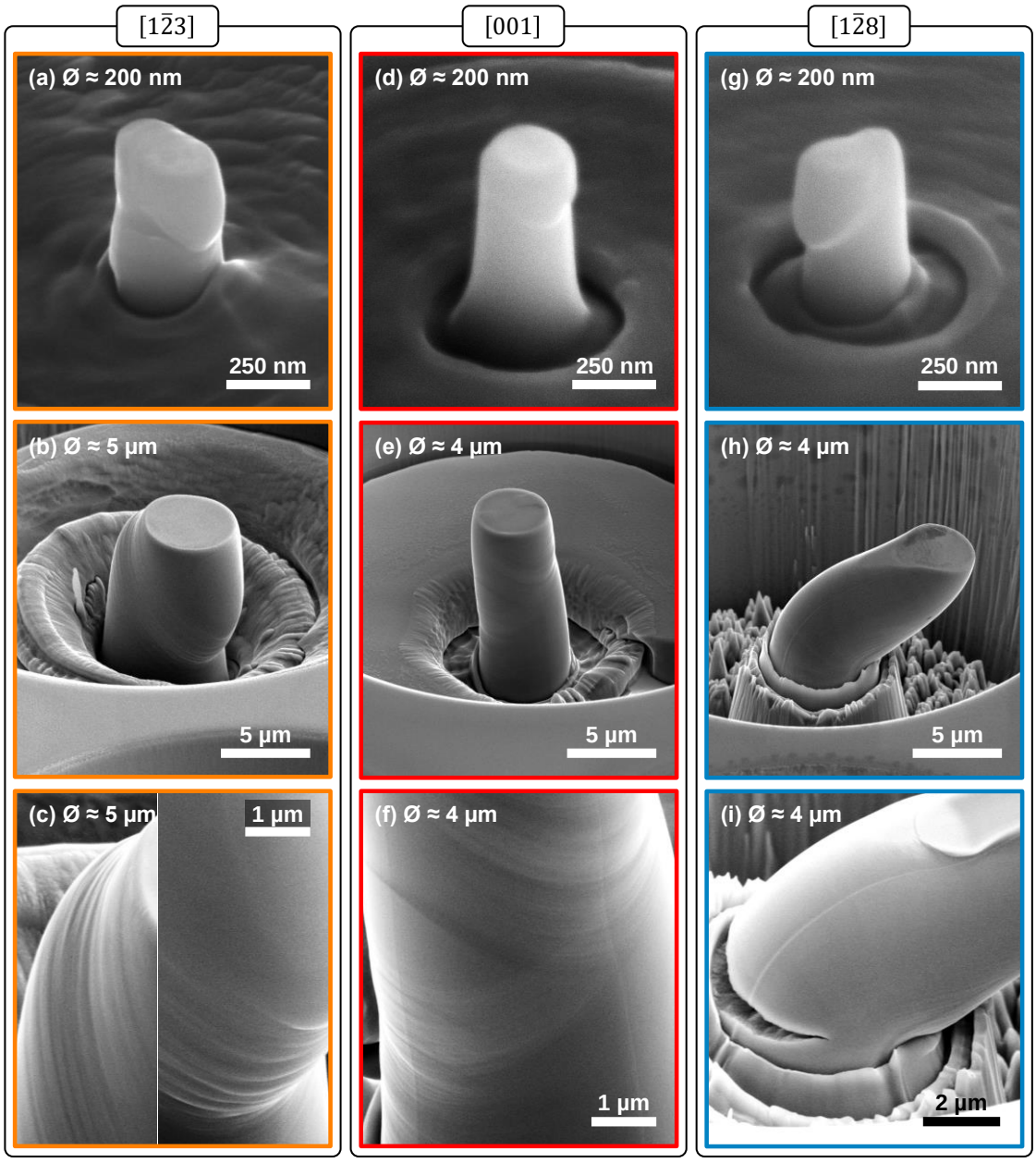

Figure 6.1: SEM images of compressed pillars oriented along the (a-c) [1$\bar{2}$3], (d-f) [001] and (g-i) [1$\bar{2}$8] directions. Small pillars of approximately 200 nm in diameter are shown in (a), (d) and (g). Higher resolution images of (c) a [1$\bar{2}$3]-oriented 5 µm pillar, (f) a [001]-oriented 4 µm diameter pillar and (i) a [1$\bar{2}$8]-oriented 4 µm diameter pillar exhibit the characteristic deformation features of large pillars.

6.3.2 Stress-strain response

Characteristic strain-stress curves of compressed micropillars with diameters between 0.2 and 5 µm are depicted in Figure 6.2. All pillars tested show some common features irrespective of crystal orientation. The pillars first experience elastic loading until a certain stress is attained, above which a significant deviation from linearity takes place. Pillars smaller than 1 µm in diameter exhibit strain bursts, as commonly observed in load-controlled micropillar compression and associated with dislocation activity [79,82,214]. Larger pillars show rather continuous stress-strain curves as typically found for micropillars of a few micrometers [5,103,104]. Some micropillars exhibit a sudden increase in strain hardening at large strain levels (see 1 and 2 µm diameter pillars in Figure 6.2a above 35% strain). This is because the contact area between the flat punch and the pillar increased at high deformation levels, thus producing an apparent increase in strain hardening. The deformation behavior of $[1\bar{2}3]$-oriented micropillars is rather continuous as denoted by the stress-strain curves in Figure 6.2a except in some rare cases where sudden long strain bursts take place (see 3 µm diameter pillar in Figure 6.2a). Plastic deformation of $[001]$- and $[1\bar{2}8]$-oriented micropillars, however, differs in that large strain bursts occur irrespective of sample size (Figure 6.2b and c). Such long strain bursts are typically caused by the sudden activation of dislocation sources in metals. Since these measurements were performed at constant stress rate up to a predefined maximum stress, large strain levels (up to 65%) were reached (Figure 6.2c). The insets in Figure 6.2 are close-up images of the elastic loading part of the different curves. They show that, sometimes, slight contact misalignments between the flat punch and the top of the pillar existed during loading.

Remarkable are the very large strain values (65-85%) reached before failure compared to their bulk counterparts. Commonly, bulk stoichiometric NiAl single crystals are semi-brittle, experiencing limited deformation with maximum strain values of up to 23% at room temperature [35,65,67,69,76,210].

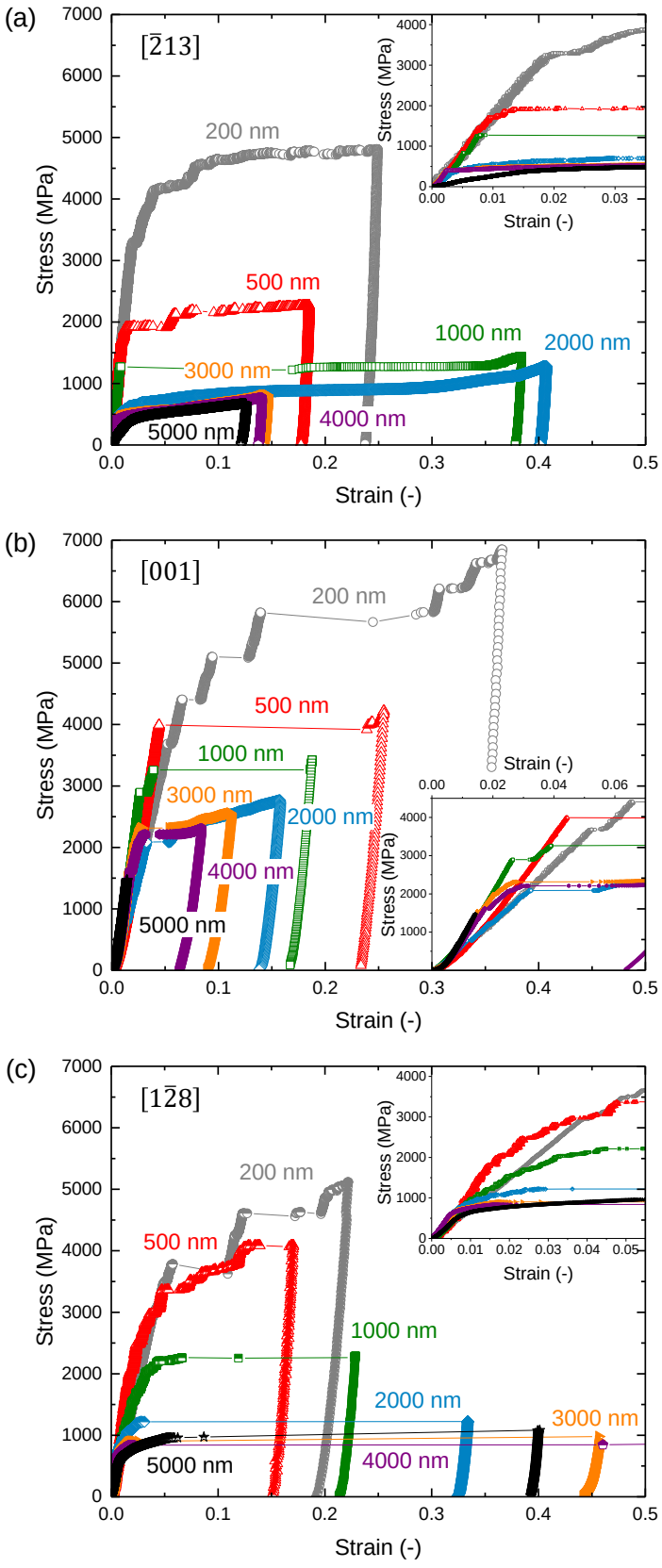

Figure 6.2: Characteristic stress-strain curves of (a) [1$\bar{2}$3]-, (b) [001]- and (c) [1$\bar{2}$8]-oriented pillars with diameters ranging between 0.2 and 5 µm. The insets show the initial loading part of the curves, where it is evident the different apparent stiffness of the pillars caused by contact misalignments (slope of the elastic loading part).

To exactly determine how $[1\bar{2}8]$-oriented micropillars deform in compression, several micropillars were compressed at different strain rates ($5\cdot10^{-2}$, $5\cdot10^{-3}$ and $5\cdot10^{-5}$ s^{-1}). Figure 6.3 shows representative stress-strain curves of 2 and 5 μm diameter pillars compressed along the $[1\bar{2}8]$ axis. After initial elastic loading, pillars compressed at high strain rates ($5\cdot10^{-2}$ s^{-1}) harden until a critical stress is reached, from which a sudden strain burst takes place, as observed previously for the pillars compressed at a constant stress rate of 30 MPa/s. On the contrary, pillars tested at the smaller strain rates of $5\cdot10^{-3}$ and $5\cdot10^{-5}$ s^{-1} exhibit a distinct softening after an initial strain hardening stage. In a few cases, pillars tested at $5\cdot10^{-3}$ s^{-1} strain rate also exhibited a similar behavior to those compressed at a faster $5\cdot10^{-2}$ s^{-1} strain rate. Since these pillars were tested at constant strain rate, any plastic event is usually attenuated by producing a stress drop and shortening of a strain burst. This was the case for the pillars compressed at the low $5\cdot10^{-3}$ and $5\cdot10^{-5}$ s^{-1} strain rates. However, for the pillars compressed at $5\cdot10^{-2}$ s^{-1}, the imposed deformation rate was too fast so that no softening is observed.

In addition, a 2 μm diameter pillar was compressed at low strain rate up to 60% strain, and this showed no relevant difference in deformation morphology with respect to the ones compressed at high strain rates (not shown here). Thus, it is apparent that there is no major difference in deformation morphology between the pillars compressed at high and low strain rates. The difference in stress-strain response stems from the difference in imposed deformation rate, thus causing softening at low strain rates and sudden yielding up to high strains at high enough strain rates.

As evidenced in Figure 6.3, most $[1\bar{2}8]$-oriented pillars exhibit a distinct deformation mark at the bottom part of the pillar (see dashed line in micrograph 3), where most deformation seems to take place. This is further observed in Figure 6.4, which captures the deformation features of a 2 μm diameter pillar compressed along the $[1\bar{2}8]$ loading axis up to a total strain of 15% at a strain rate of $5\cdot10^{-5}$ s^{-1} (pillar number 4 in Figure 6.3). The EBSD map shown in Figure 6.4a evidences that the core of the pillar is rotated with respect to the top and base of the pillar, where two distinct bands are observed. This is better seen in Figure 6.4b, where the misorientation of the pillar with respect to the undeformed substrate is mapped from an EBSD scan of the pillar. In this figure, it is observed that the pillar top and base undergo no deformation while the core of the pillar is rotated by up to 27° (red area). Figure 6.4c is a local misorientation map (kernel average misorientation). Two highly misoriented bands are observed (red regions in Figure 6.4c). This emphasizes that plastic deformation up to 15% strain was highly localized in these

two areas, leaving the core of the pillar almost undeformed. The surrounding area of the pillar in Figure 6.4 is an artifact stemming from the protective Pt layer deposited on the specimen. Interestingly, a bright field TEM image of this lamella shows that most of the deformation was localized at the bottom part of the pillar (Figure 6.5). This is manifested by the presence of a high density of dislocations as well as a clear boundary at which dislocations appear to pile up (noted by arrows in Figure 6.5). Few dislocations were observed in the core of the pillar compared to the bottom part. This image also shows the pile-up of many dislocations near the pillar top, which might be caused by stress concentrations resulting from friction between the pillar and the flat punch. The upper inset in Figure 6.5 shows the damage layer produced by the FIB, which is about 20 nm thick. The bottom inset shows a thicker damage layer of approximately 40 nm near the substrate, where the sample was exposed to much higher gallium ion beam currents.

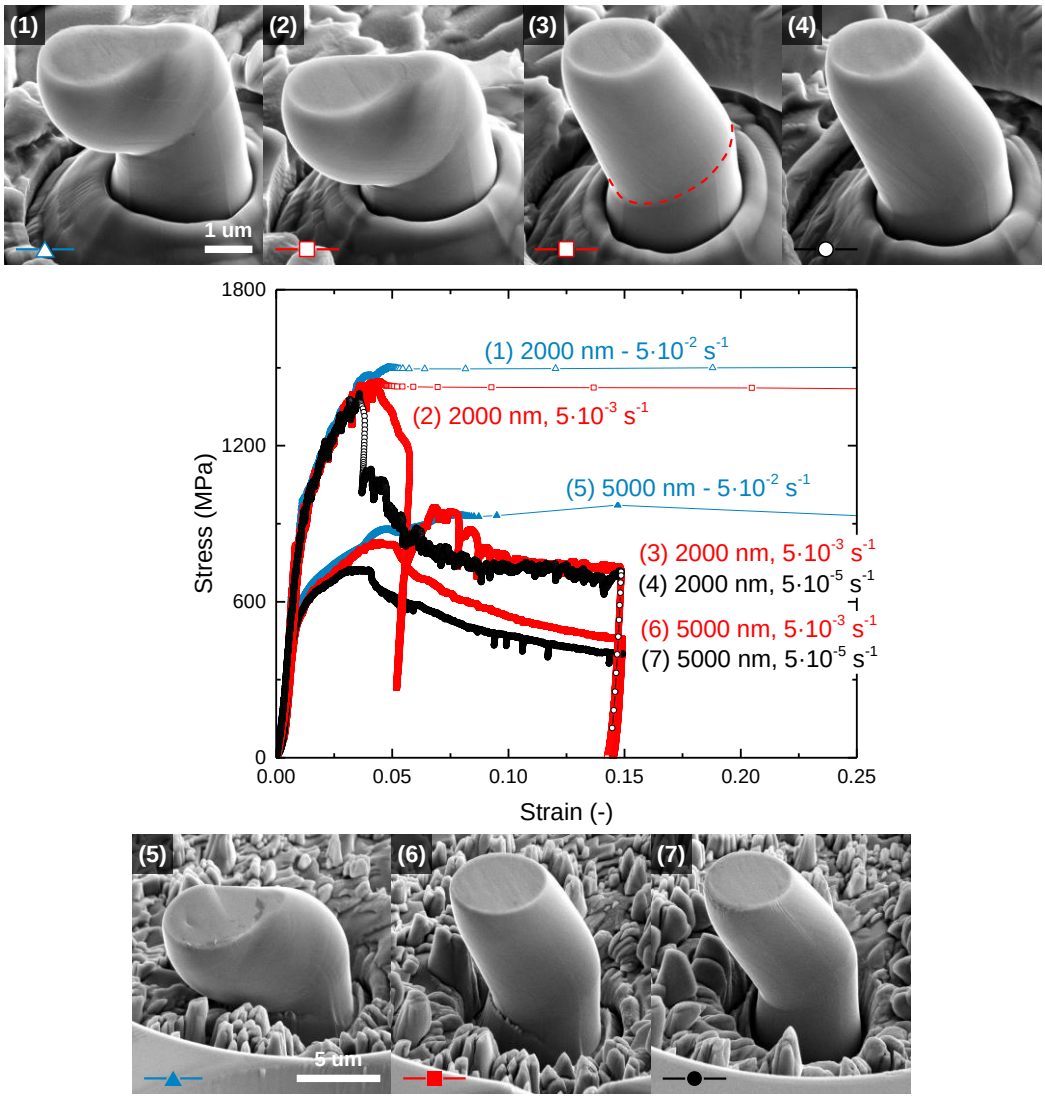

Figure 6.3: Stress-strain curves of (1-4) 2 and (5-7) 5 µm diameter pillars loaded at strain rates of $5\cdot10^{-2}$, $5\cdot10^{-3}$ and $5\cdot10^{-5}$ s^{-1} along the $[1\bar{2}8]$ axis and their corresponding SEM images after compression.

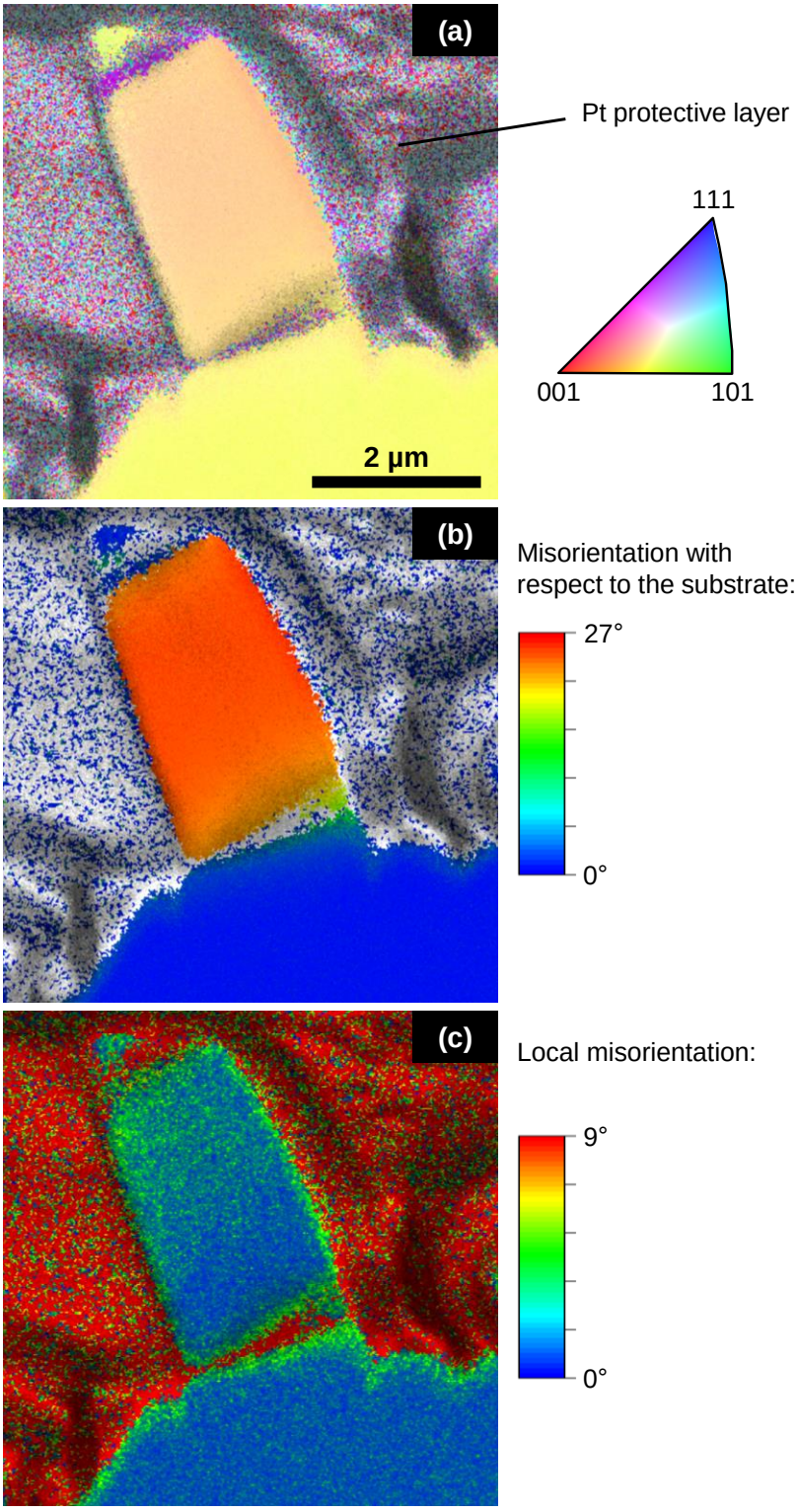

Figure 6.4: Crystal orientation and deformation maps of a thick lamella cut out of a 2 µm diameter pillar compressed up to 15% strain at $5 \cdot 10^{-5}$ s^{-1}. (a) EBSD map, (b) global misorientation map with respect to the undeformed substrate and (c) local misorientation map (kernel average misorientation map). The scan was performed with a step size of 20 nm. (a) shows the crystal orientation throughout the pillars based on the (001) pole figure map. The background grey images correspond to the image quality map of the lamella. Dark areas correspond to bad quality (Pt protective layer). An SEM image as well as the stress-strain curve of this pillar can be seen in Figure 6.3 (pillar number 4).

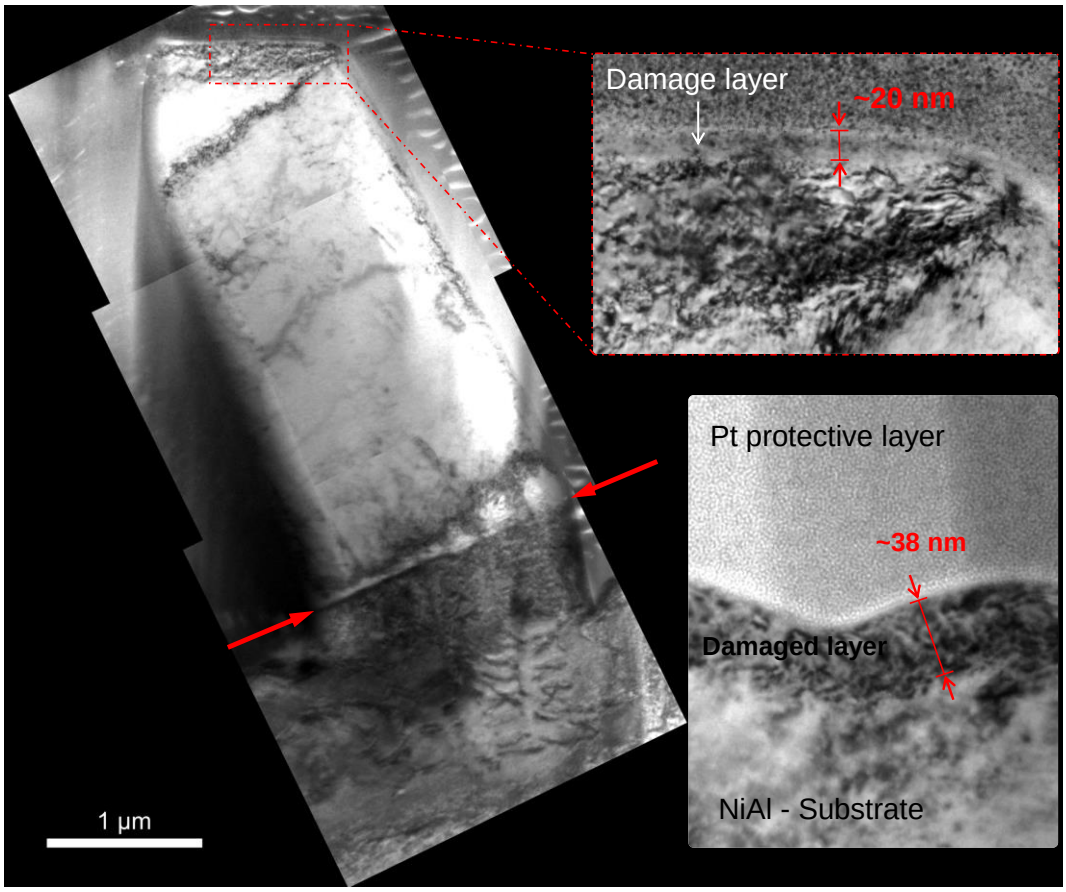

Figure 6.5: Bright field imaging micrograph of a TEM lamella cut out of a 2 µm diameter pillar compressed up to 15% strain at $5 \cdot 10^{-5}$ s^{-1} (corresponding to pillar number 4 in Figure 6.3). Deformation took place mainly on a distinct band at the bottom at the pillar, where a high dislocation density is observed. Also, dislocations seem to pile up on the top region of the pillar: on a shear band as well as at the interface between the pillar top and the flat punch. A distinctive boundary where dislocations appear to accumulate is highlighted by arrows.

6.3.3 Size effect

Due to the very high yield strength values of small pillars and some contact misalignment, elastic loading of some compressed pillars extend up to 4% strain. Thus, the size dependent plastic strength of NiAl pillars had to be determined using flow stress values above 4% strain. Figure 6.6a illustrates the critical resolved shear stress (CRSS) at 5% total strain against pillar diameter for the different crystal orientations. The procedure used to calculate *n* is the same as the one presented in [189]. From Figure 6.6b, it can be observed that the power-law exponents *n* of the different crystal orientations are considerably affected by strain up to approximately 5%, from which point they remain relatively constant. Of particular interest is the strong crystallographic orientation dependence of *n* observed in Figure 6.6: $[1\bar{2}3]$- and $[1\bar{2}8]$-oriented pillars show a similar power-law exponent *n* of -0.62 ± 0.02 and -0.56 ± 0.03 whereas [001] -oriented micropillars show a much smaller size effect: -0.27 ± 0.02. This strong disparity in size

effects between soft and hard crystal orientations has been previously reported for other materials with a high plastic anisotropy, such as MgO and LiF [138,215]. Bulk shear strength values for hard and soft crystal orientations are illustrated for comparison [33,76] in Figure 6.6a. Correlation between bulk and micropillar results must be carried out with caution as the stress-strain response of NiAl will be affected by defect density and impurity concentration [33,39,208]. Interestingly, Figure 6.6a indicates a clear decrease in plastic anisotropy with decreasing sample size, with similar strength values of 200 nm diameter pillars regardless of crystal orientation.

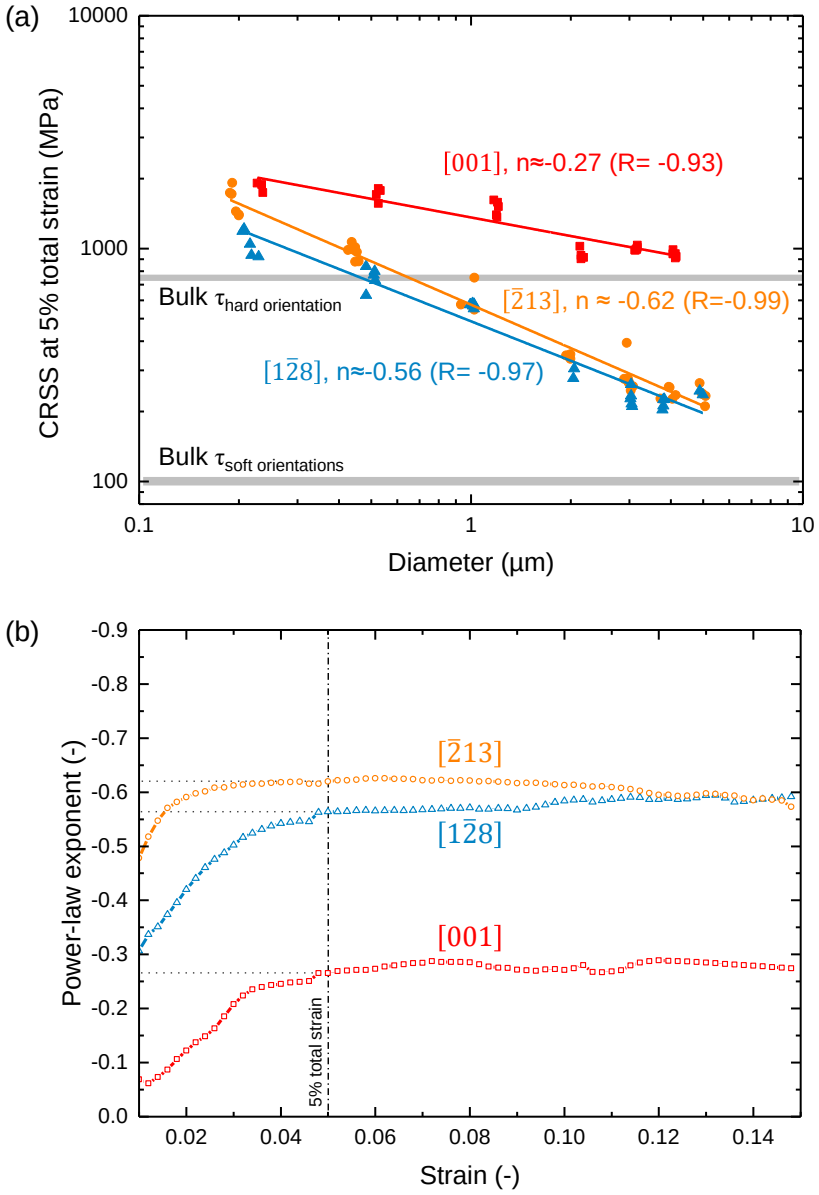

Figure 6.6: (a) Flow stress at 5% total strain against pillar diameter for [1$\bar{2}$3]-, [001]- and [1$\bar{2}$8]-oriented pillars. (b) Size effect as a function of strain level (yield criterion) for the [1$\bar{2}$3]-, [001]- and [1$\bar{2}$8]-oriented pillars. Bulk yield strength ranges indicated in (a) are taken from references [33,76].

6.4 Discussion

To study the size and crystal orientation dependence of plastic strength in NiAl, FIB manufactured single-crystalline pillars ranging in diameter from 0.2 to 5 µm have been tested in compression at room temperature. Three distinct characteristics were observed in comparison to better-studied FCC and BCC metals. First, deformation morphology was a function of crystal orientation and particularly size. Second, high ductility was experienced irrespective of crystal orientation compared to the limited ductility shown by bulk NiAl specimens. Last, the size effect was clearly crystal orientation dependent, exhibiting high FCC-like size dependence (~ -0.6) for soft crystals and much lower size dependence (-0.27) for the hard crystal.

6.4.1 Deformation mechanisms as a function of crystal orientation and size

Deformation morphology was a function of crystal orientation, which is caused by the activation of different slip systems depending on crystal orientation. $[1\bar{2}3]$-oriented pillars showed deformation characteristic of single slip pillars ($[001](1\bar{1}0)$ slip) and exhibited clearly defined slip steps regardless of specimen size. This deformation feature resembles that of FCC and BCC micropillars [4,83,97] with a low thermal component to the strength at room temperature. In this case, FCC and BCC micropillars have a rather planar dislocation core structure, and thus slip is confined to specific crystallographic planes [165].

By contrast, $[001]$-oriented pillars showed multiple fine slip traces resembling those observed in another B2 intermetallic, β-CuZn, which typically deforms by $\langle 111\rangle\{110\}$ [211]. These results agree with our expectations since, for this orientation, all possible $\langle 100\rangle\{110\}$ slip systems have a Schmid factor of zero. Thus, the alternative $\langle 111\rangle\{110\}$ slip system, commonly shown by other B2 intermetallics, is activated [33,76].

$[1\bar{2}8]$ -oriented pillars showed a characteristic plastic instability, i.e., sudden buckling/bending. Such a deformation mechanism does not appear to be caused by contact misalignments, which were carefully minimized: using indentations in the vicinity of the pillars, the load-displacement curves and indentation prints were analyzed. The fact that the elastic loading and unloading part of the curves in Figure 6.3 are very similar confirms that the deformation behavior is not a consequence of contact

misalignment. The existence of such plastic deformation, therefore, may be ascribed to misalignments in the crystal orientation, i.e., crystal rotation with respect to the [001] orientation, as also found for highly anisotropic LiF [171,215]. Soler *et al.* [171,215] observed similar deformation mechanisms and associated this plastic behavior with the high plastic anisotropy of the material. They compared experimental results with finite element simulations of LiF micropillar compression experiments. The large plastic anisotropy was attributed to the very different properties of hard and soft slip systems. Furthermore, they showed that highly plastically anisotropic materials are considerably more susceptible to pillar misalignments than plastically isotropic materials such as FCC and BCC metals. In view of this hypothesis, bulk NiAl exhibits a marked plastic anisotropy as a consequence of the two distinct slip systems responsible for single crystal deformation: ⟨100⟩{110} cube slip and ⟨111⟩{110} diagonal slip [33,76].

It appears, then, that the observed plastic instability in $[1\bar{2}8]$-oriented pillars may be the result of the sudden activation of cube slip systems after reaching a certain load, which is possibly favored by a first elastic bending of the pillars. This plastic instability may be the commonly observed in bulk specimens oriented along hard orientations, i.e., kinking. This is manifested in our micropillars as a deformation band in the plane of maximum shear stress (see Figure 6.5), after a limited amount of plastic straining (see Figure 6.2c). Also, some specimens exhibited cracks at the bottom of the pillars after a possible formation of a kink band (see Figure 6.1i). All these deformation features have been previously described for bulk NiAl specimens loaded between 3 and 20° away from the [001] axis [67,76]. Uniform deformation of these hard oriented specimens by the glide of ⟨111⟩ or ⟨100⟩ dislocations results in a rotation of the specimen axis away from [100], and kinking may therefore be expected after some amount of uniform deformation [67,76]. Although it has been postulated that the occurrence of kinking is associated with strain rate and specimen aspect ratio [66], in our experiments, no difference in deformation mechanism has been observed as a function of these two parameters (see Figure 6.3). The results indicate that kinking is not a deformation mechanism that takes place only at the macroscale, but also at the micron regime.

Interestingly, in the case of the 200 nm diameter pillars, the plastic deformation took place in clear slip steps regardless of crystal orientation, showing noticeable differences in deformation morphology with respect to the larger counterparts for [001]- and $[1\bar{2}8]$-oriented pillars (see Figure 6.1). In general, for pillars in the nanometer regime, plastic deformation occurs by dislocation nucleation preferentially at the free surface [85,216],

and the weakest dislocation source is the one which actually dominates the plastic deformation [202]. Thus, less favorable slip systems may be activated at such size scale. In addition, FIB damage might contribute to the activation of dislocations on less favorable slip systems. It has been shown that microalloying NiAl with Ga causes changes in the deformation behavior of bulk single crystals [217]. Although changes in the slip system have not been observed [217], changes in the dislocation core may limit cross-slip and confine slip in particular slip planes [218]. This might explain why the small 200 nm diameter pillars oriented along the [001] and [1$\bar{2}$8] directions exhibit slip on defined slip planes.

6.4.2 Compression ductility

A striking feature of our current results is the high ductility experienced irrespective of crystal orientation; very high strain levels of up to 85% were reached before fracture took place. Of particular interest are the micropillars compressed along the [001] and [1$\bar{2}$8] axis since compression of 'hard' bulk single crystals has consistently shown considerably lower ductility levels, reaching maximum values between 3 and 16% strain [67,69,210]. Different hypotheses may explain such an increase in ductility. On the one hand, it has been observed that surface oxidation can strongly affect the deformation behavior of bulk NiAl single crystals, reaching ductility values several times higher than unoxidized samples [210]. Such improvement in ductility is related to surface softening, a phenomenon based on the nucleation of mobile edge dislocations at the oxide/metal interface. For our study, we can rule out surface oxidation since the pillars were never exposed to environmental conditions (vacuum of approximately $5 \cdot 10^{-6}$ mbar). On the other hand, the ductility of NiAl is very sensitive to material composition [67], exhibiting a maximum for stoichiometric NiAl. Furthermore, microalloying of NiAl with Ga has shown that tensile ductility may be improved for [110]-oriented specimens [217]. This could explain the increased ductility in our micropillars since our micropillars were manufactured with a focused Ga ion beam. Bright field imaging and EDX analysis of a TEM lamella made out of a compressed 2 µm diameter pillar evidenced the presence of a FIB damage layer of about 20 nm thick where traces of Ga were detected on the pillar surface (see Figure 6.5). Previous investigations for other metals such as Cu [150] and Ni [82] have also shown the formation of a damage layer including dislocation networks that might influence the deformation behavior of micropillars. The exact phenomenon responsible for such improvement in room temperature ductility of NiAl bulk single

crystals has not been elucidated yet. Microalloying with Ga has not been shown to change the main slip system in NiAl. Researchers have suggested that such ductility improvement may be due to a change in the dislocation core structure, thus altering the dislocation mobility, Peierls stress and thermally activated mechanisms [217]. However, our current results seem to disagree with this since the experienced differences in size effects as a function of crystal orientation indicate that screw dislocation mobility may be limited in the case of [001]-oriented micropillars, as further discussed in the next section. Another possible explanation for such high ductility may stem from the fact that the deformation of FIB manufactured micropillars is dominated by the activation of dislocation sources coming from the FIB (surface effects) rather than by conventional dislocation-dislocation interactions as for bulk materials [135], and the inability to build up stresses by sessile dislocation networks. A study on FIB-machined molybdenum (Mo) BCC micropillars showed that pre-straining and re-cutting of Mo pillars does not influence their mechanical response, thus indicating that the dislocation sources produced by the FIB are the ones driving the deformation of these micropillars [135]. Furthermore, a very recent study on high pressure torsion deformation of NiAl has proposed that the limited ductility observed in hard bulk single crystals is a direct consequence of internal stresses built up by sessile dislocation networks, generating deformation induced embrittlement [219]. Since dislocation-dislocation interactions are then not the main factor for deformation at this size regime, the activation of dislocation sources and their exhaustion may lead to the deformation of the material without consequent embrittlement in contrast to bulk NiAl. Thus, micropillars exhibit larger ductility levels.

6.4.3 Size effects: plastic anisotropy

The stress-strain behavior of the NiAl micropillars showed a clear crystal orientation dependence of the size effect, where *n* ranged from -0.62 for $[1\bar{2}3]$-oriented micropillars to -0.27 for [001]-oriented micropillars. This is a manifestation of the plastic anisotropy of NiAl, i.e., difference between critical shear stresses resolved on either cube or diagonal slip systems, which seems to decrease with decreasing sample size (see Figure 6.6: a).

In general, the magnitude of the size effect depends strongly on the yield strength of the bulk material as first suggested by Korte and Clegg [138]. They tested MgO micropillars with a marked plastic anisotropy and pointed out that differences in bulk yield strength of the different pillars could lead to changes in the size effect: larger bulk yield strength

values would diminish the size effect. This reduction can be explained since the size exponent n is the result of the relative contributions of bulk stresses σ_{bulk} and size-dependent stresses $\sigma_{size\text{-}dependent}$ as demonstrated by Soler *et al.* [146] and Torrents Abad *et al.* [189], who systematically altered σ_{bulk} by changing the test temperature:

$$\sigma_y = \sigma_{bulk} + \sigma_{size\ dependent} = B \cdot d^n \qquad \text{Equation 6.1}$$

The bulk stress of a crystalline material is strongly dependent on the lattice friction, shear modulus and dislocation density [142]. It can be treated as the linear superposition of the lattice resistance τ_0/S and a Taylor-like hardening factor including the initial dislocation density ρ_{tot}, shear modulus μ, Burgers vector b and Schmid factor S [113,142]:

$$\sigma_{bulk} \cong \frac{\tau_0}{S} + \frac{0.5\mu b}{S}\sqrt{\rho_{tot}} \qquad \text{Equation 6.2}$$

Thus, if the dislocation density ρ_{tot} does not change drastically, the main parameter dictating the size dependence is the lattice resistance. For metals commonly known to present low lattice resistance at room temperature and hence low size independent bulk yield strengths σ_{bulk}, such as FCC metals, a pronounced size dependence is then observed (low power-law exponent n) on the order of -0.6 (for reviews see, for example, refs. [103,104,127]). On the contrary, other metals such as BCC metals have shown scalable size effects ranging between -0.76 and -0.21 at room temperature as a result of different effective lattice resistance values [7]. These were rationalized in terms of a temperature ratio indicative of the mobility of screw dislocations (magnitude of the lattice friction of the BCC metal at the testing temperature) [7,189], suggesting that the mobility of screw dislocations was the dictating mechanism for experiencing different size effects in BCC metals. The mobility of screw dislocations in BCC metals is associated with the core structure of the dislocations, which are non-planar and thus can present high lattice friction at low temperatures [165]. Similarly, we can explain the crystal orientation dependence of NiAl size effects by assessing the screw dislocation mobility: TEM studies and atomistic computer simulations of $\langle 100 \rangle$ screw dislocations on $\{110\}$ planes conclude that the core structure of $\langle 100 \rangle$ screw dislocations is planar with low Peierls stresses [67,220,221]. Hence, specimens loaded along soft directions would be expected to exhibit a strong size dependence. This is then consistent with our results for $[1\bar{2}3]$-and $[1\bar{2}8]$-oriented micropillars, where $\langle 100 \rangle \{110\}$ slip takes place and and strong size dependences in strength are reached (n values in the range of -0.6).

By contrast, NiAl single crystals compressed along the [001] axis have been shown to deform by ⟨111⟩{110} slip (see Figure 6.1d,e and f) as observed for bulk NiAl [65,208]. Atomistic computer simulations have indicated that the core structure of ⟨111⟩ screw dislocations is non-planar, in a similar way as in BCC metals [221]. The dislocation core is spread on three {110} planes, hence displaying high Peierls stresses and low mobility compared to edge dislocations. This diminishes size effects in [001]-oriented NiAl micropillars, as was commonly observed for BCC micropillars at low temperatures [7,189].

A different hypothesis may explain the observed strong decrease in plastic anisotropy with decreasing sample size. As mentioned above in section 6.4.1, it is believed that the plastic deformation and hence strength of a specimen becomes dislocation-nucleation controlled (in lieu of dislocation-dislocation interaction controlled) as sample size decreases [85,216]. For large samples, dislocation sources are usually abundant and activated when a critical resolved shear stress is attained. However, for samples in the sub-micron regime, dislocations sources are limited, so dislocations have to be first nucleated. It is then expected that the weakest dislocation source, i.e., easiest to activate, is the one that controls the plastic deformation [202] at the sub-micron regime. This might not necessarily be taking place in the most favorable slip system as expected from Schmid's law. Thus, plastic anisotropy might be considerably reduced for the smallest pillars. In addition, it has been proposed for BCC micropillars that surface assisted kink-pair dislocation nucleation may improve screw dislocation mobility [136]. This would imply, for our NiAl sub-micron pillars, that the intrinsic lattice resistance is more easily overcome so that differences in strength between soft and hard oriented pillars decrease as shown in Figure 6.6a.

In summary, NiAl has a size scale dependence on strength characteristic of highly plastic anisotropic materials [138,215], where very different power-law exponents *n* are observed at room temperature. The origin of the different *n* with crystal orientation lies in the activation of different slip systems, and in turn, in differences in the lattice friction with crystal orientation, which strongly changes the size independent bulk strength of the specimens. The underlying physical mechanism responsible for the different size effects as a function of crystal orientation in NiAl micropillars appears to be the mobility of screw dislocations, similarly to BCC metals [7,165,189]. On the other hand, the origin of

the four-fold increase in ductility of NiAl micropillars (in comparison to their bulk counterparts) might come from a combination of different factors. However, there are indications that such large ductility is mainly due to the activation of dislocation sources and limited dislocation-dislocation interactions.

6.5 Conclusions

We studied the compressive behavior of single crystalline NiAl micropillars at room temperature in order to determine the impact of sample size on the plastic behavior of such a semi-brittle material. Overall, more than 200 pillars with different crystal orientations and aspect ratios were tested at different compression rates. The following was found:

- The $[1\bar{2}3]$-, $[001]$- and $[1\bar{2}8]$-oriented micropillars exhibited very different plastic response as a consequence of the activation of different slip systems: $\langle 111\rangle\{110\}$ for $[001]$-oriented micropillars and $\langle 100\rangle\{110\}$ $[1\bar{2}3]$- and $[1\bar{2}8]$-oriented micropillars.
- In contrast to larger pillars, 200 nm diameter pillars deformed in broad and well-defined slip steps irrespective of crystal orientation. This might be caused by surface dislocation source activation promoted at this small size scale.
- Constant strain rate tests on pillars with different aspect ratios compressed along the $[001]$ and $[1\bar{2}8]$ axes showed that kinking also takes place at the microscale as a result of crystal misorientation; $[001]$-oriented micropillars deformed by slip in $\langle 111\rangle\{110\}$ while $[1\bar{2}8]$-oriented micropillars deformed by kink banding.
- Very high ductility was obtained for the compressed micropillars in contrast to the semi-brittle bulk specimens. This might be due to surface effects such as Ga ion damage as well as the fact that, at the (sub-) micron scale, plasticity is dominated by dislocation source activation rather than dislocation-dislocation interaction (thus minimizing deformation induced embrittlement effects).
- The strain-stress response of the pillars evidenced the plastic behavior of highly anisotropic materials, showing the effect that crystal orientation has in the overall mechanical response. More importantly, plastic anisotropy, defined as the ratio of

the critical resolved shear stresses between hard and soft crystals, strongly decreased with decreasing sample size. The reduced plastic anisotropy might be attributed to a decrease in the intrinsic resistance of the specimens at the sub-micron scale (surface effects).

- Very dissimilar size effects were observed as a function of crystal orientation. Soft crystals exhibited a strong size effect, similar to that observed in FCC metals. By contrast, hard crystals exhibited a diminished size effect, similar to those found in BCC metals or other materials (GaAs, LiF, MgO, Si) that have relatively large bulk strengths at room temperature. These results are a consequence of the activation of different slip systems depending on crystal orientation, thus leading to very different lattice resistance levels (bulk strength). This is, in turn, strongly related to the degree of screw dislocation mobility, as is also the case for BCC micropillars [7,189].

7 Concluding remarks

The plastic deformation of metals in the nano and micron regime varies essentially from that in the macro regime. A transition from dislocation-dislocation interaction controlled deformation at the macroscale to dislocation source nucleation controlled deformation at the nano- and microscale gives rise to a size effect on strength. The magnitude of this effect has been shown to differ from one material to another one. For instance, FCC metals with dimensions in the micrometer range show a universal scaling power-law exponent whereas BCC metals exhibit different degrees of size dependence. This disparity has been previously attributed to differences in the relative motion of screw and edge dislocations. In BCC metals, the deformation is dominated by screw dislocations that exhibit non-planar dislocation cores and thus high intrinsic resistance. The limited mobility of screw dislocations can be overcome through thermally activation mechanisms, causing a change in the size effect with temperature. In broad terms, this implies that differences in the lattice resistance may be responsible for the different degrees of size effects. However, so far, no effort had been made to consistently study the effect of lattice resistance (bulk strength) and screw dislocation mobility on the size strengthening dependence of BCC-based structures.

Therefore, this work was focused on investigating size-strengthening effects in BCC and B2 metals. In particular, Ta and W single crystal micropillars were compressed at different temperatures in order to systematically change the bulk strength. Also, β-CuZn, with a low thermal component to the strength at room temperature, was investigated. The influence of bulk strength and screw dislocation mobility was further investigated by compressing single crystal NiAl micropillars with different crystallographic orientations (different bulk strengths) at room temperature. From this research, the main conclusions are:

- The elevated-temperature compression tests performed in Ta and W micropillars at temperatures between 25 and 400 °C clearly indicate that temperature influences size-strengthening effects. It was found that the magnitude of the size effect is the result of the relative contributions of the size independent and size dependent factors to strength: lattice resistance and forest hardening against activation of dislocation sources.

- Assuming our pillars have a constant initial dislocation density, the temperature-dependent size effects of BCC micropillars depend mainly on the magnitude of the lattice resistance, which can be interpreted in terms of the temperature ratio T_{test}/T_c. Our results confirmed the hypothesis first put forward by Schneider *et al.* [7] that, at T_{test}/T_c close to or above 1, size effects in the order of FCC metals are observed, while at lower T_{test}/T_c, size effects are diminished due to the higher bulk stress as a base line.

- A change from uniform wavy deformation to localized deformation with increasing temperature and pillar size in W micropillars was the first clear manifestation of the importance of the relative motion of screw and edge dislocations in the deformation of micron-sized BCC structures. We supported these results by evaluating strain hardening, which was shown to be temperature dependent. Strain hardening was clearly found to decrease with increasing temperature, thus indicating easier activation of dislocation sources near the surface and better dislocation mobility at higher temperatures.

- In line with these findings, room-temperature compression tests performed on β-CuZn and NiAl micropillars further evidenced the influence of the lattice resistance on size effects in BCC-based structures. β-CuZn, with a low lattice resistance at room temperature, exhibited a size dependence similar to that of FCC pillars. As the test temperature was above the critical temperature, screw and edge dislocations were assumed to have similar mobility. NiAl pillars oriented along different crystal orientations exhibited very different plastic response as a result of the activation of different slip systems: $\langle 111 \rangle \{110\}$ and $\langle 100 \rangle \{110\}$. More importantly, this gave rise to very different size effects depending on crystal orientation. Soft crystals ($[1\bar{2}3]$-oriented pillars) exhibited a size effect in the range of FCC metals while hard crystals ($[001]$-oriented pillars) showed much

lower values. These differences stem from the large disparity in lattice resistance levels that ⟨111⟩ and ⟨100⟩ dislocations exhibit.

- The experiments on β-CuZn and NiAl micropillars also indicate that, at the sub-micron scale, the deformation behavior changes considerably. At a size regime where surface dislocation nucleation is assumed to become the dominant deformation mechanism, surface effects might promote these changes. For instance, plasticity in NiAl micropillars showed that the inherent plastic anisotropy of this material is drastically reduced with decreasing sample size. This decrease suggests that the influence of the screw dislocations vanishes, as first postulated by Schneider *et al.* [7] to explain the convergence of the yield strength for FCC and BCC pillars. This was hypothetically ascribed to surface-dislocation source activation effects: enhancement of screw dislocation mobility through kink-pair nucleation at the free surface or Ga ion implantation effects. Also, for NiAl micropillars, ductility increased largely in contrast to the semi-brittle bulk specimens. This might be attributed to surface effects such as Ga ion damage combined with the fact that, at the (sub-) micron scale, plasticity is controlled by dislocation source activation rather than by forest hardening.

7.1 Outlook

Microcompression testing has been shown to be a suitable technique to study the deformation mechanisms of BCC-based metals at the nano and microscale. However, in order to provide a clear picture of the dislocation mechanisms responsible for size effects in BCC and B2 alloys, coupling with other imaging techniques other than SEM would be beneficial. For instance, *in situ* TEM or μ-Laue diffraction compression of micropillars would provide very valuable information about dislocation processes. These *in situ* methods could directly reveal the type and the formation of dislocations that are responsible for the plastic deformation of these metals, and thus discern from Ga ion effects, which might become important for pillar sizes below 500 nm in diameter. In addition, computer simulations would be also crucial to understand deformation.

In line with the β-CuZn and NiAl work done in this thesis, there are still many open questions regarding the plastic deformation of this class of alloys (B2), in which micropillar compression would be extremely useful:

- B2 metals that slip along ⟨111⟩ usually exhibit an anomalous temperature dependence of the yield strength (β-CuZn). The origin of such an anomalous dependence is not understood in many cases. Moreover, it is not known if the peak in the stress-temperature curve would be affected by the sample size due to, for instance, surface effects. Thus, *in situ* SEM and/or TEM temperature dependent pillar compression testing would give further insights into this phenomenon.
- Stoichiometric CuZn may present an ordered or disordered structure. In the ordered state (β-CuZn), the material has a B2 crystal structure and deforms by $a/2\,\langle 111\rangle$ superpartial dislocations that are coupled via an APB as explained in this thesis. In contrast, the disordered alloy has a BCC crystal structure, and deforms by independent $a/2\,\langle 111\rangle$ dislocations. Compared to BCC metals that have previously been tested, this BCC metal has a critical temperature above room temperature and should therefore behave like an FCC metal. It would be interesting to compare the effect of atomic ordering at the microscale and investigate how size effects are influenced by that.
- A special class of B2 alloys is known to have greater than expected ductility. Previous studies indicate that these materials mainly deform along the ⟨100⟩ slip vector, but become ductile due to the activation of a hard slip mode involving ⟨111⟩ dislocation. Although the activation of the additional slip vector can explain the significant ductility of these materials, it is still unknown how and why these dislocations are formed. In particular, it is observed that they only appear at a certain stress level, but are not initially present in the material. *In situ* micropillar testing might provide valuable insight here. Due to the small size of the samples, a much larger volume fraction of the sample can be analyzed compared to bulk, enabling to rule out other mechanisms which were proposed to explain the greater than expected ductility of B2 metals. For example, it is possible that twinning or stress-induced transformations contribute to the deformation. However, in previous experiments no evidence for those mechanisms could be found. This might be related to the small amount of material that was investigated or the resolution limit of the methods used.

All these results and suggestions do one's bits towards the understanding of not only the deformation behavior of crystalline materials at the nano-/microscale, but also the size effect on strength in crystalline materials. This has been the focus of many researchers

during the last decade to eventually determine, for instance, a useful design parameter for technological applications. In this respect, researchers have started to envision possible applications developing new strategies for engineering design other than classical strengthening strategies. This is the case of ‘architected’ materials, i.e., materials with cellular-like structures made of microlattices, that may be used as structural materials with superior mechanical properties such as high relative strength and ductility. This evidences that such a fundamental research together with the fact that innovative nano-/microfabrication techniques continue to emerge will certainly open new pathways to the design of structural materials with improved and tuned mechanical properties.

8 References

1. Arzt, E. Size effects in materials due to microstructural and dimensional constraints: a comparative review. *Acta Mater.* **46,** 5611–5626 (1998).
2. Nix, W. D. Mechanical properties of thin films. *Metall. Trans. A* **20,** 2217–2245 (1989).
3. Freund, L. B. The stability of a dislocation threading a strained layer on a substrate. *J. Appl. Mech.* **54,** 553–557 (1987).
4. Uchic, M. D., Dimiduk, D. M., Florando, J. N. & Nix, W. D. Sample dimensions influence strength and crystal plasticity. *Science* **305,** 986–9 (2004).
5. Uchic, M. D., Shade, P. A. & Dimiduk, D. M. Plasticity of micrometer-scale single crystals in compression. *Annu. Rev. Mater. Res.* **39,** 361–386 (2009).
6. Schneider, A. S., Clark, B. G., Frick, C. P., Gruber, P. A. & Arzt, E. Effect of orientation and loading rate on compression behavior of small-scale Mo pillars. *Mater. Sci. Eng. A* **508,** 241–246 (2009).
7. Schneider, A. S. *et al.* Correlation between critical temperature and strength of small-scale bcc pillars. *Phys. Rev. Lett.* **103,** 1–4 (2009).
8. Schneider, A. S., Frick, C. P., Arzt, E., Clegg, W. J. & Korte, S. Influence of test temperature on the size effect in molybdenum small-scale compression pillars. *Philos. Mag. Lett.* 1–8 (2013).
9. Frick, C. P., Orso, S. & Arzt, E. Loss of pseudoelasticity in nickel–titanium sub-micron compression pillars. *Acta Mater.* **55,** 3845–3855 (2007).
10. Frick, C. P. *et al.* On the plasticity of small-scale nickel–titanium shape memory alloys. *Scr. Mater.* **62,** 492–495 (2010).
11. Clark, B. G., Gianola, D. S., Kraft, O. & Frick, C. P. Size independent shape memory behavior of nickel–titanium. *Adv. Eng. Mater.* **12,** 808–815 (2010).
12. Hull, D. & Bacon, D. J. *Introduction to dislocations*. (Elsevier, Butterworth-Heinemann, 2011).
13. Hirth, J. P. & Lothe, J. *Theory of dislocations*. (Krieger Publishing Company, 1992).
14. Argon, A. S. *Strengthening mechanisms in crystal plasticity*. (Oxford University Press, 2008).
15. Schmid, E. Zn - Normal stress law. in *Proceedings of the International Congress on Applied Mechanics* 324 (1924).

16. Kubin, L. P. Reviews on the deformation behavior of materials. *Reviews on the deformation behavior of materials* **4,** 181–275 (1982).

17. Taylor, G. I. & Elam, C. F. The distortion of iron crystals. *Proc. R. Soc. London A Math. Phys. Eng. Sci.* **112,** 337–361 (1926).

18. Šesták, B. & Zárubová, N. Asymmetry of slip in Fe-Si alloy single crystals. *Phys. status solidi* **10,** 239–250 (1965).

19. Seeger, A. & Hollang, L. The flow-stress asymmetry of ultra-pure molybdenum single crystals. *Mater. Trans. JIM* **41,** 141–151 (2000).

20. Sesták, B. & Seeger, A. Gleitung und Verfestigung in kubisch-raumzentrierten Metallen und Legierungen (II). *Z. Met.* **69,** 355 (1978).

21. Sesták, B. & Seeger, A. Gleitung und Verfestigung in kubisch-raumzentrierten Metallen und Legierungen (I). *Z. Met.* **69,** 195 (1978).

22. Christian, J. W. Some surprising features of the plastic deformation of body-centered cubic metals and alloys. *Metall. Trans. A* **14,** 1237–1256 (1983).

23. Hirsch, P. B. No Title. in *Proceedings of the Fifth International Conference on Crystallography* 139 (Cambridge University Press, 1960).

24. Seeger, A. Why anomalous slip in body-centred cubic metals? *Mater. Sci. Eng. A* **319-321,** 254–260 (2001).

25. Hollang, L., Brunner, D. & Seeger, A. Work hardening and flow stress of ultrapure molybdenum single crystals. *Mater. Sci. Eng. A* **319-321,** 233–236 (2001).

26. Vitek, V. & Paidar, V. in *Dislocations in Solids* **14,** 439–514 (Elsevier, 2008).

27. Seeger, A. The temperature and strain-rate dependence of the flow stress of body-centred cubic metals: A theory based on kink-kink interactions. *Z. Met.* **72,** 369–380 (1981).

28. Seeger, A. Progress and problems in the understanding of the dislocation relaxation processes in metals. *Mater. Sci. Eng. A* **370,** 50–66 (2004).

29. Seeger, A. Peierls barriers, kinks, and flow stress: Recent progress. *Zeitschrift für Met.* **93,** 760–777 (2002).

30. Taylor, G. I. The deformation of crystals of ß-brass. *Proc. R. Soc. London A* **118,** 1–24 (1928).

31. Taylor, G. Thermally-activated deformation of BCC metals and alloys. *Prog. Mater. Sci.* **36,** 29–61 (1992).

32. Seeger, A. & Wasserbäch, W. Anomalous slip – A feature of high-purity body-centred cubic metals. *Phys. status solidi* **189,** 27–50 (2002).

33. Miracle, D. B. Overview No. 104 The physical and mechanical properties of NiAl. *Acta Metall. Mater.* **41,** 649–684 (1993).

34. Ball, A. & Smallman, R. . The operative slip system and general plasticity of NiAl-II. *Acta Metall.* **14,** 1517–1526 (1966).

35. Ball, A. & Smallman, R. E. The deformation properties and electron microscopy studies of the intermetallic compound NiAl. *Acta Metall.* **14,** 1349–1355 (1966).

36. Loretto, M. H. & Wasilewski, R. J. Slip systems in NiAl single crystals at 300°K and 77°K. *Philos. Mag.* **23,** 1311–1328 (1971).

37. Lin, Y.-S., Cak, M., Paidar, V. & Vitek, V. Why is the slip direction different in different B2 alloys? *Acta Mater.* **60,** 881–888 (2012).

38. Russell, A. M. & Lee, K. L. in *Structure-property relations in nonferrous metals* 520 (John Wiley & Sons Ltd, 2005).

39. Baker, I. A review of the mechanical properties of B2 compounds. *Mater. Sci. Eng. A* **192-193,** 1–13 (1995).

40. Yoo, M. H., Takasugi, T., Hanada, S. & Izumi, O. Slip modes in B2-type intermetallic alloys. *Mater. Trans. JIM* **31,** 435–442 (1990).

41. Gschneidner, K. *et al.* A family of ductile intermetallic compounds. *Nat. Mater.* **2,** 587–91 (2003).

42. Saka, H. Strength anomaly of β -CuZn. *Memoirs of the School of Engineering* **52,** (Nagoya University, 2001).

43. Yamaguchi, M. & Umakoshi, Y. The operative slip systems and slip line morphology in βCuZn and β(CuNi)Zn alloys. *Acta Metall.* **24,** 1061–1067 (1976).

44. Umakoshi, Y., Yamaguchi, M., Namba, L. & Murakami, K. The effect of crystal orientation on the strength anomaly in β CuZn at around 200°C. *Acta Metall.* **24,** 89–93 (1976).

45. Takasugi, T., Hanada, S., Yoshida, M. & Shindo, D. A model for strength anomaly in IVa-VIII B2 ordered intermetallics. *Philos. Mag. A* **71,** 347–358 (1995).

46. Taylor, A. & Jones, R. M. Constitution and magnetic properties of iron-rich iron-aluminum alloys. *J. Phys. Chem. Solids* **6,** 16–37 (1958).

47. Mulay, R. P. & Agnew, S. R. Hard slip mechanisms in B2 CoTi. *Acta Mater.* **60,** 1784–1794 (2012).

48. Ardley, G. W. & Cottrell, A. H. Yield points in brass crystals. *Proc. R. Soc. London. Ser. A. Math. Phys. Sci.* **219,** 328–341 (1953).

49. Takeuchi, S., Hashimoto, T., Suzuki, K. & Ichihara, M. Plastic deformation of β-CuZn single crystals at low temperatures. *Acta Metall.* **30,** 513–521 (1982).

50. Dirras, G., Beauchamp, P. & Veyssière, P. Weak-beam study of the dislocation microstructure of β-CuZn deformed in the temperature domain of the plastic anomaly. *Philos. Mag. A* **65,** 815–828 (1992).

51. Matsumoto, A. & Saka, H. Strength anomaly in β-CuZn single crystals deformed in direct shear. *Philos. Mag. A* **67,** 217–229 (1993).

52. Saka, H. & Zhu, Y. M. Climb dissociation of 〈111〉 superdislocations in β-CuZn. *Philos. Mag. A* **51,** 629–637 (1985).

53. Saka, H., Zhu, Y. M., Kawase, M., Nohara, A. & Imura, T. The anomalous strength peak and the transition of slip direction in β-CuZn. *Philos. Mag. A* **51,** 365–371 (1985).

54. Hanada, S. & Izumi, O. Orientation dependence of yield stress and operative slip systems of ß-CuZn single crystals at low temperatures. *Phys. Status Solidi* **40,** (1977).

55. Nohara, A., Izumi, M., Saka, H. & Imura, T. Plastic deformation behavior of β-CuZn single crystals at low and high temperatures. *Phys. status solidi* **82,** 163–170 (1984).

56. Hanada, S., Mohri, M. & Izumi, O. Plasticity of β-brass single crystals at low temperatures. *Sci. reports Res. Institutes, Tohoku Univ.* **26,** 370–371 (1975).

57. Caillard, D. & Couret, A. in *Dislocations in Solids* (eds. Nabarro, F. R. N. & Duesbery, M. S.) **10,** 69–134 (Elsevier, 1996).

58. Lee, K. A. & Lee, C. S. The effect of strain rate on the anomalous peak of yield stress in β-CuZn alloy. *Scr. Mater.* **39,** 1289–1294 (1998).

59. Nohara, A. & Imura, T. Yield-point phenomenon in a β-CuZn single crystal at high temperatures. *Phys. status solidi* **84,** (1984).

60. Beauchamp, P., Dirras, G. & Veyssière, P. Calculation of antiphase boundaries on {110} planes in a B2 ordered compound by the cluster variation method. *Philos. Mag. A* **65,** 477–496 (1992).

61. Saka, H. & Kawase, M. Dislocation structures of β-CuZn deformed in compression between 25 and 300°C. *Philos. Mag. A* **49,** 525–533 (1984).

62. Saka, H., Kawase, M., Nohara, A. & Imura, T. Anti-phase boundary energy in β-CuZn. *Philos. Mag. A* **50,** 65–70 (1984).

63. Zhu, Y. M. & Saka, H. Climb dissociation of superlattice dislocations and the strength anomaly in β-brass. *Philos. Mag. A* **59,** 661–676 (1989).

64. Pascoe, R. T. & Newey, C. W. A. Deformation modes of the intermediate phase NiAl. *Phys. status solidi* **29,** 357–366 (1968).

65. Pascoe, R. T. & Newey, C. W. A. The mechanical behaviour of the intermediate phase NiAl. *Met. Sci.* **2,** 138–143 (1968).

66. Fraser, H. L., Smallman, R. E. & Loretto, M. H. The plastic deformation of NiAl single crystals between 300°K and 1050°K. *Philos. Mag.* **28,** 651–665 (1973).

67. Noebe, R. D., Bowman, R. R. & Nathal, M. V. Physical and mechanical properties of the B2 compound NiAl. *Int. Mater. Rev.* **38,** 193–232 (1993).

68. Field, R. D., Lahrman, D. F. & Darolia, R. Slip systems in 〈001〉 oriented NiAl single crystals. *Acta Metall. Mater.* **39,** 2951–2959 (1991).

69. Wasilewski, R. J., Butler, S. R. & Hanlon, J. E. Plastic deformation of single-crystal NiAl. *Trans. Met. Soc. AIME* **239,** 1357–1364 (1967).

70. Lahrman, D. F., Field, R. D. & Darolia, R. The effect of strain rate on the mechanical properties of single crystal NiAl. High temperature ordered intermetallic alloys IV. in *MRS Proc.* 603 (1991).

71. Pascoe, R. T. & Newey, C. W. A. Deformation processes in the intermediate phase NiAl. *Met. Sci.* **5,** 50–55 (1971).

72. Fraser, H. L., Smallman, R. E. & Loretto, M. H. The plastic deformation of NiAl single crystals between 300°K and 1050°K. *Philos. Mag.* **28,** 667–677 (1973).

73. Hess, J. B. & Barrett, C. S. Structure and nature of kink bands in zinc. *Trans. Met. Soc. AIME* 185 (1949).

74. Zhang, L., Jenkins, M. L. & Taylor, G. Model for kink-like deformation in CoTi single crystals. *J. Mater. Sci.* **41,** 2631–2639 (2006).

75. Takasugi, T., Kishino, J. & Hanada, S. Stress asymmetry of stoichiometric NiAl single crystals. *Acta Metall. Mater.* **41,** 1021–1031 (1993).

76. Mielec, J., Novák, V., Zárubová, N. & Gemperle, A. Orientation dependence of plastic deformation in NiAl single crystals. *Mater. Sci. Eng. A* **236,** 410–413 (1997).

77. Bowman, R. R., Noebe, R. D. & Darolia, R. Mechanical properties and deformation mechanisms of NiAl. *HITEMPReview. NASA* **47,** 1–15 (1989).

78. Corcoran, S. G., Colton, R. J., Lilleodden, E. T. & Gerberich, W. W. Anomalous plastic deformation at surfaces: Nanoindentation of gold single crystals. *Phys. Rev. B* **55,** R16057–R16060 (1997).

79. Page, T. F., Oliver, W. C. & McHargue, C. J. The deformation behavior of ceramic crystals subjected to very low load (nano)indentations. *J. Mater. Res.* **7,** 450–473 (1992).

80. Gerberich, W. W., Nelson, J. C., Lilleodden, E. T., Anderson, P. & Wyrobek, J. T. Indentation induced dislocation nucleation: The initial yield point. *Acta Mater.* **44,** 3585–3598 (1996).

81. McElhaney, K. W., Vlassak, J. J. & Nix, W. D. Determination of indenter tip geometry and indentation contact area for depth-sensing indentation experiments. *J. Mater. Res.* **13,** 1300–1306 (1998).

82. Shan, Z. W., Mishra, R. K., Syed Asif, S. a, Warren, O. L. & Minor, A. M. Mechanical annealing and source-limited deformation in submicrometre-diameter Ni crystals. *Nat. Mater.* **7,** 115–9 (2008).

83. Dimiduk, D. M., Uchic, M. D. & Parthasarathy, T. A. Size-affected single-slip behavior of pure nickel microcrystals. *Acta Mater.* **53,** 4065–4077 (2005).

84. Frick, C. P., Clark, B. G., Orso, S., Schneider, A. S. & Arzt, E. Size effect on strength and strain hardening of small-scale [111] nickel compression pillars. *Mater. Sci. Eng. A* **489,** 319–329 (2008).

85. Greer, J. & Nix, W. Nanoscale gold pillars strengthened through dislocation starvation. *Phys. Rev. B* **73,** 245410 (2006).

86. Greer, J. R., Oliver, W. C. & Nix, W. D. Size dependence of mechanical properties of gold at the micron scale in the absence of strain gradients. *Acta Mater.* **53,** 1821–1830 (2005).

87. Volkert, C. A. & Lilleodden, E. T. Size effects in the deformation of sub-micron Au columns. *Philos. Mag.* **86,** 5567–5579 (2006).

88. Kim, J.-Y. & Greer, J. R. Tensile and compressive behavior of gold and molybdenum single crystals at the nano-scale. *Acta Mater.* **57,** 5245–5253 (2009).

89. Greer, J. R., Weinberger, C. R. & Cai, W. Comparing the strength of f.c.c. and b.c.c. sub-micrometer pillars: compression experiments and dislocation dynamics simulations. *Mater. Sci. Eng. A* **493,** 21–25 (2008).

90. Nix, W. D., Greer, J. R., Feng, G. & Lilleodden, E. T. Deformation at the nanometer and micrometer length scales: Effects of strain gradients and dislocation starvation. *Thin Solid Films* **515,** 3152–3157 (2007).

91. Kiener, D., Motz, C., Schöberl, T., Jenko, M. & Dehm, G. Determination of mechanical properties of copper at the micron scale. *Adv. Eng. Mater.* **8,** 1119–1125 (2006).

92. Kiener, D. & Minor, A. M. Source-controlled yield and hardening of Cu (1 0 0) studied by in situ transmission electron microscopy. *Acta Mater.* **59,** 1328–1337 (2011).

93. Ng, K. S. & Ngan, A. H. W. Stochastic nature of plasticity of aluminum micro-pillars. *Acta Mater.* **56,** 1712–1720 (2008).

94. Zaiser, M. *et al.* Strain bursts in plastically deforming molybdenum micro- and nanopillars. *Philos. Mag.* **88,** 3861–3874 (2008).

95. Kim, J.-Y. & Greer, J. R. Size-dependent mechanical properties of molybdenum nanopillars. *Applied Physics Letters* **93,** 101913–101916 (2008).

96. Brinckmann, S., Kim, J.-Y. & Greer, J. R. Fundamental differences in mechanical behavior between two types of crystals at the nanoscale. *Phys. Rev. Lett.* **100,** 155502 (2008).

97. Schneider, A. S., Frick, C. P., Clark, B. G., Gruber, P. A. & Arzt, E. Influence of orientation on the size effect in bcc pillars with different critical temperatures. *Mater. Sci. Eng. A* 1540–1547 (2011).

98. Kim, J.-Y., Jang, D. & Greer, J. R. Tensile and compressive behavior of tungsten, molybdenum, tantalum and niobium at the nanoscale. *Acta Mater.* **58,** 2355–2363 (2010).

99. Kim, J.-Y., Jang, D. & Greer, J. R. Insight into the deformation behavior of niobium single crystals under uniaxial compression and tension at the nanoscale. *Scr. Mater.* **61,** 300–303 (2009).

100. Han, S. M., Bozorg-Grayeli, T., Groves, J. R. & Nix, W. D. Size effects on strength and plasticity of vanadium nanopillars. *Scr. Mater.* **63,** 1153–1156 (2010).

101. Kaufmann, D., Mönig, R., Volkert, C. a. & Kraft, O. Size dependent mechanical behaviour of tantalum. *Int. J. Plast.* **27,** 470–478 (2011).

102. Zhu, T. T., Bushby, A. J. & Dunstan, D. J. Materials mechanical size effects: a review. *Mater. Technol. Adv. Perform. Mater.* **23,** 193–209 (2008).

103. Kraft, O., Gruber, P. a., Mönig, R. & Weygand, D. Plasticity in confined dimensions. *Annu. Rev. Mater. Res.* **40,** 293–317 (2010).

104. Greer, J. R. & De Hosson, J. T. M. Plasticity in small-sized metallic systems: Intrinsic versus extrinsic size effect. *Prog. Mater. Sci.* **56,** 654–724 (2011).

105. Bei, H., Shim, S., Pharr, G. M. & George, E. P. Effects of pre-strain on the compressive stress–strain response of Mo-alloy single-crystal micropillars. *Acta Mater.* **56,** 4762–4770 (2008).

106. Taylor, G. I. The mechanism of plastic deformation of crystals. Part I. Theoretical. *Proc. R. Soc. A Math. Phys. Eng. Sci.* **145,** 362–387 (1934).

107. Greer, J. R. Bridging the gap between computational and experimental length scales: A review on nano-scale plasticity. *Rev. Adv. Mater. Sci.* **13,** 59–70 (2006).

108. H. Tang, Schwarz, K. W. & Espinosa, H. D. Dislocation escape-related size effects in single-crystal micropillars. *Acta Mater.* 1607–1616 (2006).

109. Deshpande, V. S., Needleman, A. & Van der Giessen, E. Plasticity size effects in tension and compression of single crystals. *J. Mech. Phys. Solids* **53,** 2661–2691 (2005).

110. Balint, D. S., Deshpande, V. S., Needleman, a & Giessen, E. Van Der. Size effects in uniaxial deformation of single and polycrystals: a discrete dislocation plasticity analysis. *Model. Simul. Mater. Sci. Eng.* **14,** 409–422 (2006).

111. Norfleet, D. M., Dimiduk, D. M., Polasik, S. J., Uchic, M. D. & Mills, M. J. Dislocation structures and their relationship to strength in deformed nickel microcrystals. *Acta Mater.* **56,** 2988–3001 (2008).

112. von Blanckenhagen, B., Gumbsch, P. & Arzt, E. Discrete dislocation simulation of thin film plasticity. *MRS Online Proc. Libr.* **673,** null–null (2001).

113. Parthasarathy, T. A., Rao, S. I., Dimiduk, D. M., Uchic, M. D. & Trinkle, D. R. Contribution to size effect of yield strength from the stochastics of dislocation source lengths in finite samples. *Scr. Mater.* **56,** 313–316 (2007).

114. Rao, S. I. *et al.* Estimating the strength of single-ended dislocation sources in micron-sized single crystals. *Philos. Mag.* **87,** 4777–4794 (2007).

115. Ngan, A. H. W. & Ng, K. S. Transition from deterministic to stochastic deformation. *Philos. Mag.* **90,** 1937–1954 (2010).

116. El-Awady, J. a., Bulent Biner, S. & Ghoniem, N. M. A self-consistent boundary element, parametric dislocation dynamics formulation of plastic flow in finite volumes. *J. Mech. Phys. Solids* **56,** 2019–2035 (2008).

117. El-Awady, J. a., Wen, M. & Ghoniem, N. M. The role of the weakest-link mechanism in controlling the plasticity of micropillars. *J. Mech. Phys. Solids* **57,** 32–50 (2009).

118. Oh, S. H., Legros, M., Kiener, D. & Dehm, G. In situ observation of dislocation nucleation and escape in a submicrometre aluminium single crystal. *Nat. Mater.* **8,** 95–100 (2009).

119. Sedláček, R. Orowan-type size effect in plastic bending of free-standing thin crystalline strips. *Mater. Sci. Eng. A* **393,** 387–395 (2005).

120. Budiman, A. S. *et al.* A search for evidence of strain gradient hardening in Au submicron pillars under uniaxial compression using synchrotron X-ray microdiffraction. *Acta Mater.* **56,** 602–608 (2008).

121. Friedman, L. H. & Chrzan, D. C. Continuum analysis of dislocation pile-ups: Influence of sources. *Philos. Mag. A* **77,** 1185–1204 (1998).

122. Hall, E. O. The deformation and ageing of mild steel: III Discussion of results. *Proc. Phys. Soc. Sect. B* **64,** 747 (1951).

123. Petch, N. J. The cleavage strength of polycrystals. *Iron Steel Inst.* **174,** 25–28 (1953).

124. Kiener, D. & Minor, A. M. Source truncation and exhaustion: Insights from quantitative in situ TEM tensile testing. *Nano Lett.* **11,** 3816–3820 (2011).

125. Lee, S.-W., Han, S. M. & Nix, W. D. Uniaxial compression of fcc Au nanopillars on an MgO substrate: The effects of prestraining and annealing. *Acta Mater.* **57,** 4404–4415 (2009).

126. Dimiduk, D. M., Woodward, C., Lesar, R. & Uchic, M. D. Scale-free intermittent flow in crystal plasticity. *Science* **312,** 1188–90 (2006).

127. Uchic, M. D., Shade, P. A. & Dimiduk, D. M. Micro-compression testing of fcc metals : A selected overview of experiments and simulations. *JOM* **61,** 36–41 (2009).

128. Uchic, M. D. & Dimiduk, D. M. A methodology to investigate size scale effects in crystalline plasticity using uniaxial compression testing. *Mater. Sci. Eng. A* **400-401,** 268–278 (2005).

129. Uchic, M. D., Dimiduk, D. M., Wheeler, R., Shade, P. a. & Fraser, H. L. Application of micro-sample testing to study fundamental aspects of plastic flow. *Scr. Mater.* **54,** 759–764 (2006).

130. Kiener, D., Motz, C. & Dehm, G. Micro-compression testing: A critical discussion of experimental constraints. *Mater. Sci. Eng. A* **505,** 79–87 (2009).

131. Dou, R. & Derby, B. A universal scaling law for the strength of metal micropillars and nanowires. *Scr. Mater.* **61,** 524–527 (2009).

132. Lee, S.-W., Cheng, Y., Ryu, I. & Greer, J. R. Cold-temperature deformation of nano-sized tungsten and niobium as revealed by in-situ nano-mechanical experiments. *Sci. China Technol. Sci.* **57,** 652–662 (2014).

133. Rogne, B. R. S. & Thaulow, C. Effect of crystal orientation on the strengthening of iron micro pillars. *Mater. Sci. Eng. A* (2015).

134. Kaufmann, D., Schneider, A. S., Mönig, R., Volkert, C. A. & Kraft, O. Effect of surface orientation on the plasticity of small bcc metals. *Int. J. Plast.* **49,** 145–151 (2013).

135. Schneider, A. S., Clark, B. G., Frick, C. P., Gruber, P. A. & Arzt, E. Effect of pre-straining on the size effect in molybdenum pillars. *Philos. Mag. Lett.* **90,** 841–849 (2010).

136. Schneider, A. S., Clark, B. G., Frick, C. P. & Arzt, E. Correlation between activation volume and pillar diameter for Mo and Nb bcc pillars. *MRS Online Proc. Libr.* **1185,** 1185–II07–04 (2009).

137. Rogne, B. R. S. & Thaulow, C. Strengthening mechanisms of iron micropillars. *Philos. Mag.* 1–15 (2014).

138. Korte, S. & Clegg, W. J. Discussion of the dependence of the effect of size on the yield stress in hard materials studied by microcompression of MgO. *Philos. Mag.* **91,** 1150–1162 (2011).

139. Schneider, A. S. Mechanical properties of small BCC metal structures. (Universität Stuttgart, 2010).

140. Weinberger, C. R. & Cai, W. Surface-controlled dislocation multiplication in metal micropillars. *Proc. Natl. Acad. Sci. U. S. A.* **105,** 14304–7 (2008).

141. Hollang, L., Hommel, M. & Seeger, A. The flow stress of ultra-high-purity molybdenum single crystals. *Phys. status solidi* **160,** 329–354 (1997).

142. Lee, S.-W. & Nix, W. D. Size dependence of the yield strength of fcc and bcc metallic micropillars with diameters of a few micrometers. *Philos. Mag.* **92,** 1238–1260 (2012).

143. Han, S. M. *et al.* Critical-temperature/Peierls-stress dependent size effects in body centered cubic nanopillars. *Appl. Phys. Lett.* **102,** 41910–41915 (2013).

144. Segall, D. E., Strachan, A., Goddard III, W. A., Ismail-Beigi, S. & Arias, T. A. Ab initio and finite-temperature molecular dynamics studies of lattice resistance in tantalum. *Phys. Rev. B* **68,** 14104 (2003).

145. Hoge, K. G. & Mukherjee, A. K. The temperature and strain rate dependence of the flow stress of tantalum. *J. Mater. Sci.* **12,** 1666–1672 (1977).

146. Soler, R. *et al.* Understanding size effects on the strength of single crystals through high-temperature micropillar compression. *Acta Mater.* **81,** 50–57 (2014).

147. Hütsch, J. & Lilleodden, E. T. The influence of focused-ion beam preparation technique on microcompression investigations: Lathe vs. annular milling. *Scr. Mater.* **77,** 49–51 (2014).

148. Sneddon, I. The relation between load and penetration in the axisymmetric boussinesq problem for a punch of arbitrary profile. *Int. J. Eng. Sci.* **3,** 47–57 (1965).

149. Wheeler, J. M. & Michler, J. Elevated temperature, nano-mechanical testing in situ in the scanning electron microscope. *Rev. Sci. Instrum.* **84,** 45103–45115 (2013).

150. Kiener, D., Motz, C., Rester, M., Jenko, M. & Dehm, G. FIB damage of Cu and possible consequences for miniaturized mechanical tests. *Mater. Sci. Eng. A* **459,** 262–272 (2007).

151. McCaffrey, J. P., Phaneuf, M. W. & Madsen, L. D. Surface damage formation during ion-beam thinning of samples for transmission electron microscopy. *Ultramicroscopy* **87,** 97–104 (2001).

152. Jamison, R. B., Mardinly, A. J., Susnitzky, D. W. & Gronsky, R. Effects of ion species and energy on the amorphization of Si during FIB TEM sample preparation as determined by computational and experimental methods. *Microsc. Microanal.* **6,** 526–527 (2000).

153. Prenitzer, B. I. *et al.* The correlation between ion beam/material interactions and practical FIB specimen preparation. *Microsc. Microanal.* **9,** 216–236 (2003).

154. Rubanov, S. & Munroe, P. R. Investigation of the structure of damage layers in TEM samples prepared using a focused ion beam. *J. Mater. Sci. Lett.* **20,** 1181–1183 (2001).

155. Rubanov, S. & Munroe, P. R. FIB-induced damage in silicon. *J. Microsc.* **214,** 213–221 (2004).

156. Shim, S., Bei, H., Miller, M. K., Pharr, G. M. & George, E. P. Effects of focused ion beam milling on the compressive behavior of directionally solidified micropillars and the nanoindentation response of an electropolished surface. *Acta Mater.* **57,** 503–510 (2009).

157. Zhang, H., Schuster, B. E., Wei, Q. & Ramesh, K. T. The design of accurate micro-compression experiments. *Scr. Mater.* **54,** 181–186 (2006).

158. Choi, Y. S., Uchic, M. D., Parthasarathy, T. a. & Dimiduk, D. M. Numerical study on microcompression tests of anisotropic single crystals. *Scr. Mater.* **57,** 849–852 (2007).

159. Shade, P. A. *et al.* A combined experimental and simulation study to examine lateral constraint effects on microcompression of single-slip oriented single crystals. *Acta Mater.* **57,** 4580–4587 (2009).

160. Schwaiger, R., Weber, M., Moser, B., Gumbsch, P. & Kraft, O. Mechanical assessment of ultrafine-grained nickel by microcompression experiment and finite element simulation. *J. Mater. Res.* **27,** 266–277 (2011).

161. Raabe, D., Ma, D. & Roters, F. Effects of initial orientation, sample geometry and friction on anisotropy and crystallographic orientation changes in single crystal microcompression deformation: A crystal plasticity finite element study. *Acta Mater.* **55,** 4567–4583 (2007).

162. Fleck, N. A. & Hutchinson, J. W. Strain gradient plasticity. *Adv. Appl. Mech.* **33,** 295–361 (1997).

163. Nix, W. D. & Gao, H. Indentation size effects in crystalline materials: A law for strain gradient plasticity. *J. Mech. Phys. Solids* **46,** 411–425 (1998).

164. Chen, Y., Kraft, O. & Walter, M. Size effects in thin coarse-grained gold microwires under tensile and torsional loading. *Acta Mater.* **87,** 78–85 (2015).

165. Seeger, A. Peierls barriers, kinks, and flow stress: Recent progress. *Int. J. Mater. Res.* **93,** 760–777 (2002).

166. Kim, J.-Y., Jang, D. & Greer, J. R. Crystallographic orientation and size dependence of tension–compression asymmetry in molybdenum nano-pillars. *Int. J. Plast.* **28,** 46–52 (2012).

167. El-Awady, J. A. *et al.* Pre-straining effects on the power-law scaling of size-dependent strengthening in Ni single crystals. *Scr. Mater.* **68,** 207–210 (2013).

168. Rao, S. I. *et al.* Athermal mechanisms of size-dependent crystal flow gleaned from three-dimensional discrete dislocation simulations. *Acta Mater.* **56,** 3245–3259 (2008).

169. Wheeler, J. M., Niederberger, C., Tessarek, C., Christiansen, S. & Michler, J. Extraction of plasticity parameters of GaN with high temperature, in situ micro-compression. *Int. J. Plast.* **40,** 140–151 (2013).

170. Ng, K. S. & Ngan, A. H. W. Stochastic theory for jerky deformation in small crystal volumes with pre-existing dislocations. *Philos. Mag.* **88,** 677–688 (2008).

171. Soler, R., Molina-Aldareguia, J. M., Segurado, J. & LLorca, J. Effect of misorientation on the compression of highly anisotropic single-crystal micropillars. *Adv. Eng. Mater.* **14,** 1004–1008 (2012).

172. Franke, O. *et al.* Incipient plasticity of single-crystal tantalum as a function of temperature and orientation. *Philos. Mag.* 1–12 (2014).

173. Gibson, J. S. K.-L., Roberts, S. G. & Armstrong, D. E. J. High temperature indentation of helium-implanted tungsten. *Mater. Sci. Eng. A* **625,** 380–384 (2015).

174. Chen, L. Y., He, M., Shin, J., Richter, G. & Gianola, D. S. Measuring surface dislocation nucleation in defect-scarce nanostructures. *Nat Mater* **14,** 707–713 (2015).

175. Zhu, T., Li, J., Samanta, A., Leach, A. & Gall, K. Temperature and strain-rate dependence of surface dislocation nucleation. *Phys. Rev. Lett.* **100,** 25502 (2008).

176. Kiener, D., Guruprasad, P. J., Keralavarma, S. M., Dehm, G. & Benzerga, A. A. Work hardening in micropillar compression: In situ experiments and modeling. *Acta Mater.* **59,** 3825–3840 (2011).

177. Smialek, R. L., Webb, G. L. & Mitchell, T. E. Solid solution softening in bcc metal alloys. *Scr. Metall.* **4,** 33–37 (1970).

178. Brunner, D. Comparison of flow-stress measurements on high-purity tungsten single crystals with the kink-pair theory. *Mater. Trans. JIM* **41,** 152–160 (2000).

179. Orlikowski, D., Söderlind, P. & Moriarty, J. A. First-principles thermoelasticity of transition metals at high pressure: Tantalum prototype in the quasiharmonic limit. *Phys. Rev. B* **74,** 54109 (2006).

180. Lowrie, R. & Gonas, M. Single-crystal elastic properties of tungsten from 24 to 1800°C. *J. Appl. Phys.* **38,** 4505 (1967).

181. Gouldstone, A. *et al.* Indentation across size scales and disciplines: Recent developments in experimentation and modeling. *Acta Mater.* **55,** 4015–4039 (2007).

182. Zhu, T. & Li, J. Ultra-strength materials. *Prog. Mater. Sci.* **55,** 710–757 (2010).

183. Brenner, S. S. Growth and properties of ‘whiskers’. *Science.* **128,** 569–575 (1958).

184. Richter, G. *et al.* Ultrahigh strength single crystalline nanowhiskers grown by physical vapor deposition. *Nano Lett.* **9,** 3048–3052 (2009).

185. Jennings, A. T., Burek, M. J. & Greer, J. R. Microstructure versus size: Mechanical properties of electroplated single crystalline Cu nanopillars. *Phys. Rev. Lett.* **104,** 135503 (2010).

186. Jennings, A. T. & Greer, J. R. Tensile deformation of electroplated copper nanopillars. *Philos. Mag.* **91,** 1108–1120 (2011).

187. Buzzi, S., Dietiker, M., Kunze, K., Spolenak, R. & Löffler, J. F. Deformation behavior of silver submicrometer-pillars prepared by nanoimprinting. *Philos. Mag.* **89,** 869–884 (2009).

188. Dietiker, M., Buzzi, S., Pigozzi, G., Löffler, J. F. & Spolenak, R. Deformation behavior of gold nano-pillars prepared by nanoimprinting and focused ion-beam milling. *Acta Mater.* **59,** 2180–2192 (2011).

189. Torrents Abad, O., Wheeler, J. M., Michler, J., Schneider, A. S. & Arzt, E. Temperature-dependent size effects on the strength of Ta and W micropillars. *Acta Mater.* **103,** 483–494 (2016).

190. Takasugi, T. & Izumi, O. Deformation of CoTi polycrystals. *J. Mater. Sci.* **23,** 1265–1273 (1988).

191. Cao, G. H. *et al.* Determination of slip systems and their relation to the high ductility and fracture toughness of the B2 DyCu intermetallic compound. *Acta Mater.* **55,** 3765–3770 (2007).

192. Kheradmand, N. & Vehoff, H. Orientation gradients at boundaries in micron-sized bicrystals. *Adv. Eng. Mater.* **14,** 153–161 (2012).

193. Kiener, D. *et al.* Influence of external and internal length scale on the flow stress of copper. *Int. J. Mater. Res.* **98,** 1047–1053 (2007).

194. Ishitani, T., Umemura, K., Ohnishi, T., Yaguchi, T. & Kamino, T. Improvements in performance of focused ion beam cross-sectioning: aspects of ion-sample interaction. *J. Electron Microsc. (Tokyo).* **53,** 443–449 (2004).

195. Nye, J. . Some geometrical relations in dislocated crystals. *Acta Metall.* **1,** 153–162 (1953).

196. Lee, K. A., Chang, Y. W. & Lee, C. S. An internal variable approach for anomalous yield phenomena of β-CuZn alloy. *Acta Mater.* **52,** 2913–2922 (2004).

197. Peng, C. *et al.* Strain rate dependent mechanical properties in single crystal nickel nanowires. *Appl. Phys. Lett.* **102,** 083102 (2013).

198. Popille, F., Kubin, L. P., Douin, J. & Naka, S. Portevin—Le Châtelier instabilities and stoichiometric effects in B2 titanium aluminides. *Scr. Mater.* **34,** 977–984 (1996).

199. Nandy, T. K., Feng, Q. & Pollock, T. M. Elevated temperature deformation and dynamic strain aging in polycrystalline RuAl alloys. *Intermetallics* **11,** 1029–1038 (2003).

200. Caillard, D. Yield-stress anomalies and high-temperature mechanical properties of intermetallics and disordered alloys. *Mater. Sci. Eng. A* **319-321,** 74–83 (2001).

201. Chen, Z. M., Mrovec, M. & Gumbsch, P. Atomistic aspects of 1/2 <111> screw dislocation behavior in α -iron and the derivation of microscopic yield criterion. *Model. Simul. Mater. Sci. Eng.* **21,** 55023 (2013).

202. Ng, K. S. & Ngan, A. H. W. Breakdown of Schmid's law in micropillars. *Scr. Mater.* **59,** 796–799 (2008).

203. Yamaguchi, M. & Umakoshi, V. Slip geometry and anomalous strengthening in β-Cu(ZnMn) single crystals. *Phys. Status Solidi* **43,** 667–674 (1977).

204. Jennings, A. T., Li, J. & Greer, J. R. Emergence of strain-rate sensitivity in Cu nanopillars: Transition from dislocation multiplication to dislocation nucleation. *Acta Mater.* **59,** 5627–5637 (2011).

205. L. P. Kubin & Y. Estrin. Dynamic strain ageing and the mechanical response of alloys. *J. Phys. III Fr.* **1,** 929–943 (1991).

206. Hähner, P. On the physics of the Portevin-Le Châtelier effect part 1: The statistics of dynamic strain ageing. *Mater. Sci. Eng. A* **207,** 208–215 (1996).

207. Li, J. The mechanics and physics of defect nucleation. *MRS Bull.* **32,** 151–159 (2011).

208. Miracle, D. B. & Darolia, R. NiAl and its alloys. *Intermet. Compd.* **3,** 55–74 (1995).

209. Mori, H., Fujita, H., Tendo, M. & Fujita, M. Amorphous transition in intermetallic compounds induced by electron irradiation. *Scr. Metall.* **18,** 783–788 (1984).

210. Noebe, R. D. & Gibala, R. Surface oxide softening of single crystal NiAl. *Scr. Metall.* **20,** 1635–1639 (1986).

211. Torrents Abad, O., Medina Clavijo, B., Frick, C. P., Schneider, A. S. & Arzt, E. *Size dependent deformation of beta brass*. (2016).

212. Iqbal, F., Ast, J., Göken, M. & Durst, K. In situ micro-cantilever tests to study fracture properties of NiAl single crystals. *Acta Mater.* **60,** 1193–1200 (2012).

213. Ast, J., Przybilla, T., Maier, V., Durst, K. & Göken, M. Microcantilever bending experiments in NiAl – Evaluation, size effects, and crack tip plasticity. *J. Mater. Res.* **29,** 2129–2140 (2014).

214. Gerberich, W. W., Tymiak, N. I., Grunlan, J. C., Horstemeyer, M. F. & Baskes, M. I. Interpretations of indentation size effects. *J. Appl. Mech.* **69,** 433 (2002).

215. Soler, R. *et al.* Micropillar compression of LiF [111] single crystals: Effect of size, ion irradiation and misorientation. *Int. J. Plast.* **36,** 50–63 (2012).

216. Schneider, A. S. *et al.* Influence of bulk pre-straining on the size effect in nickel compression pillars. *Mater. Sci. Eng. A* **559,** 147–158 (2013).

217. Darolia, R., Lahrman, D. & Field, R. The effect of iron, gallium and molybdenum on the room temperature tensile ductility of NiAl. *Scr. Metall. Mater.* **26,** 1007–1012 (1992).

218. Baker, I., Nagpal, P., Liu, F. & Munroe, P. R. The effect of grain size on the yield strength of FeAl and NiAl. *Acta Metall. Mater.* **39,** 1637–1644 (1991).

219. Geist, D., Gammer, C., Rentenberger, C. & Karnthaler, H. P. Sessile dislocations by reactions in NiAl severely deformed at room temperature. *J. Alloys Compd.* **621,** 371–377 (2015).

220. Mills, M. J. & Miracle, D. B. The structure of a〈100〉 and a〈110〉 dislocation cores in NiAl. *Acta Metall. Mater.* **41,** 85–95 (1993).

221. Schroll, R., Vitek, V. & Gumbsch, P. Core properties and motion of dislocations in NiAl. *Acta Mater.* **46,** 903–918 (1998).

222. Kim, J. T. On the slip behavior and surface film effects in B2 ordered NiAl single crystals. (University of Michigan, 1990).

223. Greer, J. R. & Nix, W. D. Size dependence of mechanical properties of gold at the sub-micron scale. *Appl. Phys. A* **80,** 1625–1629 (2005).

224. Kraft, O. & Volkert, C. A. Size effects on deformation and fatigue of thin films and small structures. in *CAMTEC* (2006).

Appendices

Appendix I: Taper angle vs. pillar diameter

This appendix includes detailed information on the taper angles exhibited by the different tested Ta, W, β-CuZn and NiAl micropillars.

Table A.1: Average taper angles of W pillars compressed at different temperatures.

Diameter (nm)	**Taper angle (°)**		
	25 °C	**200 °C**	**400 °C**
500	2.4 ± 0.1	2.4 ± 0.1	2.2 ± 0.3
1000	1.8 ± 0.1	1.7 ± 0.1	2.5 ± 0.2
2000	2.5 ± 0.1	2.6 ± 0.1	2.1 ± 0.2
3000	2.1 ± 0.1	2.2 ± 0.2	2.3 ± 0.2
4000	2.4 ± 0.1	2.2 ± 0.1	1.8 ± 0.2
5000	2.4 ± 0.2	2.3 ± 0.1	2.2 ± 0.2
Average	2.3 ± 0.1	2.2 ± 0.1	2.2 ± 0.2

Table A.2: Average taper angle of Ta pillars compressed at different temperatures.

Diameter (nm)	**Taper angle (°)**		
	25 °C	**100 °C**	**200 °C**
500	3.2 ± 0.5	3.2 ± 0.6	3.1 ± 0.4
1000	2.4 ± 0.5	2.7 ± 0.3	2.6 ± 0.4
2000	2.6 ± 0.4	2.7 ± 0.2	2.5 ± 0.3
3000	2.4 ± 0.3	2.5 ± 0.3	2.6 ± 0.3
4000	2.3 ± 0.3	2.3 ± 0.4	2.4 ± 0.4
5000	2.2 ± 0.2	2.3 ± 0.4	2.4 ± 0.3
Average	2.5 ± 0.4	2.6 ± 0.4	2.6 ± 0.3

Table A.3: Average taper angle of β-CuZn pillars with a circular cross-section.

Diameter (nm)	Taper angle (°)			
	[001]	[$\bar{1}$49]	[$\bar{1}$11]	[011]
200	5.3 ± 0.6	4.5 ± 0.3	4.9 ± 0.5	4.6 ± 0.2
500	4.9 ± 0.8	3.9 ± 0.2	2.9 ± 0.5	3.2 ± 0.3
1000	2.6 ± 0.4	2.8 ± 0.5	2.6 ± 0.3	2.5 ± 0.1
2000	2.0 ± 0.6	2.8 ± 0.3	2.4 ± 0.7	2.5 ± 0.2
3000	1.6 ± 0.2	3.1 ± 0.5	1.7 ± 0.3	2.1 ± 0.2
4000	1.6 ± 0.2	2.1 ± 0.2	1.7 ± 0.2	1.8 ± 0.1
5000	1.7 ± 0.2	1.4 ± 0.5	1.7 ± 0.1	2.1 ± 0.2
Average	2.7 ± 1.5	2.9 ± 1.0	2.5 ± 1.1	2.7 ± 0.9

Table A.4: Average taper angle of NiAl pillars with an aspect ratio of approximately 3.

Diameter (nm)	Taper angle (°)		
	[1$\bar{2}$3]	[001]	[1$\bar{2}$8]
200	5.0 ± 0.4	4.7 ± 0.3	4.1 ± 0.4
500	4.2 ± 0.4	3.5 ± 0.3	3.2 ± 0.5
1000	4.5 ± 0.4	3.7 ± 0.2	4.0 ± 0.4
2000	3.6 ± 0.4	2.6 ± 0.2	3.8 ± 0.4
3000	2.9 ± 0.5	2.7 ± 0.3	2.9 ± 0.2
4000	2.8 ± 0.3	2.5 ± 0.3	2.5 ± 0.2
5000	2.9 ± 0.3	2.9 ± 0.1	3.0 ± 0.2
Average	3.8 ± 0.9	3.2 ± 0.8	3.3 ± 0.7

Appendix II: MATLAB code – Parthasarathy's model

The following MATLAB code was implemented to calculate the yield strength as a function pillar diameter for the W and Ta micropillars in Chapter 4. The code accounts for the size dependence of the micropillars taking into account Parthasarathi's single-arm dislocation source model. It consists of a modified version of the MATLAB code first implemented by Lee *et al*. [142]. The input data changes according to the material properties and testing conditions.

```
% Parthasarathy's single arm dislocation source model
% Statistical average length of the weakest single arm dislocation
source

% Input Data - Diameter of pillars & dislocation density
Diameter_input=[.1 .2 .5 1 2 3 4 5 10]*10^-6; %unit [m]
Rho_tot=[10^10 2*10^10 5*10^10 10^11 10^12 5*10^12 10^13 1.5*10^13
2*10^13 5*10^13]; %unit [m^-2]

% Input Data - Material properties
mu=69*10^9; %Ta at room temperature - unit [Pa]
burgers=2.86*10^-10; %Ta at room temperature - unit [m]
tau_bulk=45*10^6; %Ta at room temperature - unit [Pa]
m=0.314; % schmid factor of [111]-oriented Ta, slip system {112}<111>
s=12; % num. of the most preferred slip systems (12 for BCC metals)
Beta=19.5; % slip plane orientation - unit [°]

p_output=zeros(size(Diameter_input,2),size(Rho_tot,2));
lambda_output=zeros(size(Diameter_input,2),size(Rho_tot,2));
tau_output=zeros(size(Diameter_input,2),size(Rho_tot,2));
sigma_output=zeros(size(Diameter_input,2),size(Rho_tot,2));
sigma_SI_output=zeros(size(Diameter_input,2),size(Rho_tot,2));
sigma_SD_output=zeros(size(Diameter_input,2),size(Rho_tot,2));

for z=1:size(Diameter_input,2);
    Diameter=Diameter_input(1,z);
    Height=3*Diameter;
    L_seg=Diameter/2;
    for y=1:size(Rho_tot,2);
        % Nr. of pinning points as a func. of pillar size and disl.
dens.
        Rho_mob=Rho_tot(1,y)/s;
        p=Rho_mob*pi*(Diameter/2)^2*Height/L_seg;
        p_integer=floor(p);
        if p_integer<1
            p_integer=1;
        end
        p_output(z,y)=p_integer;

        % Statistical avrg. length of the weakest arm disl. source
        b=Diameter/(2*cosd(Beta));
```

```
        funlambda=@(L)((1-((pi*((Diameter/2)-L).*(b-
L)./(pi*b*(Diameter/2)))).^(p-1)).*((pi*(((Diameter/2)-L)+(b-
L)))./(pi*b*(Diameter/2)))*p.*L;
        lambda=integral(funlambda,0,Diameter/2);
        lambda_output(z,y)=lambda;

        % Tau & sigma as a function of pillar diameter and disl.
density
        tau=tau_bulk+mu*burgers/lambda;
        sigma=tau/m;
        tau_output(z,y)=tau;
        sigma_output(z,y)=sigma;

        % Size dependent and size independent terms as a function of
disl. density
        tau_SI=tau_bulk;
        tau_SD=mu*burgers/lambda;
        sigma_SI=tau_SI/m;
        sigma_SD=tau_SD/m;
        sigma_SI_output(z,y)=sigma_SI;
        sigma_SD_output(z,y)=sigma_SD;
        tau_SI_output (z,y)=tau_SI;
        tau_SD_output (z,y)=tau_SD;
    end
end
```

Appendix III: C++ code – loading raw data analysis

An application was implemented in order to analyze the raw data extracted from the instrumented nanoindentation systems. Sneddon's corrections, load-displacement data conversion to stress-strain data as well as size effects calculations were performed using this application. It was developed in C++ programming language using the Qt platform under open-source licenses.

```
#include <QFileDialog>
#include <QFile>
#include <QMessageBox>
#include <QTextStream>
#include <QMdiSubWindow>
#include <math.h>

#include "mainwindow.h"
#include "ui_mainwindow.h"

QList<float> force,disp,popInJump;

struct structSubstrate
{
QString name;
QList<float> displacementStream;
QList<float> forceStream;
QList<float> dispCorrectStream;
QList<float> stressStream;
QList<float> strainStream;
float poisson_indenter;
float poisson_material;
float emod_indenter;
float emod_material;
float up_diameter;
float botton_diameter;
float height;
};

MainWindow::MainWindow(QWidget *parent) :
    QMainWindow(parent),
    ui(new Ui::MainWindow)
{
    ui->setupUi(this);
}

MainWindow::~MainWindow()
{
    delete ui;
}

void MainWindow::on_actionQuit_triggered()
{
    qApp->quit();
}
```

```
void MainWindow::on_single_butt_import_clicked()
{
    int count=0;

    QString fileName = QFileDialog::getOpenFileName(this, tr("Open
File"), QString(),
                tr("Text Files (*.txt);;C++ Files (*.cpp *.h)"));

    if (!fileName.isEmpty()) {
            QFile file(fileName);
            if (!file.open(QIODevice::ReadOnly)) {
                QMessageBox::critical(this, tr("Error"), tr("Could not
open file"));
                return;
            }
            QTextStream in(&file);
            force.clear();
            disp.clear();
            ui->single_textEdit_1->clear();
            ui->single_textEdit_1->append("Depth(nm)\tLoad(µN)");
            while(!in.atEnd()) {
                count=count+1;
                QString line = in.readLine();
                if(!line.isEmpty() && count>4){
                    QString sDisp = line.section('\t',0,0);
                    QString sForce = line.section('\t',1,1);
                    ui->single_textEdit_1->append(sDisp+'\t'+sForce);
                    force<<sForce.toFloat();
                    disp<<sDisp.toFloat();
                }
            }
            file.close();
    }
}

void MainWindow::on_single_butt_save_clicked()
{
    QString fileName = QFileDialog::getSaveFileName(this, tr("Save
File"), QString(),
                tr("Text Files (*.txt);;C++ Files (*.cpp *.h)"));

        if (!fileName.isEmpty()) {
            QFile file(fileName);
            if (!file.open(QIODevice::WriteOnly)) {
                // error message
            } else {
                QTextStream stream(&file);
                stream << ui->single_textEdit_1->toPlainText();
                stream.flush();
                file.close();
            }
        }
}

//\\ Sneddon's correction for pillar compression

int MainWindow::Sneddon_correction(struct structSubstrate *psubs)
{
    int end = psubs->displacementStream.size();
    float correction = 0;
    for(int i=0; i<end; i++)
    {
```

```
        correction = (psubs->displacementStream[i]) // measured
displacement
                -(((1-(psubs->poisson_indenter*psubs-
>poisson_indenter))/psubs->emod_indenter)*(psubs-
>forceStream[i]/psubs->up_diameter)) // indenter correction
                -(((1-(psubs->poisson_material*psubs-
>poisson_material))/psubs->emod_material)*(psubs-
>forceStream[i]/psubs->botton_diameter)); // substrate correction
        psubs->dispCorrectStream << correction;
    }
    return end;
}

//\\ force vs disp --> stress vs strain

int MainWindow::Stress_strain(struct structSubstrate *psubs)
{
    int end = psubs->displacementStream.size();
    for(int i=0 ;i<end; i++)
    {
        psubs->strainStream << ((psubs->dispCorrectStream[i])/(psubs-
>height));
        psubs->stressStream << ((psubs-
>forceStream[i])/(3.1416*(psubs->up_diameter*psubs->up_diameter)/4));
    }
    return end;
}

//\\ Searching file - raw data - force vs disp

void MainWindow::on_strain_butt_indent_clicked()
{
    QString fileName = QFileDialog::getOpenFileName(this, tr("Open
File"), QString(),
                tr("TXT Files (*.txt)"));
    if (!fileName.isEmpty()) {
        QFile file(fileName);
        if (!file.open(QIODevice::ReadOnly)) {
            QMessageBox::critical(this, tr("Error"), tr("Could not
open file"));
            return;
        }
    }
    ui->strain_lineEdit_1->clear();
    ui->strain_lineEdit_1->insert(fileName);
}

//\\ converting force vs disp into stress vs strain with Sneddon's
correction

void MainWindow::on_strain_butt_correct_clicked()
{
    unsigned count=0;
    structSubstrate substrate;
    structSubstrate * psubs;
    psubs = &substrate; // pointer to control the data structure

    ui->strain_textEdit_1->clear();
    psubs->forceStream.clear();
    psubs->displacementStream.clear();
    psubs->dispCorrectStream.clear();
```

```
    psubs->up_diameter = ui->strain_lineEdit_2-
>displayText().toFloat();
    psubs->botton_diameter = ui->strain_lineEdit_3-
>displayText().toFloat();
    psubs->height = ui->strain_lineEdit_8->displayText().toFloat();
    psubs->emod_indenter = ui->strain_lineEdit_4-
>displayText().toFloat();
    psubs->poisson_indenter = ui->strain_lineEdit_5-
>displayText().toFloat();
    psubs->emod_material = ui->strain_lineEdit_6-
>displayText().toFloat();
    psubs->poisson_material = ui->strain_lineEdit_7-
>displayText().toFloat();

    QString fileName = ui->strain_lineEdit_1->displayText();

    if (!fileName.isEmpty()) {
            QFile file(fileName);
            if (!file.open(QIODevice::ReadOnly)) {
                QMessageBox::critical(this, tr("Error"), tr("Could not
open file"));
                return;
            }
            QTextStream in(&file);
            while(!in.atEnd()) {
                count=count+1;
                QString line = in.readLine();
                if(!line.isEmpty() && count>9){
                    psubs->displacementStream <<
((line.section('\t',0,0).toFloat())/1000);
                    psubs->forceStream <<
line.section('\t',1,1).toFloat();
                }
            }
            file.close();
    }
    count = Sneddon_correction(psubs);
    count = Stress_strain(psubs);

    QString qount;
    ui->strain_textEdit_1->append("Top\tBotton\tHeight");
    ui->strain_textEdit_1->append(qount.number(psubs-
>up_diameter)+"\t"+qount.number(psubs-
>botton_diameter)+"\t"+qount.number(psubs->height)+"\n");
    ui->strain_textEdit_1->append("Sneddon correction performed.");
    ui->strain_textEdit_1->append("Stress-Strain calculated.");
    ui->strain_textEdit_1->append(qount.number(count)+" points
analysed.");

    // writing the diameter of each pillar at the beginning of the
file name
    QString fileNameOut = fileName.section('/',0,-2);
    fileNameOut.append("/");
    fileNameOut.append(qount.number(psubs->up_diameter*1000));
    fileNameOut.append("nm_");
    fileNameOut.append(fileName.section('/',-1,-1));
    fileNameOut.append(".csv");

    // writing output file
    if (!fileNameOut.isEmpty()) {
        QFile outfile(fileNameOut);
        if (!outfile.open(QIODevice::WriteOnly)) {
```

```
                QMessageBox::critical(this, tr("Error"), tr("Could not
write results file"));
        } else {
            QTextStream stream(&outfile);
            stream.setCodec("UTF-8");
            stream <<
"Load(uN);Disp(um);Correct_Disp(um);Strain;Strain%;Stress(MPa);File: "
<< qount.number(psubs->up_diameter*1000).toUtf8() << endl;
            for(unsigned i=1;i<count;i++)
            {stream << psubs->forceStream[i] << ";" << psubs-
>displacementStream[i] << ";" << psubs->dispCorrectStream[i] << ";" <<
psubs->strainStream[i] << ";" <<(psubs->strainStream[i])*100 << ";" <<
psubs->stressStream[i] << endl;}
            stream.flush();
        }
        outfile.close();
        ui->strain_textEdit_1->append("Output saved in:
"+fileNameOut);
    }
}

//\\ plotting strain vs size effect

void MainWindow::on_size_butt_indent_clicked()
{
    int defControl=0, points=20;
    float iniDisp = ui->shear_lineEdit_1->displayText().toFloat();
    int steps = ui->shear_lineEdit_3->displayText().toInt();
    float stepSize = ui->shear_lineEdit_4->displayText().toFloat();
    QString qount;

    QStringList indentFiles = QFileDialog::getOpenFileNames(this,
tr("Open File"), QString(),
        tr("CSV Files (*.csv)"));

    float resultsMatrix[steps+1][indentFiles.size()+3];
    for(int ite=0; ite<=steps; ite++){
        resultsMatrix[ite][0]=iniDisp+ite*stepSize;
//using the first column to storage the deformation of each raw
        for(int j=1; j<indentFiles.size()+3; j++)
resultsMatrix[ite][j]=-1.0; // inicialization to -1
    }
    ui->shear_textEdit_1->clear();

    //\\ going through all the selected files \\//
    for (int ifile = 0; ifile < indentFiles.size();
ifile++){       //every file
        QString fileName = indentFiles.at(ifile);
        QString diameter = fileName.section('/',-1,-
1).section('_',0,0).remove(-2,2); // diameter in nm units

        if (!fileName.isEmpty())
{                                   //not empty
            QFile file(fileName);
            if (!file.open(QIODevice::ReadOnly)) {
                QMessageBox::critical(this, tr("Error"), tr("Could not
open file"));
                return;
            }
            defControl=0;

            QTextStream in(&file);
//file open to read
```

```
            //\\ going through all the values in each file \\//
            while(!in.atEnd()){ //until end of file
                QString line = in.readLine();
                if(!line.isEmpty()){ //line by line
                    float fDisp = line.section(';',3,3).toFloat(); //
strain input
                    float fStrength =
line.section(';',5,5).toFloat()*1E6; // strength input in MPa
                    if(fDisp>=resultsMatrix[defControl][0] &&
defControl<steps){

if(fDisp<(resultsMatrix[defControl][0]+stepSize)){
                            resultsMatrix[defControl][ifile+1] =
fStrength;
                            if (defControl<steps)
defControl=defControl+1;
                        }else{

while(fDisp>(resultsMatrix[defControl][0]+stepSize) &&
defControl<steps){
                                ui->shear_textEdit_1-
>append(qount.number(fDisp)+">"+qount.number(resultsMatrix[defControl]
[0]+stepSize));
                                resultsMatrix[defControl][ifile+1] =
resultsMatrix[defControl-1][ifile+1];
                                defControl=defControl+1;
                            }
                            resultsMatrix[defControl][ifile+1] =
fStrength;
                            if (defControl<steps)
defControl=defControl+1;
                        }
                    }
                } //--line by line
            } //--until end of file
            resultsMatrix[steps][ifile+1]=diameter.toFloat()/1000;
            file.close();
        } //--not empty
    } //--every file

    //\\ Writing diameter-stress data - files \\//
    int posDiam=steps;
    for(int strainPos=0;strainPos<steps;strainPos++){
        QString fileName =
qount.number(resultsMatrix[strainPos][0]*100); //here just the first
strain value [0]
        fileName.append("%_strain.csv");

        QList<double> xlist;
        QList<double> ylist;
        double slope=0.0, ordenada=0.0;

        if (!fileName.isEmpty()) {
            QFile outfile(fileName);
            if (!outfile.open(QIODevice::WriteOnly)) {
                QMessageBox::critical(this, tr("Error"), tr("Could not
write results file"));
            } else {
                QTextStream stream(&outfile);
                stream.setCodec("UTF-8");
```

```
                stream <<
"Diameter;Stress;Log10_Dia;Log10_Stress;File: " << fileName.toUtf8()
<< endl;
                for(int i=1;i<indentFiles.size()+1;i++){
                    if (resultsMatrix[strainPos][i]>1){
                        xlist << log10(resultsMatrix[posDiam][i]);
                        ylist << log10(resultsMatrix[strainPos][i]);
                        stream << resultsMatrix[posDiam][i] << ";" <<
resultsMatrix[strainPos][i] << ";" << log10(resultsMatrix[posDiam][i])
<< ";" << log10(resultsMatrix[strainPos][i]) << endl;
                    }
                }

                //\\ Calling the regression function with the values
of xlist and ylist \\//
                regression1(xlist, ylist, xlist.size(), &slope,
&ordenada);
                resultsMatrix[strainPos][indentFiles.size()+1] =
slope;
                resultsMatrix[strainPos][indentFiles.size()+2] =
ordenada;
                if (xlist.size() < points){
                    ui->shear_textEdit_1-
>append(qount.number(resultsMatrix[strainPos][0]*100)+"% strain -
regression with "+ qount.number(xlist.size())+" points");
                    points--;
                }
                stream.flush();
            }
            outfile.close();
        }
    }

    //\\ Writing a file with the regression values \\//
    QString fileName = "sizeEffect_vs_strain.csv";
    if (!fileName.isEmpty()) {
        QFile outfile(fileName);
        if (!outfile.open(QIODevice::WriteOnly)) {
            QMessageBox::critical(this, tr("Error"), tr("Could not
write results file"));
        } else {
            QTextStream stream(&outfile);
            stream.setCodec("UTF-8");
            stream << "Strain;n-factor;Ordenada;File: " <<
fileName.toUtf8() << endl;
            for(int i=0;i<steps;i++){
                stream << resultsMatrix[i][0] << ";" <<
resultsMatrix[i][indentFiles.size()+1] << ";" <<
resultsMatrix[i][indentFiles.size()+2] << endl;
            }
        }
    outfile.close();
    }
    ui->shear_textEdit_1->append("...done");
}

//\\ linear regression of the points contained in xlist and ylist

void MainWindow::regression1(QList<double> xlist, QList<double> ylist,
int n, double *slope, double *ordenada)
{
    if(n>3){
        double SUMx = 0.0, SUMy= 0.0, SUMxy = 0.0, SUMxx = 0.0;
```

```
        for(int i=0;i<n;i++){
            SUMx = SUMx + xlist[i];
            SUMy = SUMy + ylist[i];
            SUMxy = SUMxy + xlist[i]*ylist[i];
            SUMxx = SUMxx + xlist[i]*xlist[i];
        }
        *slope = (n*SUMxy - SUMx*SUMy) / (n*SUMxx - SUMx*SUMx);
        *ordenada = (SUMy - *slope * SUMx) / n;
    }else{
        *slope = 0.0;
        *ordenada = 0.0;
    }
}

//\\ functions to modify in real time the stepping parameters in the
size effect tab

void MainWindow::on_shear_lineEdit_3_textChanged(const QString &arg1)
{
    ui->shear_lineEdit_4->clear();
    float ini = ui->shear_lineEdit_1->displayText().toFloat();
    float fin = ui->shear_lineEdit_2->displayText().toFloat();
    float steps = arg1.toFloat();
    QString qount;
    if (steps > 0)
        ui->shear_lineEdit_4->insert(qount.number((fin-ini)/steps));
}

void MainWindow::on_shear_lineEdit_2_textChanged(const QString &arg1)
{
    ui->shear_lineEdit_4->clear();
    float ini = ui->shear_lineEdit_1->displayText().toFloat();
    float steps = ui->shear_lineEdit_3->displayText().toFloat();
    float fin = arg1.toFloat();
    QString qount;
    if (steps > 0)
        ui->shear_lineEdit_4->insert(qount.number((fin-ini)/steps));
}

void MainWindow::on_shear_lineEdit_1_textChanged(const QString &arg1)
{
    ui->shear_lineEdit_4->clear();
    float fin = ui->shear_lineEdit_2->displayText().toFloat();
    float steps = ui->shear_lineEdit_3->displayText().toFloat();
    float ini = arg1.toFloat();
    QString qount;
    if (steps > 0)
        ui->shear_lineEdit_4->insert(qount.number((fin-ini)/steps));
}
```